creative commons
COMMONS DEED

저작자표시-비영리-변경금지 2.0 대한민국

이용자는 아래의 조건을 따르는 경우에 한하여 자유롭게

- 이 저작물을 복제, 배포, 전송, 전시, 공연 및 방송할 수 있습니다.

다음과 같은 조건을 따라야 합니다:

저작자표시. 귀하는 원저작자를 표시하여야 합니다.

비영리. 귀하는 이 저작물을 영리 목적으로 이용할 수 없습니다.

변경금지. 귀하는 이 저작물을 개작, 변형 또는 가공할 수 없습니다.

- 귀하는, 이 저작물의 재이용이나 배포의 경우, 이 저작물에 적용된 이용허락조건을 명확하게 나타내어야 합니다.
- 저작권자로부터 별도의 허가를 받으면 이러한 조건들은 적용되지 않습니다.

저작권법에 따른 이용자의 권리는 위의 내용에 의하여 영향을 받지 않습니다.

이것은 이용허락규약(Legal Code)을 이해하기 쉽게 요약한 것입니다.

Disclaimer

dCollection

공학박사학위논문

Friction Stir Welding Analysis by Using CFD Heat-Flow Analysis and Inherent Strain Method

CFD 열-유동 해석 및 고유변형도법을 이용한 마찰교반용접 해석에 관한 연구

2014년 8월

서울대학교 대학원

조선해양공학과

강 성 욱

Friction Stir Welding Analysis by Using CFD Heat-Flow Analysis and Inherent Strain Method

CFD 열-유동 해석 및 고유변형도법을 이용한 마찰교반용접 해석에 관한 연구

지도 교수 장범선

이 논문을 공학박사학위논문으로 제출함.

2014년 8월

서울대학교 대학원

조선해양공학과

강 성 욱

강성욱의 박사학위논문을 인준함.

2014년 7월

위 원 장 _____ (印)

부위원장 _____ (印)

위 원 _____ (印)

위 원 _____ (印)

위 원 _____ (印)

Abstract

Friction Stir Welding Analysis by Using CFD Heat-Flow Analysis and Inherent Strain Method

Kang, Sung Wook

Dept. of Naval Architecture and Ocean Engineering

The Graduate School

Seoul National University

Friction stir welding (FSW) is a new technology which makes it possible to join two materials such as aluminum alloy, magnesium alloy and dissimilar materials at a solid state. Nowadays, FSW is mainly used for vehicles like vessel, aircraft, railcar and automobile. In this study, a three dimensional numerical model is constructed for the heat transfer analysis of the FSW using a commercial computational fluid dynamics (CFD) software Fluent and finite element analysis software ANSYS multi physics. The heat transfer analysis result is used to calculate welding deformation and residual stress. Before the simulation, several simplifying assumptions are made to the model. Three different heat transfer analysis were carried out and compared with each other. Especially, a rotation affected zone concept is imposed for CFD analysis. The rotation affected

zone is a constant volume. In this volume, flow is rotated the same as the tool rotation speed and so plastic dissipation occurs. The CFD analysis is good to gain better understanding of the flow pattern regarding the vicinity of the tool. Also, the result of the asymmetric temperature distribution is remarkable as compared with other analysis. Also, the asymmetric feature of FSW are considered using a coupled CFD-FEM simulation. Heat transfer analysis was carried out by using CFD commercial program Fluent and the results were used finite element structural analysis by using ANSYS multi physics. The calculated residual stresses were compared with an experimental value by using X-ray diffraction method. Finally, inherent strain method was developed considering external constraint and features of FSW. At this time, external constraint was defined as reaction force and it was predicted using neural networks. This method result of the residual stress was verified by comparing the thermal elasto-plastic analysis, and experimental result.

Keywords : Friction stir welding, Heat transfer analysis, Elasto-plastic analysis, Computational fluid dynamics, Finite element method, Residual stress, Inherent strain method, External constraint, Neural networks
Student Number : 2007-20659

LIST OF CONTENTS

1. Introduction..... 1

1.1. Overview and principle of friction stir welding..... 1

1.2. Current status of friction stir welding for research development..... 4

1.3. Current status of friction stir welding for technology development..... 5

1.4. Current status of the main patent and prospect of future of friction stir welding. 10

1.5. Objective of this research..... 12

2. Heat transfer analysis of friction stir welding.... 14

2.1. CASE I: Representation of heat flux as formula..... 24

2.2. CASE II: Contact with work piece and rotational-tool-based method..... 30

2.3. CASE III: Computational fluid dynamics-based method..... 40

3. Heat transfer analysis results of three different methods..... 56

3.1. Heat transfer analysis results of CASE I.. 56

3.2. Heat transfer analysis results of CASE II 58

3.3. Heat transfer analysis results of CASE III..... 62
3.4. Summary of three different heat transfer analysis methods..... 68
4. Experiments of friction stir welding..... 70
5. Comparison with experimental and simulation temperature results..... 81
5.1. Welding dimension and parameters for heat transfer analysis..... 81
5.2. Heat transfer analysis results and discussions..... 82
5.3. Summary of heat transfer analysis..... 100
6. Comparison with experimental and simulation residual stress results..... 102
6.1. Welding dimension and parameters for residual stress analysis..... 108
6.2. Temperature data of CFD analysis mapping to the FE model..... 109
6.3. Structural analysis model and results..... 118
6.4. Residual stress analysis results and discussions..... 121
6.5. Summary of residual stress analysis..... 134
7. Welding analysis based on equivalent strain method to cover external constraint during friction stir welding..... 136

7.1. Definition of inherent strain..... 138
7.2. Inherent strain method to consider friction stir welding features..... 139
7.3. Predict a reaction force during cooling stage using neural networks..... 157
7.4. Inherent strain chart..... 180
7.5. Comparison of residual stress using experimental data, thermal elasto−plastic analysis, and inherent strain method using neural networks..... 183
8. Conclusion..... 194
REFERENCES..... 196

LIST OF TABLES

Table 1. The applications of FSW..... 9

Table 2. Comparison of three methods..... 20

Table 3. Experimental welding conditions of Ref. #1 [25]..... 21

Table 4. Experimental welding conditions of Ref. #2 [26]..... 21

Table 5. Experimental welding conditions of Ref. #3 [27]..... 22

Table 6. Chemical composition of AA6061-T6... 23

Table 7. The experimental measuring locations. (The x, y, and z coordinates are shown in Fig. 2)..... 23

Table 8. Welding efficiency and friction coefficient values from parametric study..... 29

Table 9. Boundary conditions..... 46

Table 10. Cell zone conditions..... 46

Table 11. The range of design variables (a, b) for parametric study..... 50

Table 12. Material constant and other values for AA6061-T6 [37]..... 53

Table 13. The work piece and tool dimensions for the experiments..... 72

Table 14. The welding parameters of the experiments..... 72
Table 15. The experimental measuring locations. (The x, y, and z coordinates are shown in Fig. 2)..... 80
Table 16. Heat transfer analysis model for comparison..... 81
Table 17. Summary of residual stress magnitude and other information [43]..... 103
Table 18. Residual stress analysis model for comparison..... 109
Table 19. Welding conditions for parametric study..... 127
Table 20. Summary of the parametric study results..... 133
Table 21. Welding condition and parameter for reaction force data base..... 143
Table 22. Maximum residual stress location in AS and the temperature of it location in Fig. 78..... 149
Table 23. Maximum residual stress location in different conditions..... 151
Table 24. Comparison of thermal elasto-plastic analysis and neural networks results for reaction force during cooling stage.. 175

Table 25. Weight and bias matrix for reaction force..... 178
Table 26. Minimum and maximum values of input data for 61 data base using thermal elasto-plastic analysis results..... 179
Table 27. Maximum residual stress in y-direction..... 185
Table 28. General case for verification of neural networks..... 188
Table 29. Input data using heat-flow analysis, and output data by using neural networks..... 189
Table 30. Maximum residual stress in y-direction..... 192

LIST OF FIGURES

Fig. 1.	The actual FSW process.....	2
Fig. 2.	Schematic view of FSW process.....	3
Fig. 3.	Overview of FSW process.....	4
Fig. 4.	Fillet welding free modularized tanker....	7
Fig. 5.	Temperature-dependent material properties.....	18
Fig. 6.	Friction heat between work piece and tool.....	25
Fig. 7.	(a) Finite element modeling for CASE I; (b) Heat input to nodes of FE model.....	27
Fig. 8.	Calculation flow chart of CASE I.....	28
Fig. 9.	Temperature-dependent material properties.....	31
Fig. 10.	Calculation flow chart of CASE II.....	34
Fig. 11.	Assumed coefficient of temperature-dependent friction for CASE II.....	36
Fig. 12.	Finite element modeling for CASE II.....	37
Fig. 13.	Velocity of tool.....	38
Fig. 14.	Velocity of work piece.....	38
Fig. 15.	Thermal contact conductance (a) between work pieces and (b) between work piece and tool shoulder.....	39

Fig. 16. Two different methods for rotating tool (a) Model I: Contact surface; (b) Model II: Rotation region..... 43
Fig. 17. Description of heat flow analysis model.. 45
Fig. 18. The cross sectional macrostructure..... 47
Fig. 19. Design variables for modeling of RAZ..... 49
Fig. 20. Calculation flow chart..... 55
Fig. 21. Transient heat transfer analysis results of Ref. #1..... 56
Fig. 22. Temperature history of parametric study results for CASE I and Ref. #1..... 57
Fig. 23. Temperature distribution of parametric study results for CASE I and Ref. #1..... 57
Fig. 24. Temperature history of parametric study results for CASE I and Ref. #2..... 58
Fig. 25. Transient heat transfer analysis results of Ref. #1..... 59
Fig. 26. Temperature history of parametric study results for CASE II and Ref. #1.... 59
Fig. 27. Temperature distribution of parametric study results for CASE II and Ref. #1.... 60
Fig. 28. Temperature history of parametric study results for CASE II and Ref. #2.... 60
Fig. 29. Frictional heat of Ref. #1..... 61
Fig. 30. Plastic deformation heat of Ref. #1..... 62

Fig. 31. Temperature distribution of parametric study results for CASE II and Ref. #1.... 64
Fig. 32. Temperature distribution of parametric study results for CASE II and Ref. #3.... 65
Fig. 33. Streamline with strain rate of Ref. #1.... 66
Fig. 34. Streamline with velocity of Ref. #1..... 67
Fig. 35. Streamline with temperature of Ref. #1.. 68
Fig. 36. The FSW experiment equipment..... 71
Fig. 37. The configuration of butt FSW experiment..... 73
Fig. 38. The configuration of three different T-joint FSW experiments..... 74
Fig. 39. Installation of thermocouple..... 75
Fig. 40. The entire FSW experimental process.... 76
Fig. 41. Special jig for T-joint FSW (a) A schematic diagram; and (b) Real jig..... 77
Fig. 42. The failed experiments..... 78
Fig. 43. Butt FS welded work piece..... 78
Fig. 44. T-joint FS welded work piece..... 79
Fig. 45. Tool for FSW experiments..... 79
Fig. 46. CFD simulation results of Exp. #1 (a) The temperature distribution; (b) The streamline with the temperature..... 83
Fig. 47. Temperature distribution of parametric study results of Exp. #1..... 85

Fig. 48. Temperature distribution of parametric study results of Exp. #2..... 86
Fig. 49. Model I and most well matching Model II cases with Exp. #1 and Exp. #2..... 87
Fig. 50. The main effect plot for temperature with variable 'a' 89
Fig. 51. The main effect plot for temperature with variable 'b' 89
Fig. 52. Polishing process..... 91
Fig. 53. Hot mounting specimen..... 92
Fig. 54. Etching process (a) Specimen in the etching solution; (b) Finish the etching process..... 93
Fig. 55. Olympus JP/BX51M electron microscope 94
Fig. 56. The cross sectional macrostructure of Exp. #1..... 94
Fig. 57. The cross sectional macrostructure of Exp. #2..... 95
Fig. 58. The cross sectional macrostructure of Exp. #7 (a) T butt joint; (b) T lap joint I; (c) T lap joint II..... 96
Fig. 59. Marked the weld nugget, TMAZ, HAZ, and base metal of Exp. #1..... 96
Fig. 60. Marked the weld nugget, TMAZ, HAZ, and base metal of Exp. #2..... 97

Fig. 61. The cross sectional velocity distribution of Exp. #1..... 98
Fig. 62. The cross sectional temperature distribution of Exp. #1..... 100
Fig. 63. The XRD equipment for measuring residual stress..... 108
Fig. 64. Temperature distribution of experimental and simulation results of Exp. #3 – 7..... 110
Fig. 65. Heat flow model using the Fluent (Left), and elasto-plastic model using the ANSYS Multi physics (Right)..... 111
Fig. 66. Temperature distribution of Exp. #5 and simulation results..... 113
Fig. 67. Temperature history of Exp. #5 and simulation results in AS (Top) and RS (Bottom)..... 114
Fig. 68. Temperature distribution at the first heat transfer analysis step..... 115
Fig. 69. Temperature distribution of the total region and the region without tool volume (E.T., Empty Tool)..... 116
Fig. 70. Temperature history of the total region and the region without tool volume, in AS (Top) and RS (Bottom)..... 117

Fig. 71. Calculation flow chart..... 119
Fig. 72. Temperature dependent material properties for elasto−plastic analysis..... 120
Fig. 73. Residual stresses results of experiment and simulation for Exp. #3 – 7..... 123
Fig. 74. The residual stress distribution, compared to knowing the effect of the rotation speed..... 125
Fig. 75. The residual stress distribution, compared to knowing the effect of the welding speed..... 126
Fig. 76. 3D temperature distribution at the middle stage of the welding..... 129
Fig. 77. 3D longitudinal residual stress distribution after the cooling..... 130
Fig. 78. The longitudinal residual stress distribution at 'Line AA' 131
Fig. 79. Summary of the parametric study results with variable welding speed (top) and rotation speed (bottom)..... 133
Fig. 80. Calculation flow chart of inherent strain method to cover external constraint during FSW..... 137
Fig. 81. Total strain is divided 4 strains..... 138

Fig. 82. Sectional temperature distribution of FSW..... 140
Fig. 83. Inherent strain model considered external constraint during FSW..... 141
Fig. 84. Distance from the weld centerline to external constraint..... 142
Fig. 85. Reaction force of three different cases... 145
Fig. 86. Effect of reaction force during heating and cooling for residual stress distribution..... 146
Fig. 87. Definition of TG in the conventional fusion welding analysis model [55]..... 147
Fig. 88. Definition of TG in the FSW analysis model..... 148
Fig. 89. Temperature gradient of x-direction (TGx)..... 152
Fig. 90. Location of inherent strain input and weighting of center value..... 153
Fig. 91. Temperature distribution of FSW..... 154
Fig. 92. Interpolated inherent strain values and input location..... 155
Fig. 93. Maximum tensile residual stress in y-direction using three different methods... 156
Fig. 94. Residual stress distribution in y-direction of No. 1..... 157

Fig. 95. Inherent strain according to (a) maximum temperature, (b) temperature gradient in x-direction, and (c) reaction force..... 159
Fig. 96. Conceptual diagram of a neural network. 162
Fig. 97. Supervised training in neural network..... 164
Fig. 98. Relationship between reaction force and welding parameters..... 167
Fig. 99. The factors affecting the reaction force 168
Fig. 100. Temperature distribution of No 1 case: (a) Consider the maximum temperature, (b) Do not consider the maximum temperature..... 169
Fig. 101. Temperature distribution of No 1 case (a) As it is, (b) Taking the value of the natural logarithm..... 169
Fig. 102. Approximated temperature distribution by a logarithmic function..... 170
Fig. 103. Approximated temperature distribution by a 2nd-order polynomial function..... 170
Fig. 104. Approximated temperature distribution by a 3rd-order polynomial function..... 171
Fig. 105. Approximated temperature distribution by a 4th-order polynomial function..... 171

Fig. 106. The structure of the neural networks for predict a reaction force during cooling stage..... 173
Fig. 107. Input and target data base for make a neural networks function..... 174
Fig. 108. Verificatioin of neural networks..... 174
Fig. 109. Interactive process for training neural networks..... 177
Fig. 110. Structure of neural networks..... 178
Fig. 111. Inherent strain charts..... 182
Fig. 112. Residual stress distribution in y-direction..... 185
Fig. 113. Comparison of thermal elasto-plastic analysis with inherent strain method using neural networks for residual stress distribution in y-direction..... 192

NOMENCLATURE

A : Material constant (s^{-1})

b : Acceleration of body force (N)

C_p : Specific heat (J/Kg)

D_p : Diameter of pin (m)

D_s : Diameter of shoulder (m)

D_{raz} : Rotation-affected cell zone diameter (m)

D/Dt : Material time derivative

F_f : Friction force (N)

F_N : Downward force (N)

H_p : Height of pin (m)

h : Convective heat transfer coefficient (W/ m^2°C)

h_c : Thermal contact conductance coefficient (W/m^2°C)

k : Thermal conductivity (W/m°C)

L : Length of work piece

n : Material constant

P : Normal pressure (Pa)

Q : Activation energy (J/mol)

Q_f : Frictional heat (W)

Q_p : Plastic deformation heat (W)

Q_t : Total heat (W)

Q_1 : Heat generated between top surface of work piece and bottom surface of tool shoulder (W)

Q_2 : Heat generated between tool−pin lateral side and side surface of work piece (W)

Q_3 : Heat generated between tool−pin bottom and work piece (W)

$\dot{Q}$: Heat generation rate due to plastic deformation (W)

R : Gas constant (J/mol°C)

R_p : Radius of pin (m)

R_s : Radius of shoulder (m)

S : Deviatoric stress (Pa)

T : Temperature (°C)

TB : Surrounding temperature (°C)

t : Thickness of work piece

u, v, w : x, y, and z directions

v : Velocity of material flow (m/s)

v_f : Slip velocity (m/s)

W : Width of work piece

W_p : Plastic work

Z : Zener−Holloman parameter (s^{-1})

α : Material constant (MPa^{-1}), Thermal expansion coefficient (1/°C)

γ : Conversion factor

ε_e : Elastic strain

ε_p : Plastic strain

ε_{pt} : Phase transformation strain

ε_{th} : Thermal strain

$\dot{\varepsilon}$: Strain rate (s^{-1})

$\dot{\bar{\varepsilon}}$: Effective strain rate (s^{-1})

η : Welding efficiency

η_f : Fraction of frictional energy

η_p : Fraction of plastic work

μ : Friction coefficient, Viscosity

ρ : Density (Kg/m^3)

σ : Cauchy stress (Pa)

$\bar{\sigma}$: Flow stress (Pa)

τ : Shear stress (Pa)

ω : Rotation speed of tool (rad/s = $2\Pi/60*RPM$)

1. Introduction

1.1. Overview and principle of friction stir welding

FSW was invented at The Welding Institute UK in December 1991 [1, 2]. With its relatively high efficiency and savings in cost and time, it is both remarkably popular in the relevant industries and good for the environment. Recently, FSW has been applied to various structures due to the following many advantages:

- ✓ solid-state welding; therefore, welding deformation is small;
- ✓ uses light alloys such as aluminum, magnesium, and titanium;
- ✓ excellent mechanical strength;
- ✓ weld defects are fewer than in fusion welding;
- ✓ eco-friendly, given the lack of harmful gas emission;
- ✓ welding process is not dependent on worker skill; thus standardization and automation are possible;
- ✓ economical, given that no post-welding process or welding consumables are necessary;

- ✓ can join dissimilar alloys and different sheet thicknesses.

According to the principle of FSW, a pin on the tip of the rotating tool is probed into the joint part of the work piece, which is referred to as a stirring or mixing process, and then the work pieces are almost melted and joined. The rotating tool generates frictional heat by rotating at a constant speed while applying a constant downward force to the work piece. FSW is accomplished by the heat generated in the stirring process. There are two heat sources: the friction between the tool shoulder and the work piece, and the plastic deformation of the solid-state material in the vicinity of the rotating pin. Fig. 1 provides the actual FSW process.

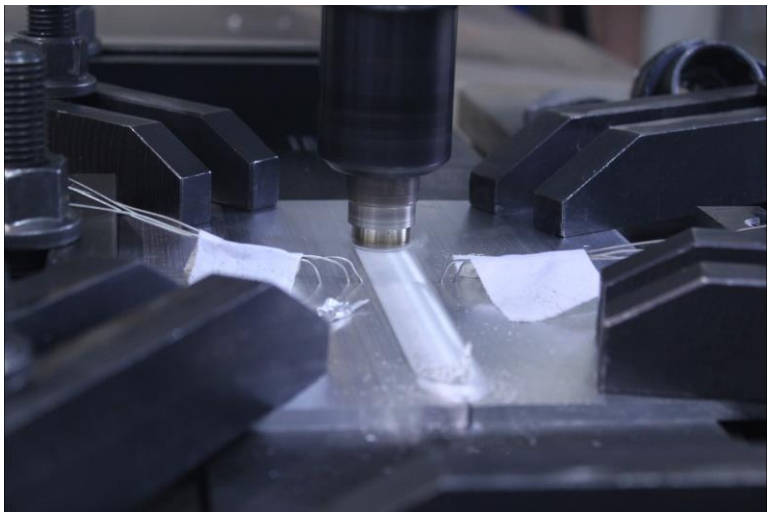

Fig. 1 The actual FSW process.

Advancing side (AS) is the same as the travel (welding) direction and the surface motion due to spinning, whereas retreating side (RS) is opposes the travel direction and surface motion. Fig. 2 provides a schematic view of the FSW process.

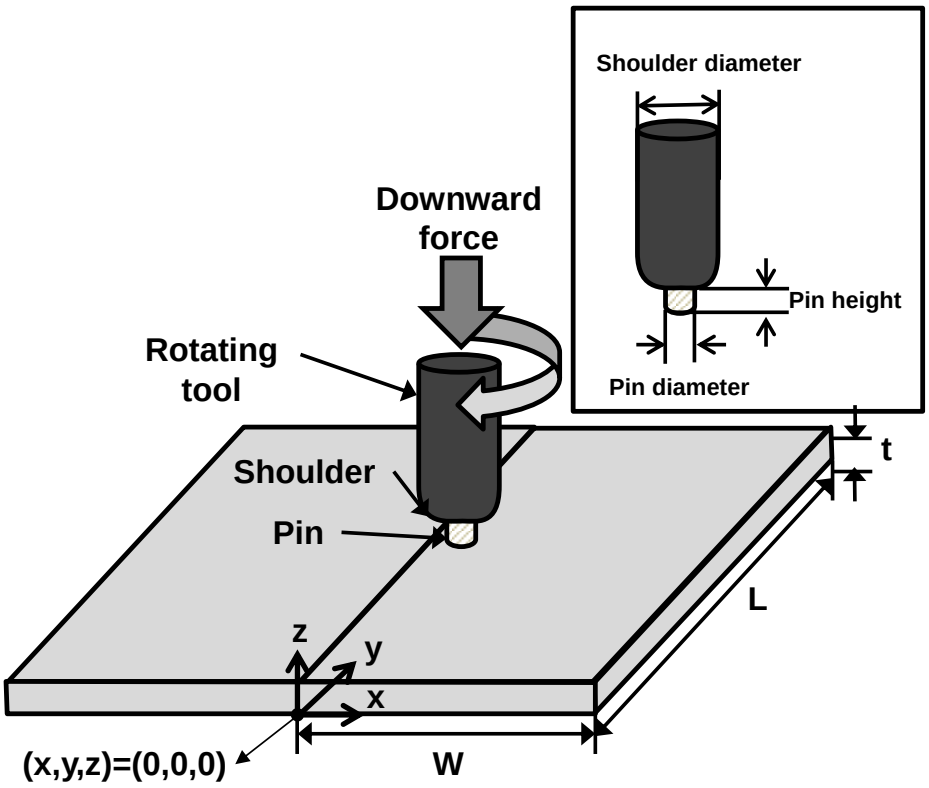

Fig. 2 Schematic view of FSW process.

FSW is performed in four steps welded as shown in Fig. 3. In step 1, the tool is inserted into the base material. In step 2, the tool is rotated at a predetermined position, thereby increasing the temperature. In step 3, the tool is moving along the weld line, and bond the base materials. In step 4, after the welding is completed, the tool comes out from the base material.

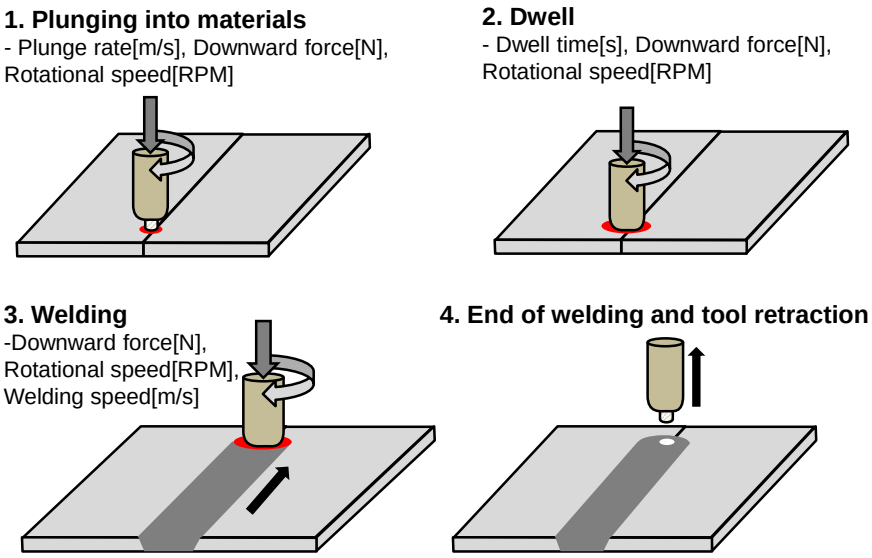

Fig. 3 Overview of FSW process.

1.2. Current status of friction stir welding for research development

The current status of FSW research development in domestic is as follows. FSW equipment is installed in Busan University, and Chosun University. Thus, a number of researches are underway here mainly

Research for analyzing the mechanism of joint fracture by observing the mechanical properties and structure of the joint based on the friction stir welding process variables were carried out, and optimum welding parameters were deducted in Busan University. In addition, they are expressed as follows

about the cause of the failure of aluminum during welding. When the softening of the material in the stirring section is not sufficiently occur, the plastic flow is unlikely to occur. This is a reason of the failure. Therefore, it has been reported appropriate temperature is necessary for weldability of FSW [3, 4].

In Chosun University, hybrid FSW and dissimilar FSW researches were carried out mainly. For FSW, which was used to a non-ferrous metal such as aluminum. Magnesium, copper alloy having a low melting point, magnesium, and copper. In order to apply for dissimilar FSW with titanium and steel which have a high melting point, the laser welding or TIG welding was used with FSW. Furthermore, the evaluation of mechanical properties was performed in accordance rotation speed of the tool, welding speed through tensile, hardness test, and microstructure observation of the joint [5-7].

1.3. Current status of friction stir welding for technology development

FSW has been developed The Welding Institute in England (TWI) in 1991. Since then, demand increase of the FSW at home and abroad has been increased and researches has been actively processed. FSW technique has been used not only means of transport vessel, automotive, aerospace, and railway

vehicle, also electronic products such as LCD back plate.

In shipbuilding industry, first aluminum living quarter with use of FS welded panels supplied to Norsk Hydro's installation OsebergSør at marine aluminum in 1998. Nowadays, FS welded aluminum products were used in ship large components, deck, floor, and heliport. In addition, the U.S. military has applied the FSW technology to high-speed boat deck. Recently, through the project of the country, DONGYANG GANGCHUL and Samsung Heavy Industries conducted a reaserch about the possibility of FSW on LNG carriers through "LNG Carriers Using Aluminum Structures" in June 2010 to May 2013. The demand for LNG increases sharply worldwide, ultra LNG carriers is preferred to reduce transportation costs. Thus, the use of possible non-ferrous metals has been studied actively to secure the cryogenic properties of levels equal or greater iron material, and these materials are lightweight. Especially aluminum has the characteristic that elongation and strength at low temperature is increased, so it is actively used for parts that require properties as cryogenic encapsulated. Fillet welding free modularized tanker production is object in this project. The concept of fillet welding free modularized tanker is schematized in Fig. 4.

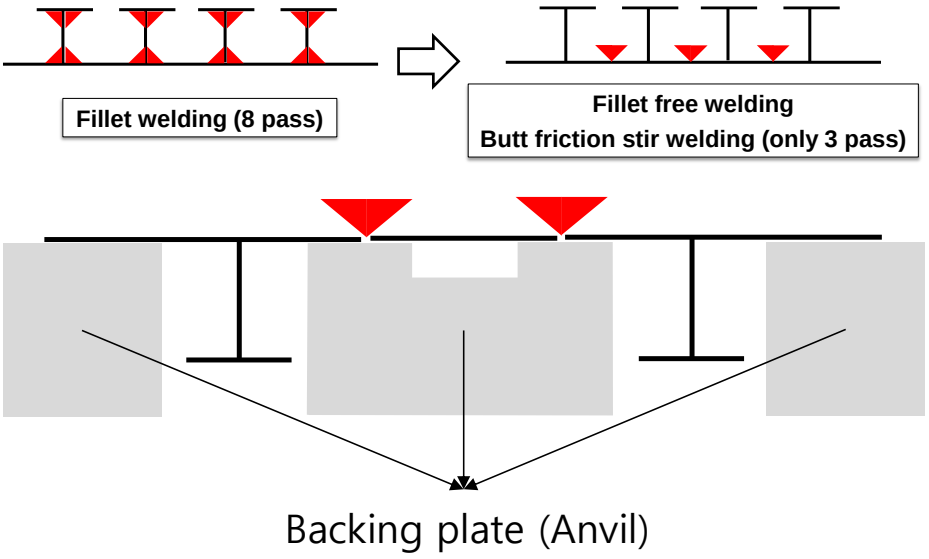

Fig. 4. Fillet welding free modularized tanker.

Thus, studies of the aluminum material in the field of marine and shipbuilding will be actively processed. It will be associated with this, interest in the aluminum welding is increased, and interest in FSW is concentrated.

In Kawasaki Heavy Industries of Japan, to produce a high-speed car ferry and high speed passenger vessel by applying the FSW technology. In the automotive field, which was used for bonding of aluminum and steel from the automobile companies Mazda Corporation of Japan. Friction stir spot welding (FSSW) is applied to the bonnet of the car, and develop mass production technology for the first time in Honda's. Furthermore, by using the FSSW technique is applied the inner panel of the door of the car, and the interior panel of the hood and panels within the roof of the car, the studies to be applied to other automotive parts are underway. In aerospace industry,

FSW is utilized in the fabrication of many fuel tanks in rocket technology and it is used to replace a rivet in aircraft. By adopting the FSW technique and structure surface portion of the aircraft, Eclipse Aviation of the United States has led to major changes in the production of aircraft. Military transport ship (C-17) tanks and Delta rocket of Boeing is utilizing the FSW in the fabrication of the internal structure. In the field of railway vehicles, Hitachi Japan has produced the A-train using the FSW. Korea Railroad Research Institute has ongoing research on many of the FSW technology. Besides, it is used for cutting tools such as a drills, taps, end mills, drill bit and for electronic components such as motor shaft, electrical terminals, high pressure hose, the piping rathet wrench. Also, it is used in office automation parts and construction machinery such as copy roller, track roller, track roller bush, and hydraulic cylinder piston rod. In addition, panel of 5 mm thickness of iMAC U.S. Apple's, FSW technology is used, finally it is used universally across all industry sectors. These are summarized in Table 1.

Table 1. The applications of FSW.

Sector	Applications
Aerospace	Structural components
	Commercial airframes
Rolling stock	Freight cars, Coaches
Marine	Boat hulls
	Propellers
Consumer durables	Refrigerators and freezers
	Air conditioners
Construction	Cladding, Roofing
	Window and door frames
	Fencing
Electrical	Busbars
	Transformers and generators
Industrial	Heat exchangers
	Hydraulic systems
Machinery and equipment	Irrigation piping
Automobiles	Inner and outer body panels
	General structural components
	Bumper components
	Seats, Load floors, Wheels
	Suspension parts, Drive shaft
	Drive shaft yokes
	Engine accessory brackets and mounts
	Sub-frames and engine cradles
	Miscellaneous
	Radiator, heater and evaporator fins
	Condenser tubes
	Condenser and radiator fins

In BBC Research (2010) 'Welding Equipment And Supplies: According to The Global Market' in 2009-2014, the world market for the welding process, which is expected to growth of 5% a year, and FSW is expected to grow to 3.6% annually followed arc welding. In addition, to overcome the technical limitations of the future, with the step-by-step progress of the process and equipment, applications will expand. It is expected that the development of equipment and FSW process technology of high melting point metal material such as high-strength steel, high heat-resisting alloy, and titanium alloy are activated in particular. As a result, it is expected that the world market size of FSW is much larger.

1.4. Current status of the main patent and prospect of future of friction stir welding

FSW is the new solid state bonding technology developed in the TWI, and has been patented in 1991. FSW research mainly active in Japan, the United States and Europe, it is also gradually expanding in Korea. Shape of the weld joint and the tool had a major focus in recently patents. In particular, T-joint FSW technology has not been studied much. Most of FSW research has limited to butt weld. Therefore, it is worth about studying the shape of the T-joint FSW.

Study of the FSW recent can be divided into four major.

- ✓ Characterization of the weld zone both at microscopic and macroscopic levels.
- ✓ Effect of variation of different FSW parameters on the mechanical and metallurgical properties of the welds.
- ✓ Effect of post welding treatments such as shot peening and laser peening on the mechanical and metallurgical properties of the welds.
- ✓ Corrosion susceptibility of the different zones in the weld region.

In future, study to the FSW of dissimilar materials effective would be done more. A number of studies will be carried out on the development of tools and processes. For it to be fixed so as not to move the base material of the FSW is a very important technological development of the fixing device therefor will also be actively studied in the future. Furthermore, the development of the auxiliary device such as load control tool pressing the base material to the FSW process at the time, and temperature sensor to maintain the proper temperature during FSW must also be performed. Lastly, research on FSW process variable necessary.

In developed countries of FSW for this purpose, it is

actively engaged in the material flow analysis, the development of equipment for the practical application of the technology, and the material and shape of the tool. For the shape tool design and optimization of FSW conditions, the aluminum is assumed to be incompressible non-Newtonian fluid and studies on material traveling along the periphery of the tool during rotation using computational fluid dynamics (CFD). For this reason, a new experimental technique, theoretical, and computational analysis model has been developed.

1.5. Objective of this research

In conventional welding, the number of welding parameters are not many. In the case of FSW, the tool is the important key of weldability. Thus, the shape and dimension of tool is significant, and the rotation speed of the tool is the same. In the previous literature, the maximum temperature is maintain about 80 – 90% of the melting temperature of the material for a great weldability. When a certain work piece is given, the worker decide the tool and welding parameters. However, it is not easy to decide the tool geometry and welding parameters using experiment all the time. Therefore, FSW heat transfer analysis method is needed for predict the weldability effectively.

In the case of FSW, the maximum temperature is 80 – 90% of the melting point of the materials. Thus, the residual

stresses are smaller than for other fusion welding, and have mostly not been considered before. However, sometimes FSW residual stresses are measured at about 70% or above. This residual stress significantly affects fatigue behavior and lifetime. Therefore, the residual stress distributions in various welding conditions and shapes of FSW are studied. In this study, thermal elasto-plastic analysis is carried out and verified with experimental residual stress distribution. However, this method has a long computational time. For example, structural analysis time took 8 hours in the thermal elasto-plastic analysis, but inherent strain method took only 10 minutes. Thus, inherent strain method for FSW is developed. Using inherent strain method, it is possible that structural analysis of a large and complex structure.

In this study, we developed reliable heat transfer analysis method using CFD heat-flow analysis, and structural method using inherent strain.

2. Heat transfer analysis of friction stir welding

Heat transfer analysis of FSW has been intensively researched over the last ten years. This work can be classified according to assumptions with respect to the complicated mechanism between the tool and the work piece. Heat is generated both from plastic deformation of the work piece and from friction between the work piece and the tool surface during FSW. For simulation convenience, heat transfer analysis methods can be simply classified into three categories: full sliding, full sticking, and partial sliding/sticking conditions.

Full sliding simulation is based on the assumption that heat is generated only by friction. The heat flux is calculated as a function of the downward force and the friction coefficient. The value thus obtained is applied to the tool contact area. Chao et al. [8] presented a three-dimensional heat source model of the parent metal based on the premise that a constant heat flux occurs from the tool shoulder, which model is adjusted by comparison with the measured temperature distribution. Gould et al. [9] applied the Rosenthal method to the analytical heat transfer model. Models consider friction heat only at the shoulder and use the finite difference method for the numerical solution of the heat equation. Colegrove et al. [10] proposed an

improved analysis method for estimation of heat-generation distributions from a threaded tool pin. Their results indicated that the pin heat contribution could be as high as 20% of the total heat generated. Frigaard et al. [11], ignoring the heat input due to the pin, suggested a constant heat flux under the shoulder. Khandkar et al. [12] modeled the heat transfer of a welding model of lap joint FSW. The frictional heat was generated at the interface of the tool shoulder and work piece; the heat generated by plastic deformation of the weld metal in the vicinity of the pin, meanwhile, was assumed to be a fraction of the frictional heating caused by the shoulder. Song et al. [13] presented a more precise three-dimensional heat transfer model of the tool and work piece based on short-term temperature simulation by finite element methods (FEM) and modeling the heat input from the thread helix angle pin as a moving heat source.

The second heat transfer analysis category is full sticking simulation. Here, the solidus part of the work piece is modeled as a fluid, adopting the full sticking condition at the interface between the tool and the material. This assumes that heat is induced only from plastic dissipation, not from friction. The heat flux is calculated according to the simulation-derived strain rate and viscosity of the solidus zone. Bendzsak et al. [14] and Smith et al. [15] modeled heat transfer by the finite difference method, assuming the FSW-welded parent metal to be a non-

Newtonian fluid material. Their model consists of a rotating region, a tool region, and a stationary region. Ulysse [16] employed a three-dimensional visco-plastic model to calculate, as products of the effective stress and effective strain rate, temperature distributions relative to tool speed. Aljoaba et al. [17] utilized STAR CCM+ in case studies of heat transfer analysis. Also, some case studies for different welding speeds and rotational speeds have been carried out for temperature, strain rate, flow stress and material velocity. Kim et al. [18] performed a heat transfer analysis using Fluent (a commercial computational fluid dynamics software). Temperature-dependent-material properties were considered by a user-defined function, and the different effects of the tilted tool, both with and without modeling of a backing plate, were investigated.

The third heat transfer analysis category is simulation partial sliding/sticking condition, in which the sliding and sticking conditions constitute a mixed state. Reynolds et al. [19] conducted inverse modeling of heat generation that entailed calculation of the friction and deformation conditions based on the measured welding torque and power. Schmidt et al. [20] established an analytical model for FSW-induced heat generation based on different assumptions of the contact condition between the rotating tool surface and the work piece, albeit with the contact-state rate defined. Recently, the arbitrary Lagrangian Eulerian (ALE) simulation was used for

friction stir spot welding (FSSW) considering tool pin modeling [21]. Fourment et al. [22] performed a heat transfer analysis using FORGE3 FE software. They compared the temperature distribution result with both a threaded tool pin and an unthreaded tool pin. This method uses software to calculate heat from the frictional and plastic dissipation. Users only input the welding parameters and conditions. However, this method cannot simulate transient analysis of the traveling process in FSW, since the work piece meshes get broken by the tool elements.

The present heat transfer analysis considers only convection at the work piece and at the tool; radiation is not considered. The convective heat boundary condition is represented as

$$\nabla T = \frac{h}{k}(T - T_B) \tag{1}$$

where h is the convective heat transfer coefficient, k is the thermal conductivity, T is the temperature, and T_B is the surrounding temperature.

The top and side surfaces of the work piece are in contact with ambient air; the convective heat transfer coefficient is 30 W/m^2°C. The bottom surface of the work piece is supported by a backing plate. The convective heat transfer coefficient is

determined by the downward force of the tool and the thermal material properties of the backing plate. In the present analysis, the convection coefficient of the bottom surface, 200 W/m^2°C, is used [23, 24]. To calculate the temperature field, material nonlinear analysis is performed considering temperature-dependent material properties such as density, specific heat, and thermal conductivity. These material properties are plotted in Fig. 5 [8].

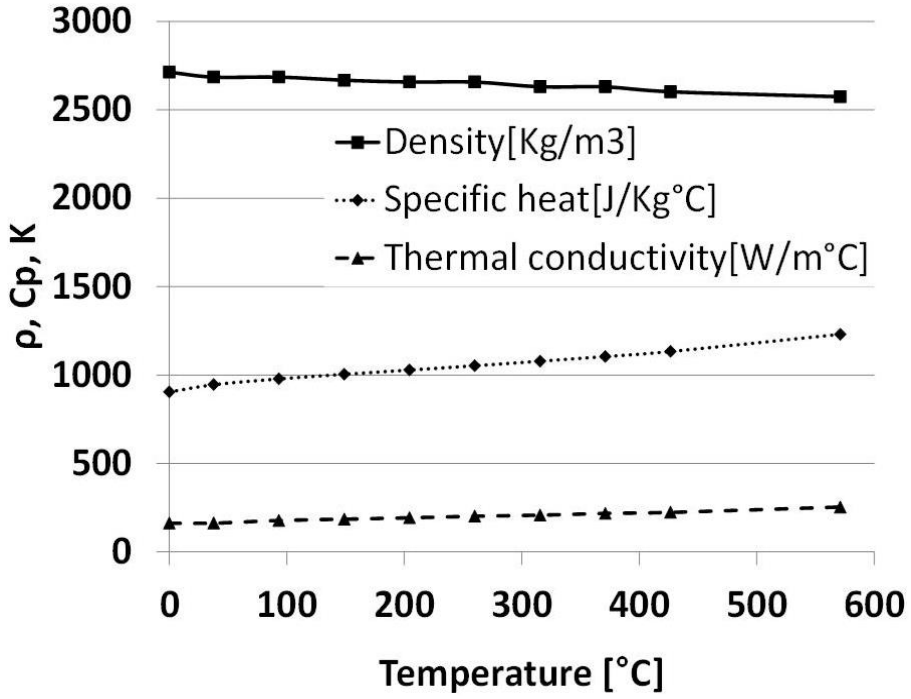

Fig. 5 Temperature-dependent material properties.

As mentioned above, the FSW process entails three different heat transfer analyses. These methods are CASE I, CASE II, and CASE III. CASE I and CASE II are implicit FEMs for transient heat transfer analysis. CASE I applies an

equivalent friction-inducing heat source in the FE work piece model; CASE II the heat source FE model consists of the work piece and the tool shoulder. Frictional heat between the work piece and the tool shoulder is calculated under the contact condition. The heat induced by plastic deformation energy is calculated in the vicinity of the tool shoulder. CASE III employs CFD for heat transfer analysis under the steady state. The CFD model consists of the work piece and the entire tool. The heat induced by plastic deformation is calculated as a function of the strain rate and viscosity. CASE I, CASE II and CASE III are compared in Table 2.

Table 2. Comparison of three methods.

	CASE I	CASE II	CASE III
Contact condition	Full sliding	Partially sliding and partially sticking	Full sticking
Heat source	Friction (Equivalent heat source formula)	Friction and plastic deformation (Contact condition)	Plastic deformation (function of viscosity and strain rate)
Modeling	Work piece only	Work piece and only tool shoulder	Work piece and entire tool
Simulation stages	Traveling (welding)	Plunge Dwell Traveling (welding)	Traveling (welding)
Temperature result	Symmetry	Indistinct asymmetry	Clear asymmetry
Analysis program	ANSYS multi physics (FEM)		Fluent (CFD)
Analysis type	Transient		Steady state
Compared experiment model	Temperature distribution and history (Exp. #1) Temperature history (Exp. #2)		Temperature distribution (Exp. #1 and Exp. #3)
Unspecified variables	Welding efficiency Friction coefficient	Temperature-dependent friction coefficient	Size of rotating region

Before FSW experiment, three FSW experimental temperature data were referred based respectively on three previous studies [25 – 27]. The plate size, tool size, and welding parameters of the experiments are listed in Tables 3 – 5.

Table 3. Experimental welding conditions of Ref. #1 [25].

Plate Size			Tool Size		
W (mm)	L (mm)	t (mm)	Shoulder diameter (mm)	Pin diameter (mm)	Pin height (mm)
50	240	6	24	6	< 6
Welding parameters					
Tool tilt (°)		Rotation speed (RPM)	Welding Speed (mm/min)		Downward Force (N)
0		500	140		19000

Table 4. Experimental welding conditions of Ref. #2 [26].

Plate Size			Tool Size		
W (mm)	L (mm)	t (mm)	Shoulder diameter (mm)	Pin diameter (mm)	Pin height (mm)
101.6	254	12.7	50	12	12
Welding parameters					
Tool tilt (°)		Rotation speed (RPM)	Welding Speed (mm/min)		Downward Force (N)
0		637	95.4		25000

Table 5. Experimental welding conditions of Ref. #3 [27].

Plate Size			Tool Size		
W (mm)	L (mm)	t (mm)	Shoulder diameter (mm)	Pin diameter (mm)	Pin height (mm)
70	100	12	32	10	9
Welding parameters					
Tool tilt (°)		Rotation speed (RPM)	Welding Speed (mm/min)		Plunge Depth (mm)
0		600	50		0.12

These three experimental models are defined herein as Ref. #1, Ref. #2, and Ref. #3. Aluminum alloy 6061-T6 (AA6061-T6), the chemical composition of which is summarized in Table 6, was used in each experiment.

Table 6. Chemical composition of AA6061−T6.

Component	Percentage (%)
Aluminum, Al	Remainder
Chromium, Cr	0.04-0.35
Copper, Cu	0.15-0.40
Iron, Fe	Max 0.7
Magnesium, Mg	0.8-1.2
Silicon, Si	Max 0.4-0.8
Zinc, Zn	Max 0.25

The experimental temperatures were measured by thermocouple. The obtained temperature data were used to verify the validity of the proposed methods. The temperature history was measured at a point during the welding process, and the temperature distribution was measured at several points perpendicular to the welding line when the tool was at the weld centerline. The experimental measuring locations are listed in Table 7.

Table 7. The experimental measuring locations. (The x, y, and z coordinates are shown in Fig. 2).

	Temperature history (x mm, y mm, z mm)	Temperature distribution (x1 ~ x2 mm, y mm, z mm)
Ref. #1 [25]	(10, 120, 4.4)	(10 ~ 30, 120, 4.4)
Ref. #2 [26]	(12, 120.7, 10.7)	−
Ref. #3 [27]	−	(−40 ~ 40, 50, 9)

2.1. CASE I: Representation of heat flux as formula

In CASE I, the tool is assumed to fully slide on the work piece, and heat is generated due to only the friction between the work piece and the tool. The work piece is assumed to be a rigid body, and the heat energy conversion from the plastic deformation is neglected. Thus, the heat source model can be represented simply as the function of the downward force, friction coefficient, and rotation speed.

Heat is generated on three contact areas (A_1, A_2, and A_3), as shown in Fig. 6. First, heat (Q_1) is generated by the friction between the surface of the work piece and the bottom surface of the tool shoulder. This, greater than 90% of the total friction heat, is the main heat source in FSW. Second, heat (Q_2) is generated by the friction between the work piece and the tool pin's lateral side. Third, heat (Q_3) is generated by friction between the work piece and the bottom surface of the tool pin.

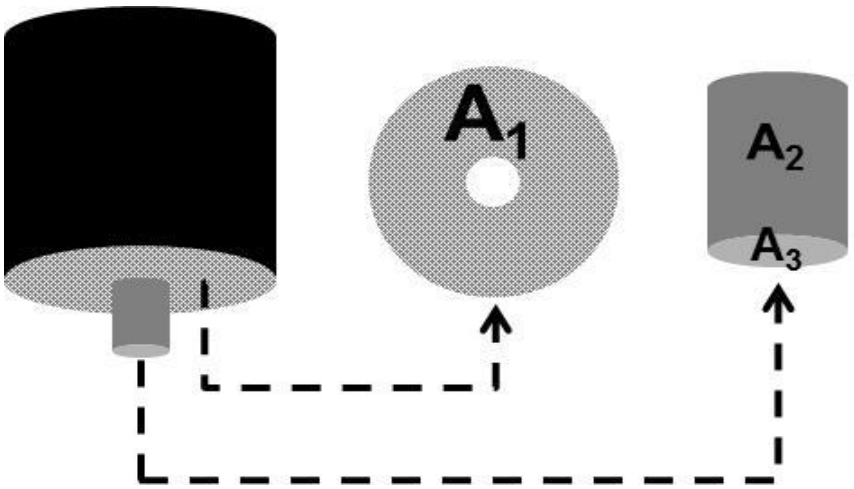

Fig. 6. Friction heat between work piece and tool.

The first heat source, based on FE analysis, was suggested by Chao et al. in 1998 [8]. They posited a heat flux distribution on the shoulder as a formulation of a radial heat flux intensity distribution. Colegrove et al. [10] and Reynolds et al. [19] considered the friction heat from both the shoulder and the pin contact. For simplified calculation, the analytical heat source model makes three assumptions:

· the downward force between the work piece and the tool is uniform;

· the bottom of the shoulder is flat;

· the shape of the pin cylindrical.

In this study, in order to obtain an accurate analytical result, Reynolds et al. [19]'s friction heat formula is used:

$$Q_t = Q_1 + Q_2 + Q_3$$
$$= \eta \cdot \left[\frac{2\pi\omega}{3} \tau \left(R_S^3 - R_P^3 \right) + \frac{2\pi\omega}{3} \tau R_P^3 + 2\pi\omega R_P^2 H_P \right] \quad (2)$$

where η is the welding efficiency, ω is the rotation speed, τ is the shear stress, R_s is the radius of the shoulder, R_p is the radius of the pin, and H_p is the height of the pin. Under the full sliding condition, the shear stress on the surface of the work piece is expressed as

$$\tau = \mu P = \frac{\mu F_N}{\pi R_S^2} \quad (3)$$

where μ is the friction coefficient, P is the normal pressure, and F_N is the downward force.

The FE model consists of only one work piece. The number of elements is 46,080, and fine mesh is adopted in the vicinity of the welding center line as in Fig. 7 (a). The calculated heat is directly inputted to the nodes of the FE model and uniformly distributed, as shown in Fig. 7 (b).

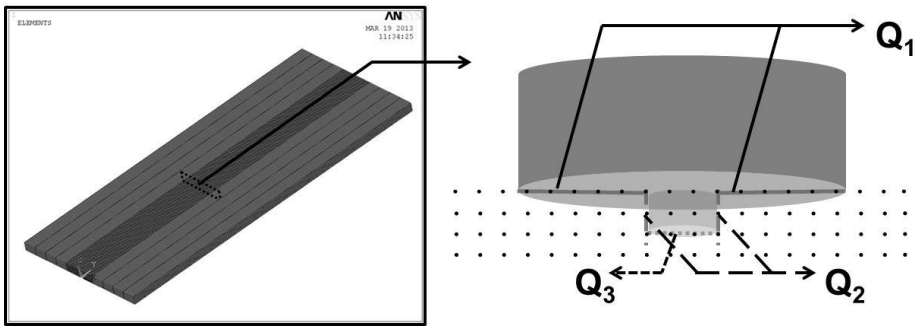

Fig. 7. (a) Finite element modeling for CASE I; (b) Heat input to nodes of FE model.

The temperature distribution in accordance with the time history, which is the heat transfer analysis result, can be utilized for the purposes of a structural analysis. The heat transfer and structural analyses are not carried out simultaneously; that is, the results of the heat transfer analysis influence the structural analysis, and the structural analysis results have no impact on the heat transfer analysis. This approach is known as semi-coupled thermal-stress analysis. The calculation flow chart is as shown in Fig. 8. As indicated, structural analysis is not carried out in CASE I.

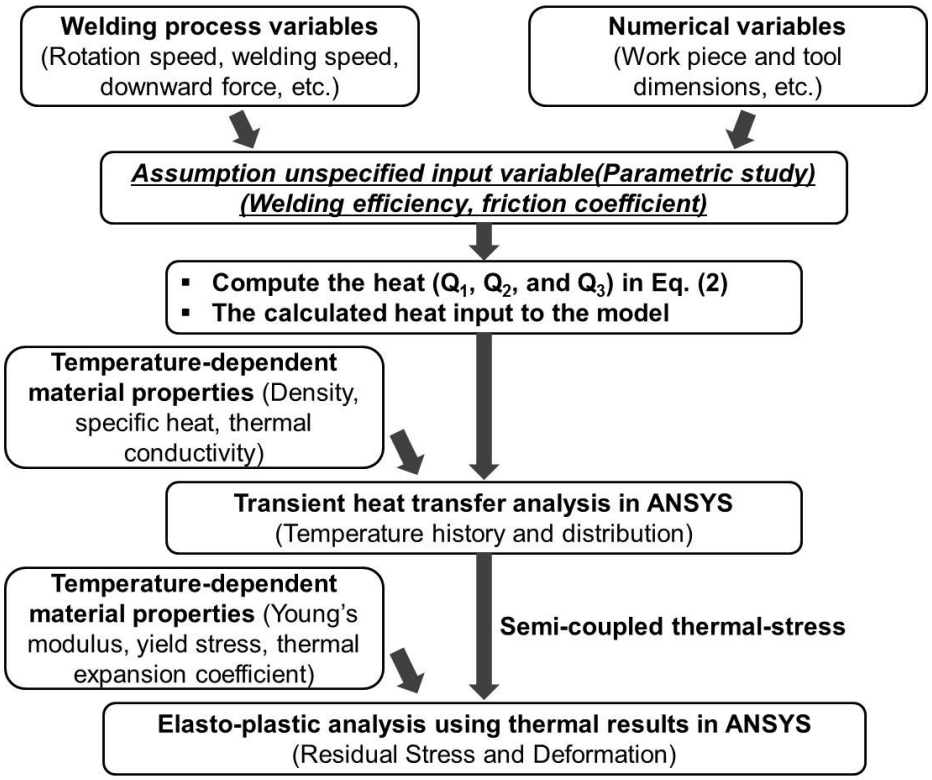

Fig. 8. Calculation flow chart of CASE I.

To calculate the heat (Q) in Eq. (2), the welding efficiency and the friction coefficient are required. The other values are listed in Tables 3 – 5.

For welding efficiency, 0.69 (from Goo et al. [28]) and 0.88 (from Schmidt et al. [29]) are used.

The coefficients of static and sliding friction are 0.61 and 0.47, respectively, for the friction between the aluminum and steel [30]. Generally, the friction coefficient is dependent on temperature, velocity, and pressure on the contact surface. Thus, the friction coefficient used in FSW must be lower than the coefficient of sliding friction value. The friction coefficient

values of Song et al. [26] and Xu et al. [31] are 0.4 and 0.3 for AA6061-T6, respectively. Song et al. [32] used 0.5 at 300K, which value linearly decreases to 0.3 at the melting point. Chen et al. [25] also used a constant friction coefficient, though they did not report the value.

Many different friction coefficients have been used, and different welding efficiencies reported, in the above-noted literature. Therefore, it is worth determining how sensitive the resultant temperature distribution is to those factors and what values yield results that are close to the measured distribution. The friction coefficient and welding efficiency values obtained in FSW parametric study are provided in Table 8.

Table 8. Welding efficiency and friction coefficient values from parametric study.

Variable	Values	Number of cases
Welding efficiency (η)	0.6, 0.7, 0.8, 0.9	24
Friction coefficient (μ)	0.25, 0.3, 0.35, 0.4, 0.45, 0.5	

2.2. CASE II: Contact with work piece and rotational-tool-based method

From the physical point of view, the FSW process is a fully-coupled thermal-stress problem. First, coupling occurs when deformations end up making a change in the associated heat transfer analysis. Such a change can bring out large deformation or change of the contact condition. Second, coupling generates heat due to plastic deformation.

CASE I is a sequential method. First of all, heat transfer analysis is carried out for the total time step, after which, according to that result, structural analysis is performed. In CASE I, only the material nonlinearity is considered in the heat transfer analysis, and only an equivalent heat source is used. Thus, the simulation differs from the actual FSW process. For realistic FSW simulation, CASE II is proposed. CASE II is a thermal-stress analysis that is carried out simultaneously. Frictional heat arises between the top surface of the work piece and the tool shoulder, and plastic deformation heat is induced in the vicinity of the tool. These heats are influential to the temperature change. The temperature history influences the stresses and strains through the coefficient of thermal expansion. Also, because the work piece geometry is changed at each time step, geometric non-linearity is considered; and since the material behavior is dependent on the current

deformation state and the deformation history, material nonlinearity is considered as well. The temperature-dependent yield stress, Young's modulus and coefficient of thermal expansion are applied to the structural analysis as shown in Fig. 9 [8].

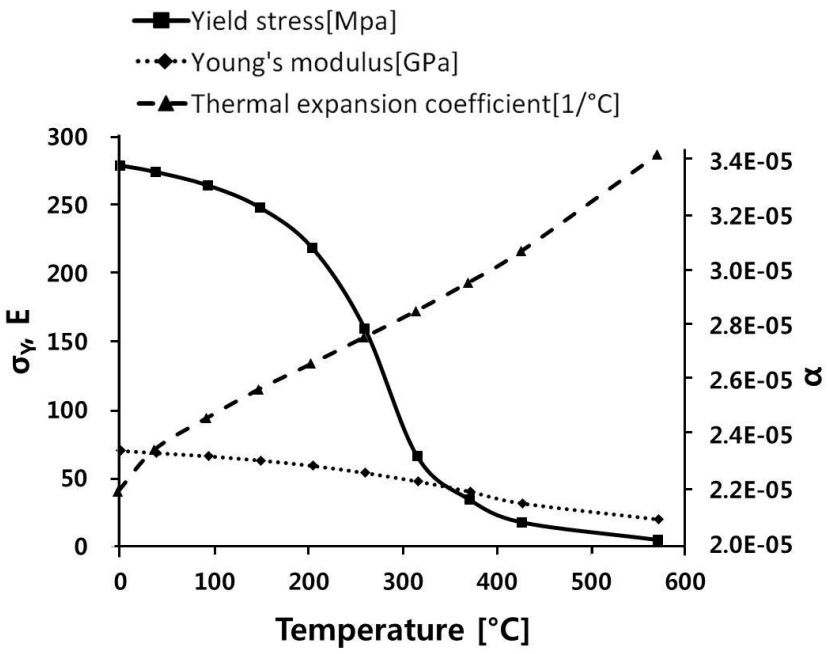

Fig. 9. Temperature-dependent material properties.

Deformation influences heat transfer as the tool moves along the weld center line. At each time step, the contact area is changed. This has an impact on the nonlinearity of the displacement boundary condition. Additionally, in the contact area, the thermal load is changed by the temperature-dependent friction coefficient and slip velocity. This means that force boundary condition non-linearity must also be considered.

Temperature influences stresses via the temperature-dependent material properties. Thus, the heat transfer analysis and structural analysis results have a mutual influence. As reflects the feasibility of the nonlinearity analysis of the contact boundary condition, the FE model consists of the work piece and the tool shoulder.

At the first time step of the initial temperature, the material properties are chosen. At the next step, the results of the first step are applied, and the material properties are estimated on the basis of the updated temperature field. The calculated heats, as calculated from the results for the previous time step, are assumed to remain constant and even. The temperature and displacement solutions are calculated by Newton-Raphson iterations. The calculation flow chart is as shown in Fig. 10. As noted above, CASE II analysis considers four nonlinear behaviors; thus, the analysis time is much longer than in CASE I. Nevertheless, CASE II has many advantages. No additional assumption or tuning process for the heat source model are necessary. Also, CASE II simulation can be applied to a real experimental process. Simulation of the plunge, dwell, and traveling stages, moreover, is possible, whereas CASE I and CASE III can simulate only the traveling stage.

For simplicity of calculation, the CASE II analytical model makes four assumptions:

· the work piece and the tool experience frictional sliding contact described by Coulomb's friction law;

· the friction coefficient is a function of the surface temperature;

· all of the dissipated energy induced by friction is converted to heat, as is 95% of the heat applied to the work piece;

· 95% of the plastic deformation energy is converted to heat [33].

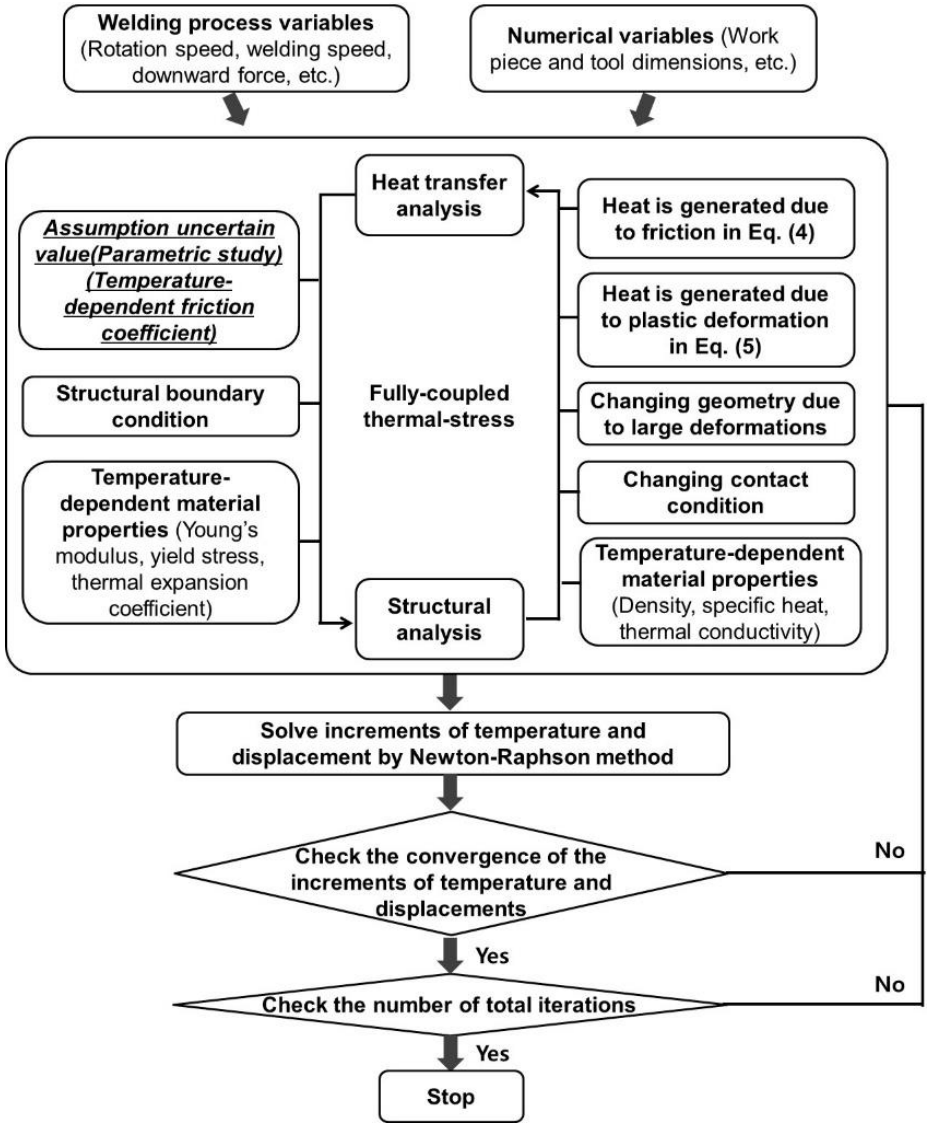

Fig. 10. Calculation flow chart of CASE II.

Frictional heat is expressed as

$$Q_f = \eta_f F_f v_f = \eta_f \mu F_N v_f \tag{4}$$

where Q_f is the frictional heat, η_f is the fraction of the

frictional energy (=0.95), F_f is the friction force, v_f is the slip velocity at the contact surface, μ is the temperature-dependent friction coefficient, and F_N is the downward force.

The heat induced by plastic deformation energy is expressed as

$$Q_p = \eta_p W_p = \eta_p \sigma \varepsilon \tag{5}$$

where Q_p is the plastic deformation heat, η_p is the fraction of plastic work (=0.95), W_p is the plastic work, σ is the stress, and ε_p is the plastic strain.

For accurate temperature distribution and history calculation, temperature-dependent friction coefficients are assumed for parametric study. This assumption is based on two facts regarding the friction coefficient: first, between the aluminum and the steel under the sliding contact condition, the friction coefficient is 0.47; second, at the melting point, the friction coefficient is almost zero. Thus, the coefficient of temperature-dependent friction is assumed as the exponential function

$$\mu = f(T) = 0.4832 e^{-aT} \tag{6}$$

where a is the variable. The coefficient of temperature-dependent friction values assumed for CASE II are plotted in

Fig. 11.

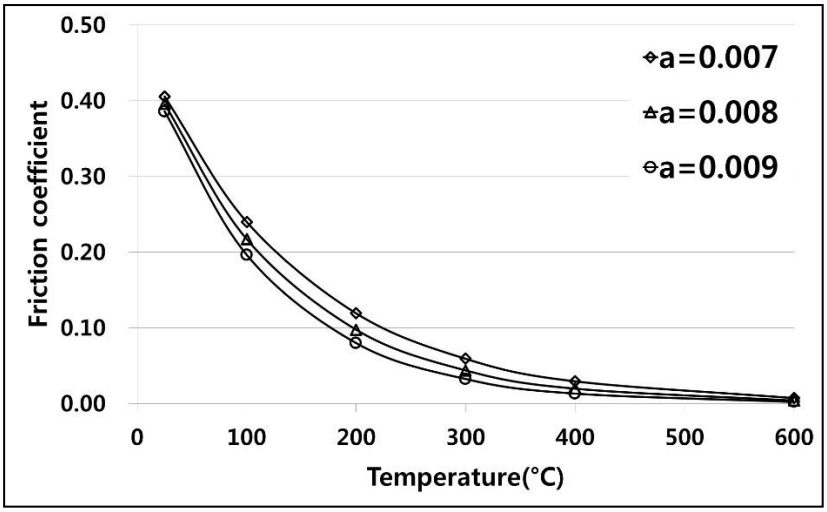

Fig. 11. Assumed coefficient of temperature-dependent friction for CASE II.

The FE model is composed of the half-and-half work piece and tool shoulder as shown in Fig. 12. The number of elements is 1,404. Although the pin is not modeled here, the main heat source is between the work piece and the shoulder, and the work piece meshes are not broken by the tool pin elements. The rotating tool moves the surface of the work piece.

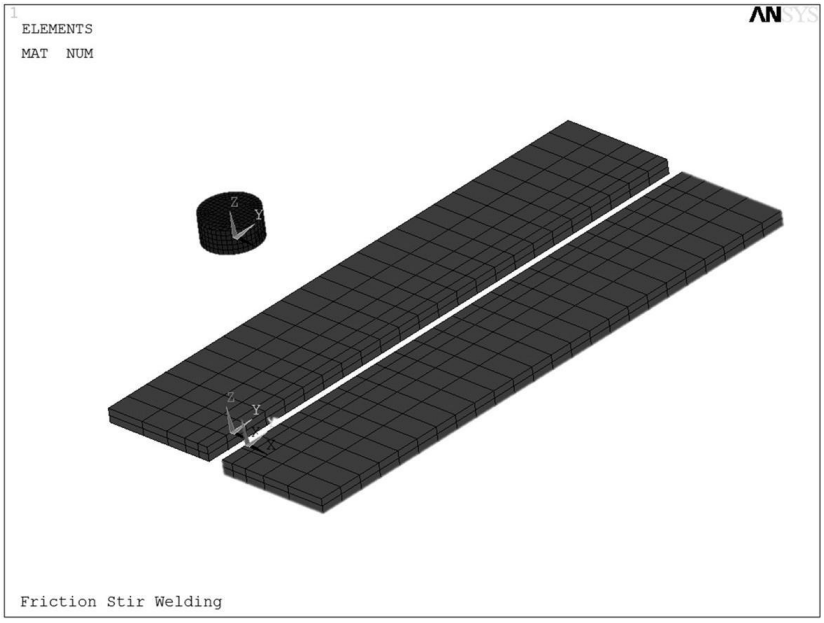

Fig. 12. Finite element modeling for CASE II.

The linear velocity of the tool is linearly proportional to the distance from the center of the tool. In Ref. #1, the rotation speed is 500 rpm and the tool radius is 12 mm. The linear velocity at the far circumference of the tool is about 0.63 m/sec. The velocity of the work piece is influenced by the velocity of the tool. The velocities of the tool and work piece are shown in Fig. 13 and Fig. 14, respectively.

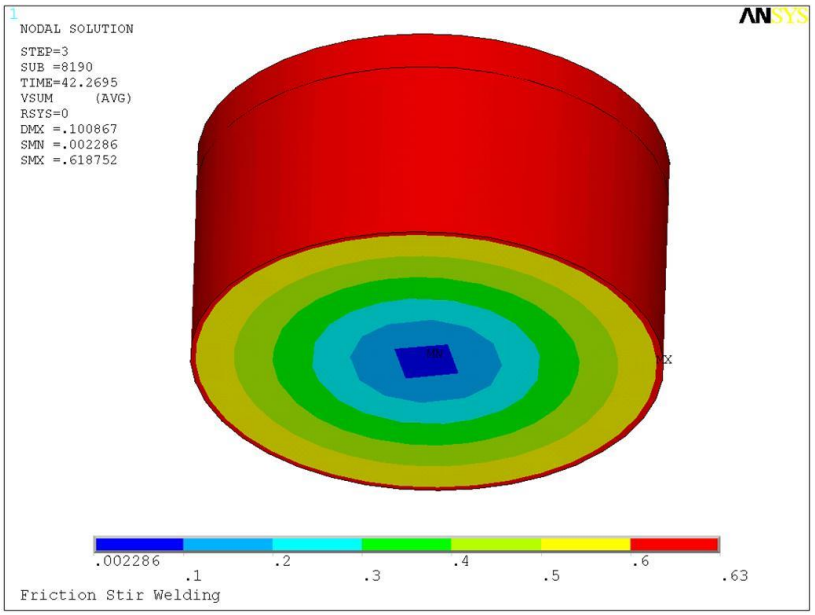

Fig. 13. Velocity of tool.

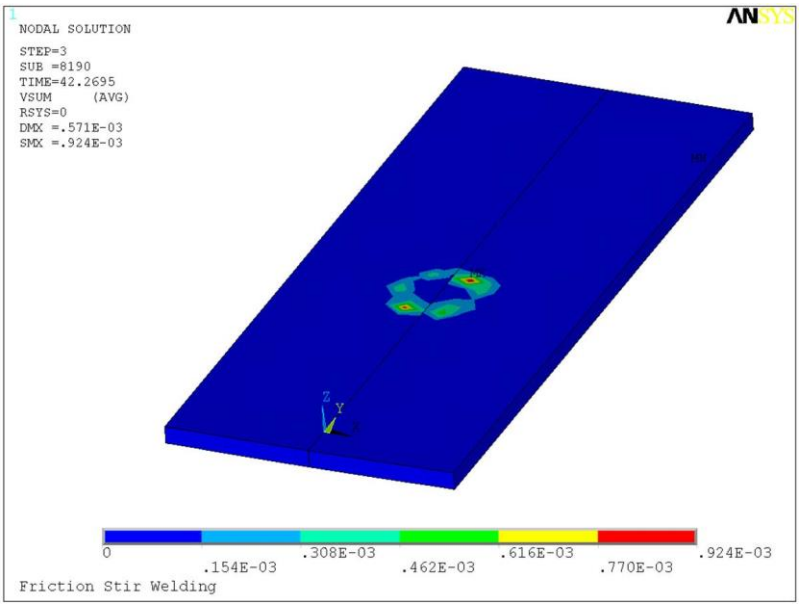

Fig. 14. Velocity of work piece.

Two other conditions also are considered. First, the structural boundary conditions: in order to simulate the backing plate at the bottom of the work piece, all of the bottom nodes of

the work piece are constrained in the thickness direction; also, the work piece is clamped on both sides, and the nodes along the long edges to a range of 10 mm are constrained in all degrees of freedom. The second condition considered is thermal contact conductance between the side surfaces of the work piece and between the work piece and the tool shoulder as shown in Fig. 15. Thermal contact conductance is the heat conduction between the solid contacted bodies. The thermal contact conductance coefficient (hc), accordingly, describes the thermal conductivity between two contacted bodies [34].

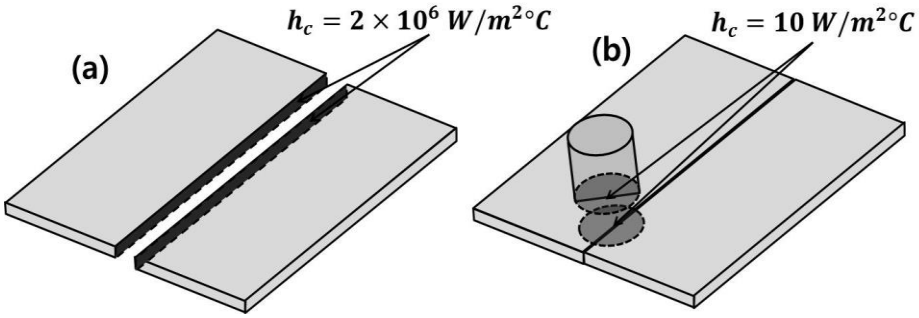

Fig. 15. Thermal contact conductance (a) between work pieces and (b) between work piece and tool shoulder.

The condition of the contact surface of the work piece is changed under high temperature. At the initial time step, the contact surfaces are separated; however, the temperature increase leads to merging of nodes, which is also referred to as bonding. In this study, 400°C is considered to be the bonding temperature, which is also approximately 70% of the AA6061-T6 melting temperature. This condition influences the fully-

coupled thermal–stress analysis.

Finally, a parametric study is implemented by Eq. (6) for 3 cases of a: 0.007, 0.008, and 0.009 in Eq. (6).

2.3. CASE III: Computational fluid dynamics–based method

In CASE III the numerical method of CFD is used to solve the fluid–particle flow assuming continuity. The FEM is one where equivalent heat sources are calculated by function of rotation speed, welding speed, the friction coefficient, the downward force, and welding efficiency. The calculated heat flux is the heat source of the FE model. However, the analysis of using the FEM does not reflect the intrinsic character of FSW. It is just a simplified method. On the other hand, the analysis of using CFD can reflect the intrinsic character through several assumptions. During the FSW process, the work piece becomes a solidus state at the vicinity of the tool. The CFD analysis can predict particle behavior and asymmetric temperature distribution can be simulated. To analyzed FSW using CFD, the heat source model can be divided into two. However, in the previous research, the description of the heat source model is insufficient. T. Long and D. G. Kim et al. [35, 18] rotated the contact surface between

the tool and the work piece as a moving wall boundary condition. Moreover, the contact surface is assumed as a no-slip condition and considered plastic deformation induced heat. P. A. Colegrove and Shercliff [36] divided six regions in the FSW model. A solid aluminum, tool, and backing plate for the solid region and a fluid aluminum, stationary mesh region, and rotating mesh region for the fluid region where the rotating mesh region rotates. However, there is no detailed information about the rotating mesh region. The one thing that can be conjectured in his paper is that the shape of the rotation mesh region is a circular cone. Also, isothermal and non-isothermal heat sources are considered. In the case of isothermal and non-isothermal, the heat sources used were at 800K and plastic dissipation, respectively. G. J. Bendzsak et al. [14] divided the CFD model into a tool, stationary and rotating region, and rotated the rotating region along the direction of the tool. The rotation region shape is assumed to be in a circular cylinder and the diameter of the circular cylinder is the same as the tool diameter. And the part of the tool pin is subtracted by the circular cylinder. The heat source is only considered a plastic dissipation. S. Z. Aljoaba et al. [17] composed a heat model with a solid body tool and a liquid aluminum sheet. The contact surface between the tool and the sheet is rotated and the heat source is calculated as friction heat.

A calculated heat source is input on the contact surface. R. Nandan et al. [37] input a heat source at the contact surface between the tool and the work piece, but any explanation about the rotating tool did not exist. P. Ulysse and D. H. Santiagoa et al. [16, 38] assumed that 90% of plastic dissipation is a heat source of FSW, but no information of a rotation tool was given. S. W. Kang and Jang [39] rotated the cylindrical region with the exception of the tool area. Heat generation is calculated as the product of the effective stress and effective strain rate. Also, the effective stress is assumed as a temperature dependent yield stress. As noted above, for most of the paper on FSW simulation using CFD, a description of the heat source model is insufficient. In this study, the CFD finite volume method (FVM) with the Eulerian description approach is adopted. The full sticking condition at the contact surface between the tool and the work piece is assumed for the FSW heat transfer analysis. Due to the condition, heat is generated by only the plastic deformation not by friction. The work piece around the tool melts partly by the stirring and the flow and energy equation is solved in this fluid part. In the other solid region, only the energy equation is solved. Then, how to define the fluid region is key issue for an accurate modeling of heat source. Two approaches are made in this study.

Model I: The fluid region can be modeled to form by natural consequences of rotating the contact area as depicted in Fig. 16(a). Only the contact area is forced to rotate and the plastic zone grows as heat spreads.

Model II: Another approach is to define rotation region around the tool like Fig. 16(b). This region is regarded as the plastic deformation zone and named rotation affected zone (RAZ). This approach requires the definition of detailed size of the zone.

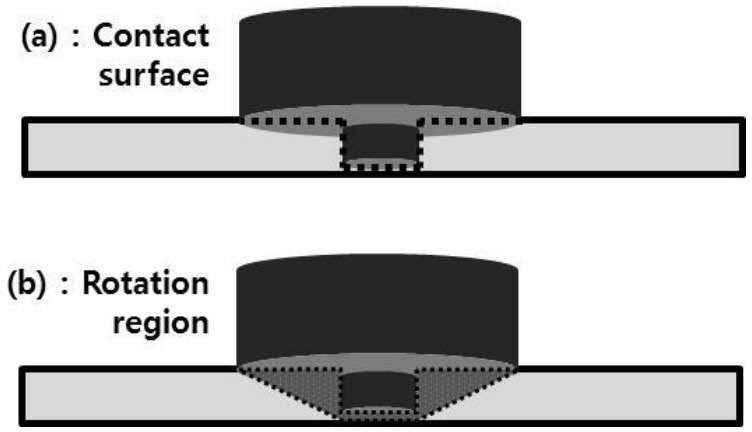

Fig. 16. Two different methods for rotating tool (a) Model I: Contact surface; (b) Model II: Rotation region.

In this study, the above defined models are simulated using CFD. For Model II, a parametric study is carried out for finding out the best shape of the rotation affected zone (RAZ) resulting in the closet heat distribution to

experiment results.

In this study, the CFD commercial program 'Fluent' is used for the FSW heat-flow analysis. The FSW heat-flow model is described in Fig. 17. The pin part of the tool is inserted into the RAZ and the shoulder part is contacted on the RAZ. The RAZ is placed inside the work piece. The properties of steel are assigned to the tool. The aluminum work piece and the RAZ are fluid regions so flow and energy equations are solved in these regions. The tool is a solid region so only the energy equation is solved in this region. As for the force equilibrium equation, the material at room temperature flows in at the inlet boundary (Plane A) and flow out at the outlet boundary (Plane B) with the welding speed. In order to understand the flow effect of the rotation tool, two methods were used. The rotating tool is realized as a rotating moving wall (Plane G) in Model I and rotating frame motion of RAZ (Volume B) in Model II. At the interface between the work piece and the tool (Plane G), the material was assumed to be in perfect contact (no slip) with the tool and rotate at the same speed as the tool. With this full sticking condition at the interface between the work piece and the tool, heat was generated only by plastic deformation without frictional heat. At all other boundaries (Planes C – F), except the boundary contacting with the tool (Plane G), a free traction boundary condition was applied. The boundary

condition and cell zone condition are summarized in Table 9 and 10, respectively.

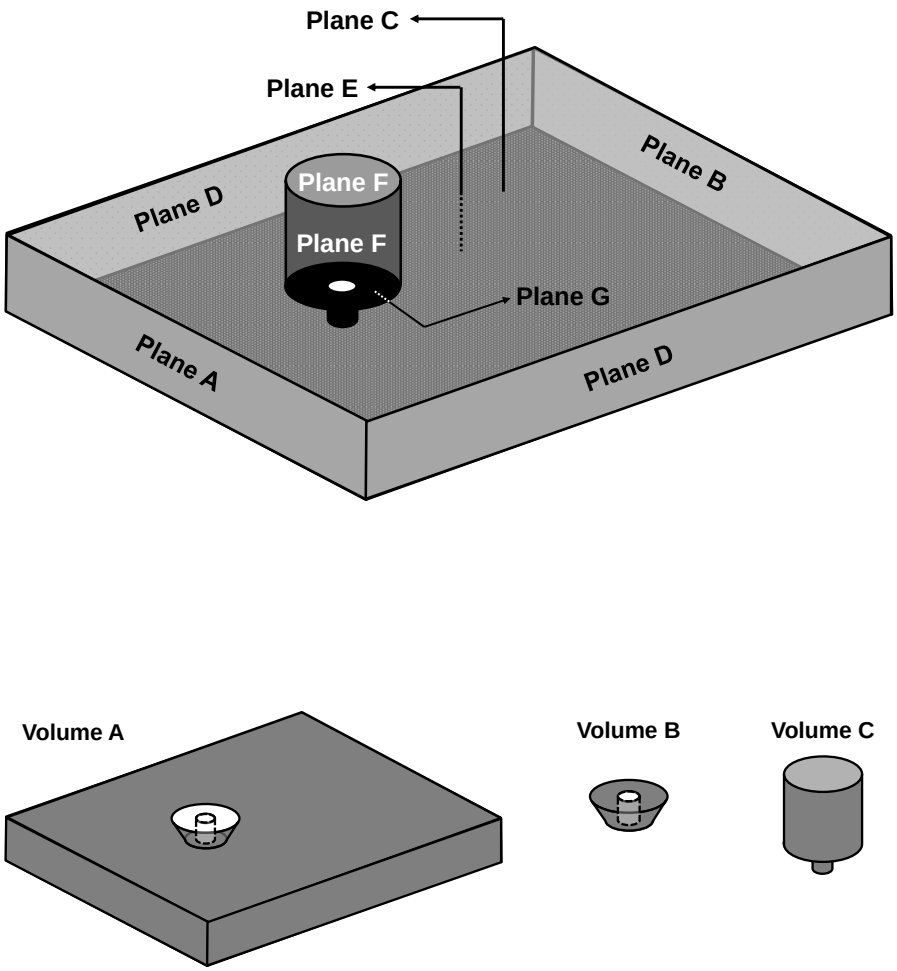

Fig. 17. Description of heat flow analysis model.

Table 9. Boundary conditions

Plane	Description	Applied condition	Heat equation condition	Heat transfer coefficients
A	Velocity-inlet	400 mm/min	20° C	-
B	Pressure-outlet	$\nabla\vec{v} = 0$	20° C	-
C	Free traction	-	20° C	h=30W/m2° C
D	Free traction	-	20° C	h=30W/m2° C
E	Free traction	-	20° C	h=200W/m2° C
F	Free traction	-	20° C	h=30W/m2° C
G	No slip (Heat induced by only plastic deformation)	600 (Exp.#1) and 800 (Exp.#2) RPM (Model I)	Q_p (Eq. 10)	h=200W/m2° C

Table 10. Cell zone conditions

Volume	Description	Force equilibrium condition	Heat equation condition
A	Fluid	-	-
B	Fluid	600 (Exp.#1) and 800 (Exp.#2) RPM (Model II)	Q_p (Eq. 10)
C	Solid	-	-

In general, a plastic deformation region is an affected

flow region by a rotating tool. The section of work piece is divided into 4 different macrostructures shown in Fig. 18 [40].

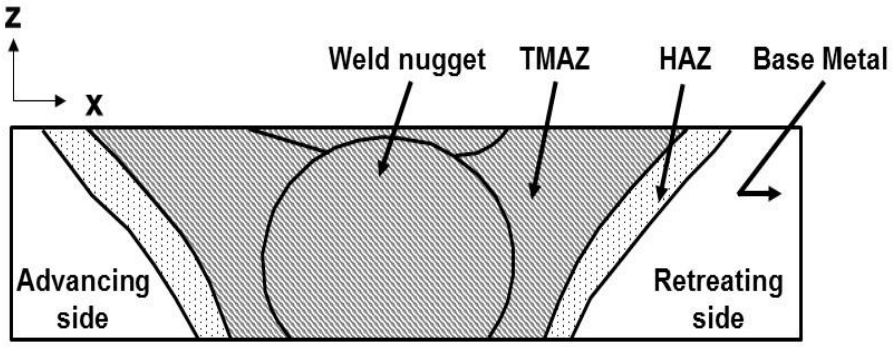

Fig. 18. The cross sectional macrostructure.

(i) Weld nugget or stir zone. This region is known to have a refined grain structure caused by roughly plastic deformation due to the rotation tool pin near the centerline. A feature of the stir zone is the occurrence of several concentric rings which has been called to as an onion ring. In addition, the flow arm is on the top surface of the weld and consists of material that is directly contacted by the shoulder. (ii) Thermo-mechanically affected zone (TMAZ). Plastic deformation occurs in this region by the tool. A plastic strain is produced without recrystallization. (iii) Heat affected zone (HAZ). This region has a change in the material properties and macrostructures as the welding center line closes. However, plastic deformation does not occur. (iv) Base metal or unaffected material. In

this region there is no change of any macrostructures and material properties. Thus, the size and shape of TMAZ is as important as the plastic deformation that occurs in this region. A plastic deformation heat is induced in TMAZ. In this study, the TMAZ assumes an appropriate region and this region is assumed as the RAZ. The RAZ is rotating at tool rotation speed and plastic dissipation occurs. In order to exactly define the RAZ, a parametric study is carried out as changing a few parameters to define the RAZ. In Fig. 19, ‘a’ is the shoulder diameter and increased at 1mm intervals, while ‘b’ is the pin diameter and also increased at 1mm intervals. The gap ‘c’ between the bottom of the pin and the bottom of the work piece is set at a very small constant value.

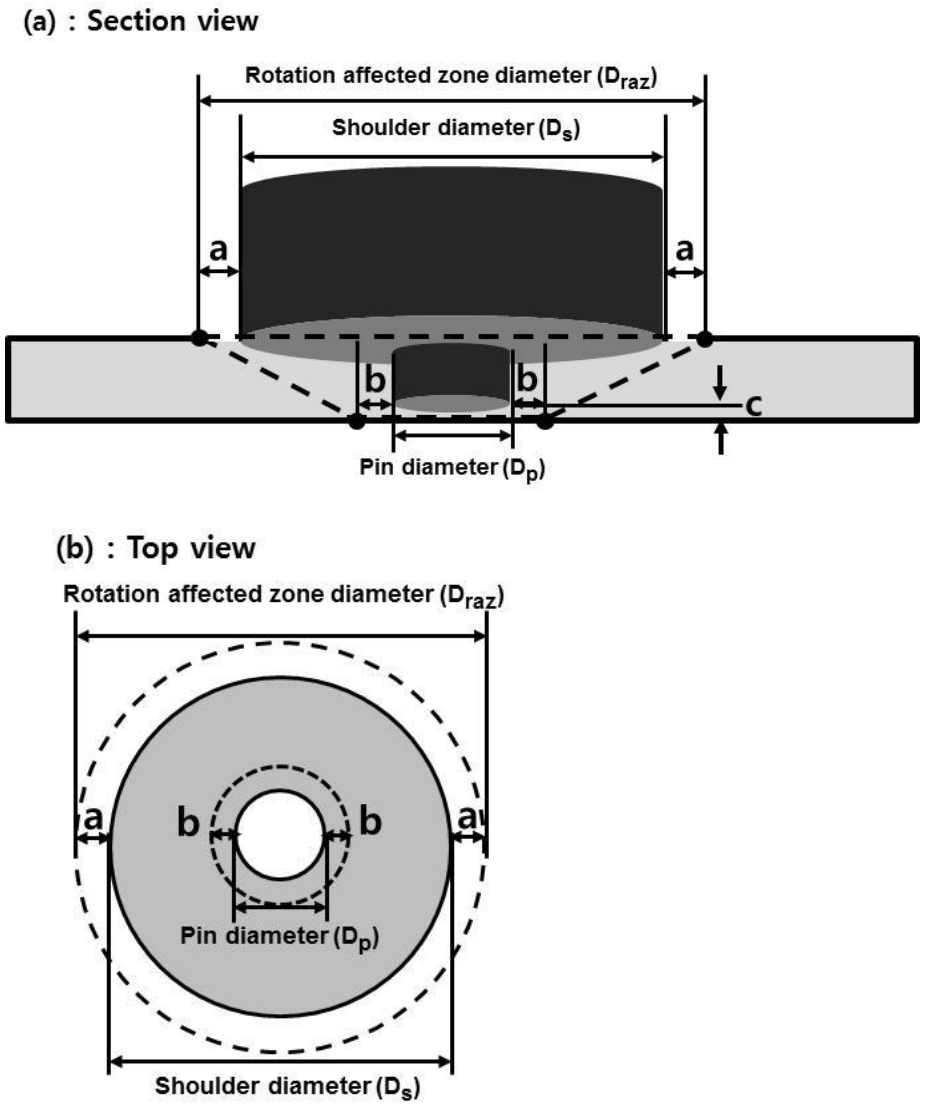

Fig. 19. Design variables for modeling of RAZ (a) Section view; (b) Top view.

The parametric study is carried out for various ranges of ‘a’ and ‘b’ which is listed in Table 11 for the heat-flow analysis of FSW. Furthermore, the temperature results of the parametric study are compared with the experimental results.

Table 11. The range of design variables (a, b) for parametric study.

	a (mm)	b (mm)	Increase range
Range	0 – 3	0 – 5	1 mm

The melting temperature of AA6061-T6 is 580℃. If the temperature of the 10mm distance from the welding centerline is over melting point, the results are not included in the study.

For the analysis of FSW, several assumptions are made so as to simplify the calculation of the analytical model.

· The aluminum work piece is treated as a non-Newtonian fluid.

· The heat is generated by only plastic deformation.

· A full sticking condition is applied to the contact boundary between the work piece and tool.

· The work piece is modeled as a viscoplastic flow and the tool is modeled as a solid.

The three governing equations are solved here. The material is assumed to be a single phase flow during the FSW. The equation of the continuity, the law of the conservation of the mass, is as follows:

$$v \cdot \nabla \rho + \frac{\partial \rho}{\partial t} = 0 \tag{7}$$

where v is the velocity of material flow, ρ is the density, and t is the time. $\partial / \partial t$ is zero in a steady state. Velocity vector v is calculated in inlet velocity (Plane A in Fig. 17) and rotation velocity (Plane G or Volume B in Fig. 17).

The momentum conservation equation is as follows:

$$\nabla \cdot \sigma + \rho b = \rho \frac{Dv}{Dt} \tag{8}$$

where σ is the Cauchy stress tensor which includes both pressure and shear, b is the acceleration of the body force, and D/Dt is the material time derivative. Free traction boundary conditions are applied at the Planes C – F boundary in Fig. 17, thus the stress is zero.

Since, the material is a time derivative term, the viscosity value is required. The viscosity can be calculated by the function of the flow stress and strain rate. If the material flow is adopted to model the large plastic deformation and high strain rate during the FSW, the deviatoric stress is in relation with the strain rate as follows:

$$S = 2\mu\dot{\varepsilon} \tag{9}$$

where, S is the deviatoric stress, μ is the viscosity, $\dot{\varepsilon}$ is the strain rate.

The strain rate is as follows:

$$\dot{\varepsilon} = \frac{\partial \rho}{\partial t} + \frac{\partial u}{\partial x} + \frac{\partial v}{\partial y} + \frac{\partial w}{\partial z} \tag{10}$$

where, u, v, and w represent the x, y, and z directions shown in Fig. 1.

The flow stress (effective stress) and effective strain rate is expressed in Eq. (11):

$$\bar{\sigma} = \sqrt{\frac{3}{2} S \cdot S}\,,\ \bar{\dot{\varepsilon}} = \sqrt{\frac{2}{3} \dot{\varepsilon} \cdot \dot{\varepsilon}} \tag{11}$$

where $\bar{\sigma}$ is the flow stress, and $\bar{\dot{\varepsilon}}$ is the effective strain rate.

By using Eq. (9) and Eq. (11), the viscosity can be expressed as function of the flow stress and effective strain rate as stated in Eq. (12):

$$\mu = \frac{\bar{\sigma}}{3\dot{\varepsilon}} \tag{12}$$

The effective strain rate is calculated in the Fluent. The flow stress calculation is based on the Zener-Holloman parameter [41]. Zener and Holloman found out that the effects of changes in strain rate and in temperature depend upon the stress and strain relation in the material [42]. The Zener-Holloman parameter is expressed in Eq. (13):

$$Z = \dot{\bar{\varepsilon}} \exp\left(\frac{Q}{RT}\right) = A(\sinh \alpha\bar{\sigma})^n \tag{13}$$

where α, n, and A are the material constants, Q is the activation energy and R is the gas constant. These values are listed in Table 12 for AA6061-T6 [37].

Table 12. Material constant and other values for AA6061-T6 [37].

α [MPa^{-1}]	n	A [S^{-1}]	Q [J/mol]	R [J/mol·K]
0.045	3.55	8.86× 106	145×103	8.314

Eq. (13) can be represented by the flow stress as follows in Eq. (14):

$$\bar{\sigma} = \frac{1}{\alpha} \ln \left\{ \left(\frac{\dot{\bar{\varepsilon}} \exp\left(\frac{Q}{RT} \right)}{A} \right)^{1/n} + \sqrt{\left(\frac{\dot{\bar{\varepsilon}} \exp\left(\frac{Q}{RT} \right)}{A} \right)^{2/n} + 1} \right\} \tag{14}$$

In Eq. (14), the flow stress is a function of strain rate and temperature.

The energy conservation equation is as follows:

$$\rho C_p \frac{DT}{Dt} = \nabla \cdot (k \nabla T) + \dot{Q} \tag{15}$$

where C_p is the specific heat, and $\dot{Q}$ is the heat generation rate due to plastic deformation in the work piece which becomes:

$$\dot{Q} = \gamma S \cdot \dot{\varepsilon} \tag{16}$$

where γ is the conversion factor and assumed 1.0 in this study.

The calculation flow chart is as in Fig. 20. If the difference of both is less than 0.1% as the change of the

flow velocity magnitude in the entire cell zone between N stage and N+1 stage are compared, it implies the solution is assumed to be converged.

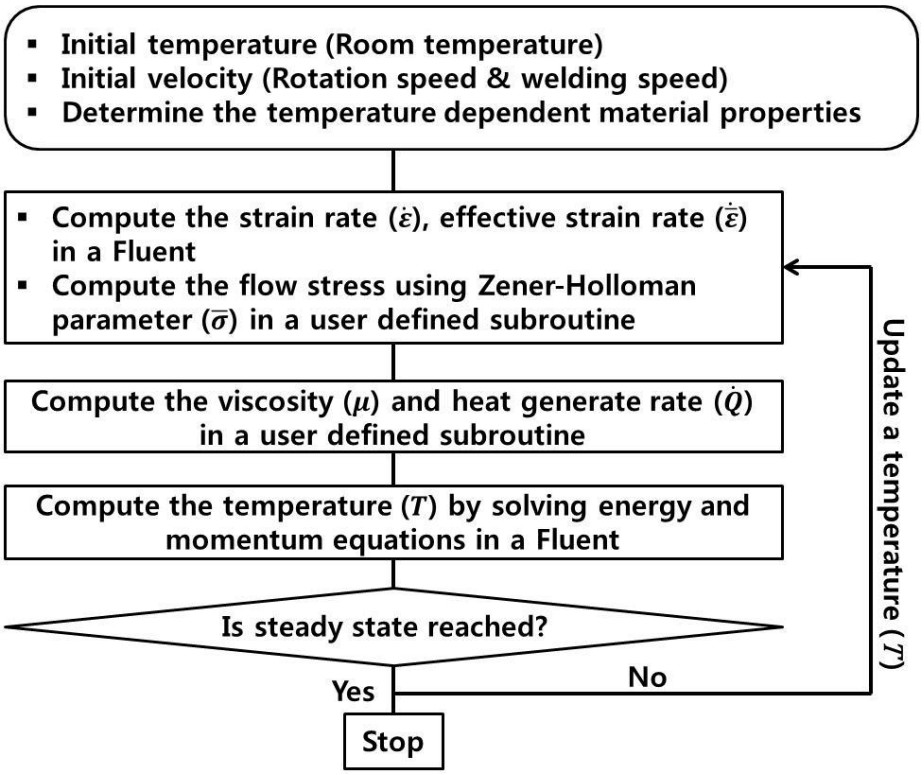

Fig. 20. Calculation flow chart.

In this study, heat transfer analysis is carried out in a steady state. Only the temperature distribution results of CFD are compared with the experimental results.

3. Heat transfer analysis results of three different methods

3.1. Heat transfer analysis results of CASE I

The parametric study was carried out with 24 cases. The temperature-change results for the simulation were compared with the Ref. #1 and Ref. #2 results. The three-dimensional simulation noted above was performed for the values listed in Table 8. Transient heat transfer analysis results of Ref. #1 is shown in Fig. 21. The Ref. #1 temperature history and distribution are plotted in Fig. 22 and Fig. 23, respectively; the Ref. #2 temperature history is plotted in Fig. 24.

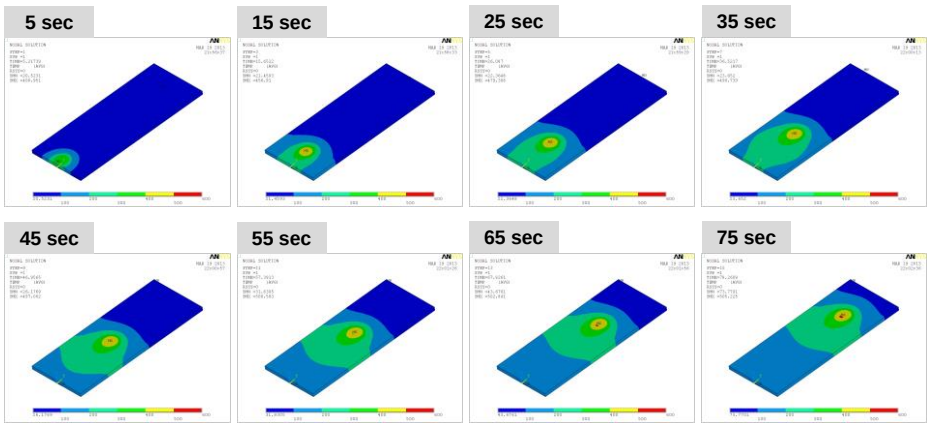

Fig. 21. Transient heat transfer analysis results of Ref. #1.

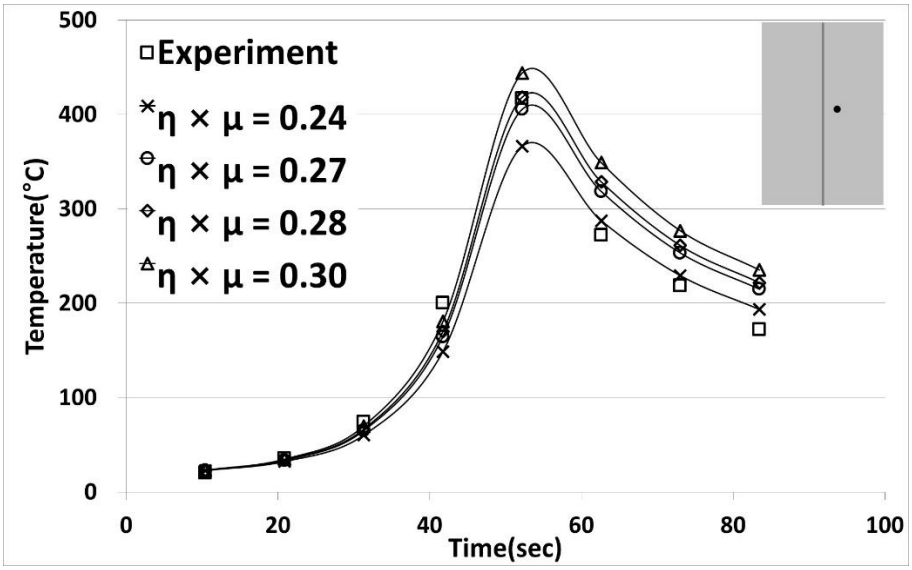

Fig. 22. Temperature history of parametric study results for CASE I and Ref. #1

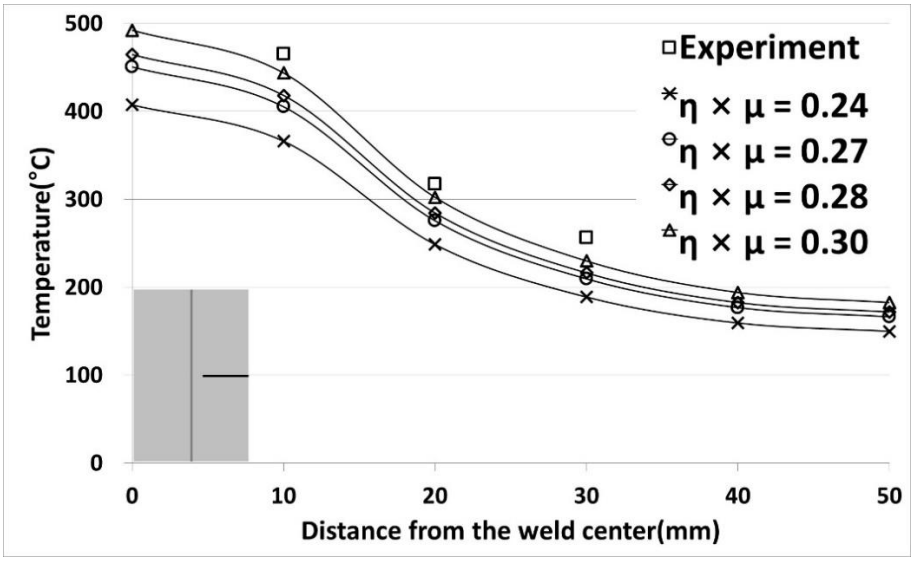

Fig. 23. Temperature distribution of parametric study results for CASE I and Ref. #1

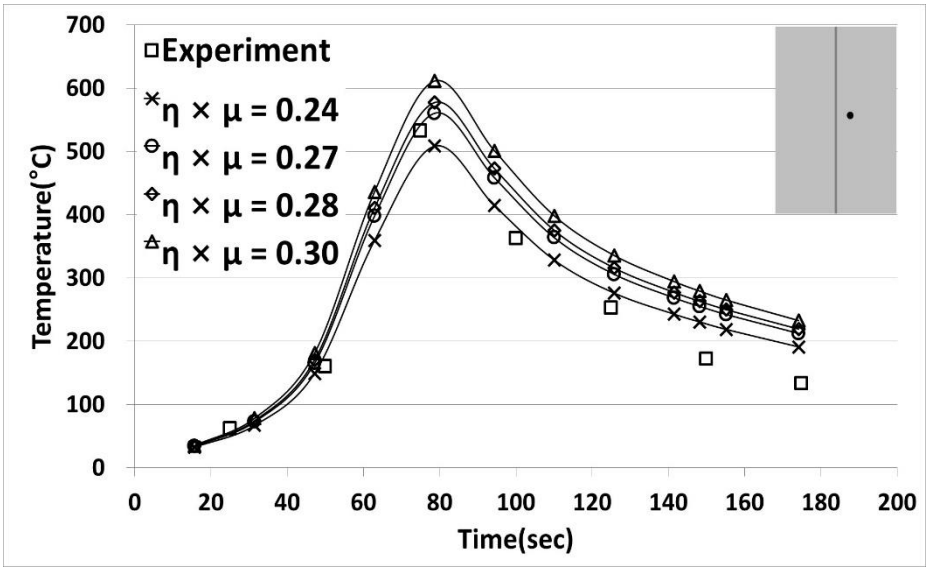

Fig. 24. Temperature history of parametric study results for CASE I and Ref. #2

In Figs. 22 – 24, there are some cases of good agreement with the experimental data. In Eq. (2), the welding efficiency and the friction coefficient are multiplied. Thus, the temperature-change results in the simulation were related to those values. The temperature distribution and the history results showed the best agreement with the experimental results when the welding efficiency and friction coefficient were multiplied and within the 0.27 – 0.30 range.

3.2. Heat transfer analysis results of CASE II

The three-dimensional simulation noted above was performed for the different cases listed in Fig. 11. Transient

heat transfer analysis results of Ref. #1 is shown in Fig. 25. The resultant temperature history and distribution for Ref. #1 are plotted in Fig. 26 and Fig. 27, respectively, and the resultant temperature history for Ref. #2 is plotted in Fig. 28.

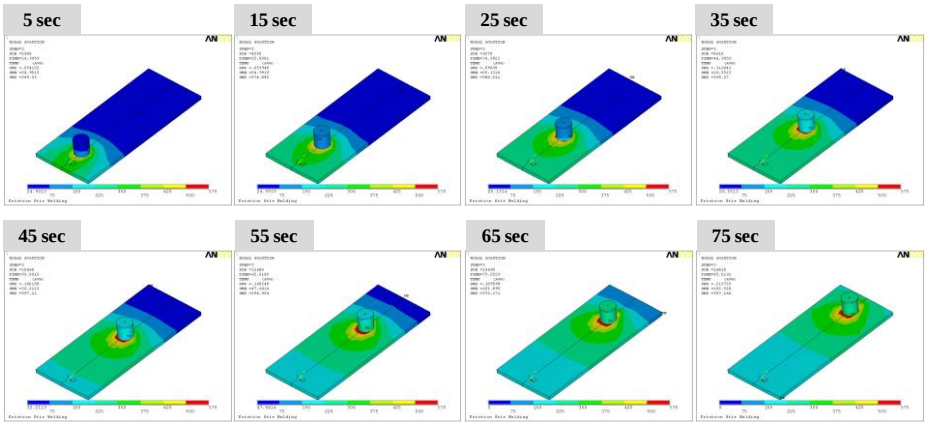

Fig. 25. Transient heat transfer analysis results of Ref. #1

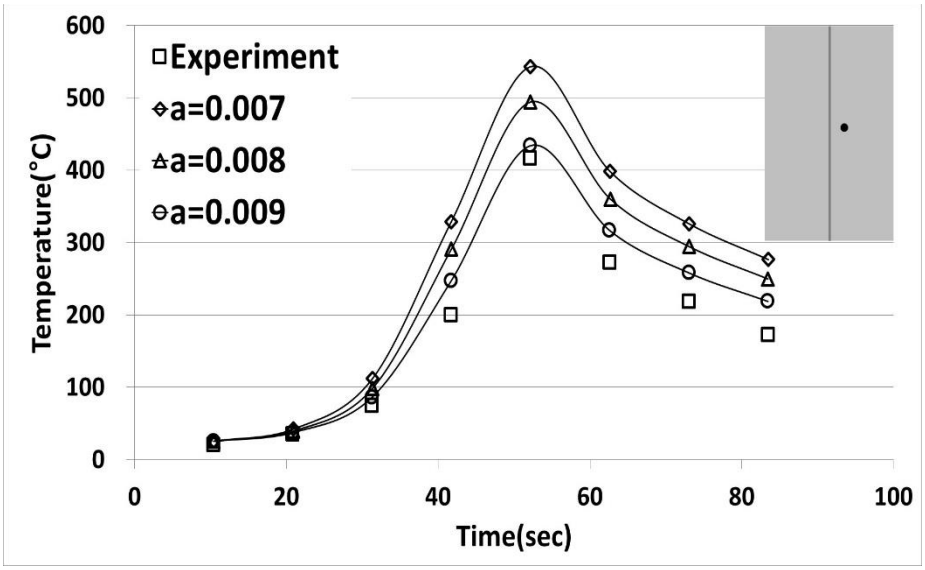

Fig. 26. Temperature history of parametric study results for CASE II and Ref. #1

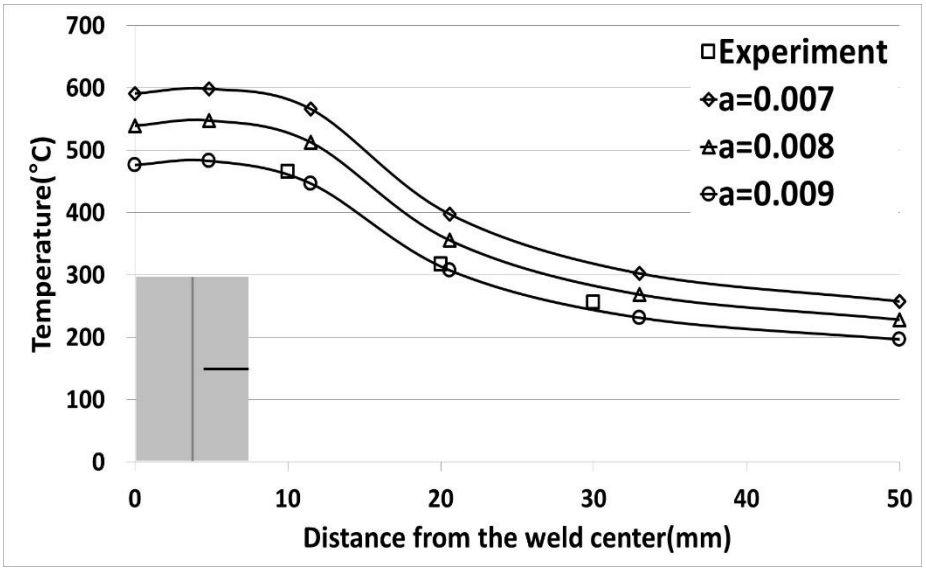

Fig. 27. Temperature distribution of parametric study results for CASE II and Ref. #1

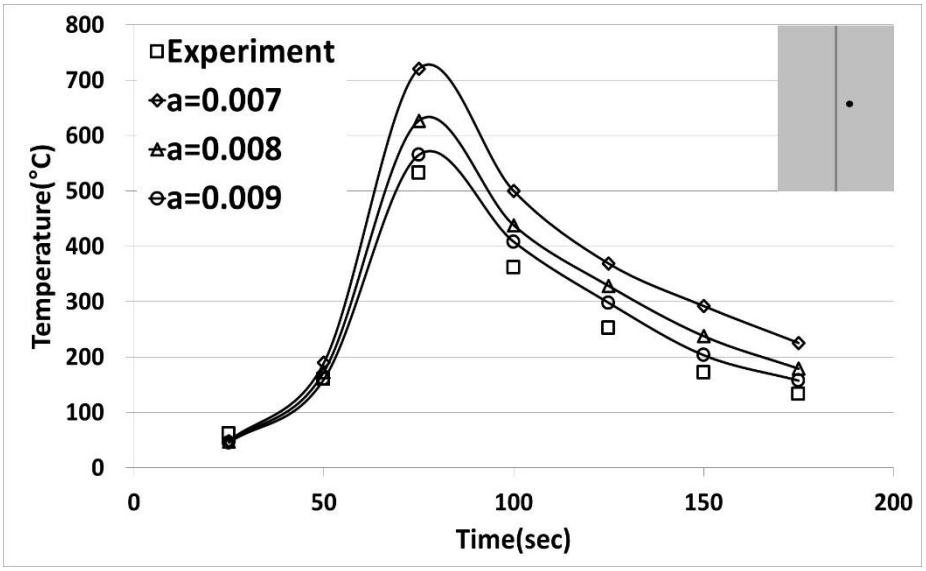

Fig. 28. Temperature history of parametric study results for CASE II and Ref. #2

The temperature distribution and history were in good agreement when the value of '*a*' was 0.009 in the temperature-

dependent friction coefficient in Eq. (6). In this simulation, the result of the temperature was very sensitive to the friction coefficient. An accurate assumption of the temperature-dependent friction coefficient is needed for simulation of FSW using a contact element.

The calculated frictional heat and plastic deformation heat based on time are plotted in Fig. 29 and Fig. 30, respectively. Clearly, the frictional heat is the greatest part of the total heat. As Fig. 29 indicates, the peak frictional heat is related to the material softening resulting from the temperature rises at the plunge and dwell stages.

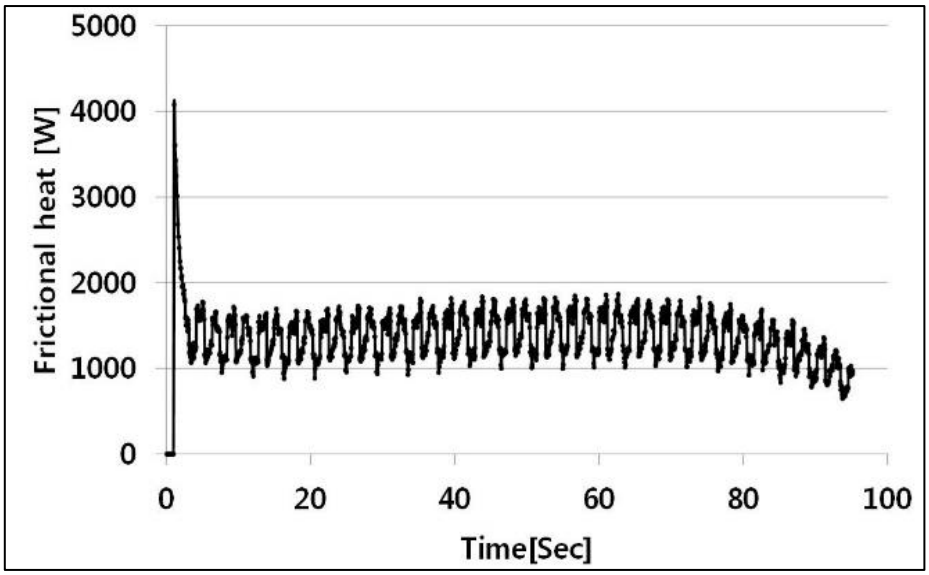

Fig. 29. Frictional heat of Ref. #1.

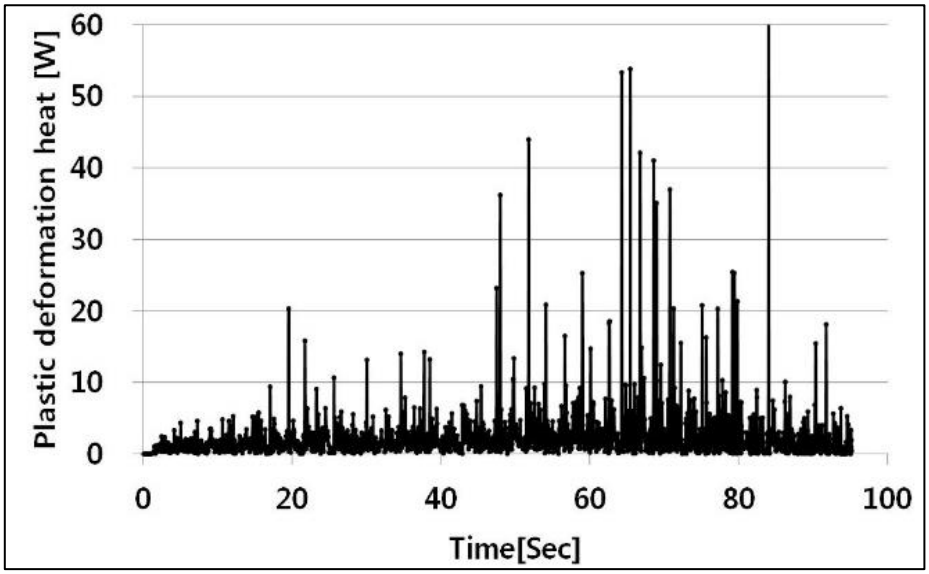

Fig. 30. Plastic deformation heat of Ref. #1.

In CASE II, the maximum frictional heat (Q_1) is 1884 W ,which is between the work piece and the tool shoulder in Ref. #1, whereas in CASE I, the frictional heat (Q_1) between the work piece and the tool shoulder has a constant value of 2115 W the entire time. In CASE II, the value of Q_1 is relatively small, due to the influence of nonlinearity behavior on heat transfer. Additionally, the convective heat transfer is less effective in CASE II than in CASE I, since the tool is modeled to prevent the contact of the surface with the air.

3.3. Heat transfer analysis results of CASE III

When the value of 'a' is 1 and the value of 'b' is 2 – 3 in Model II, the temperature results show the best agreement with the experimental results in both Ref. #1

and Ref. #3. They are collected in Fig. 31 and Fig. 32 along with Model I results. Also, all the cases remarkably show the asymmetry temperature distribution at approximately 10%. The temperature of the advancing side was higher than that of the retreating side. This is related to the strain rate. The strain rates are a measure of how fast the three velocity components change in each of the three directions. Heat generation is high under a high strain rate (Eq. 9 – 16). In CASE III, the strain rate values are higher on the advancing side than on the retreating side. Thus, the temperature is high on the advancing side.

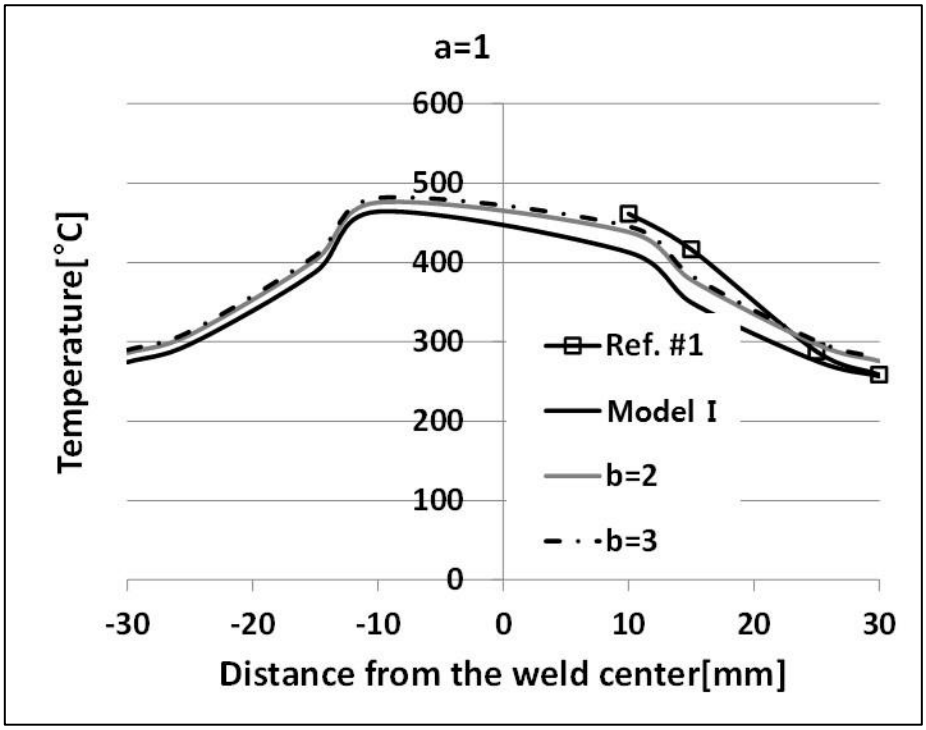

Fig. 31. Temperature distribution of parametric study results for CASE II and Ref. #1.

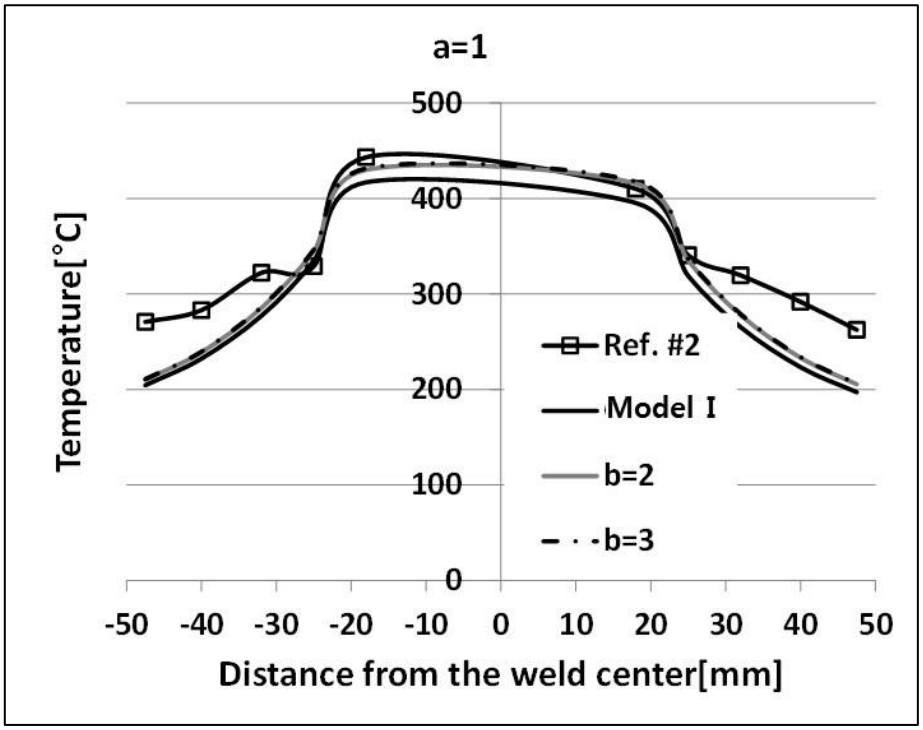

Fig. 32. Temperature distribution of parametric study results for CASE II and Ref. #3.

The streamlines near the tool are shown along with the strain rate, the velocity, and the temperature in Figs. 33 – 35, respectively. These streamlines were the results of Ref. #1. They were tangents to the velocity vectors, and were not changed under steady-state fluid flow. In Figs. 33 – 35, the streamlines complicatedly rotate around the tool. Considering that a no-slip boundary condition was applied at the contact boundary aspects between the work piece and the tool, the materials exhibited sticking behavior there. The strain rate of the material near the tool was much higher than in the other fields. And because temperature is a function of the strain rate,

the temperature also was relatively high near the tool.

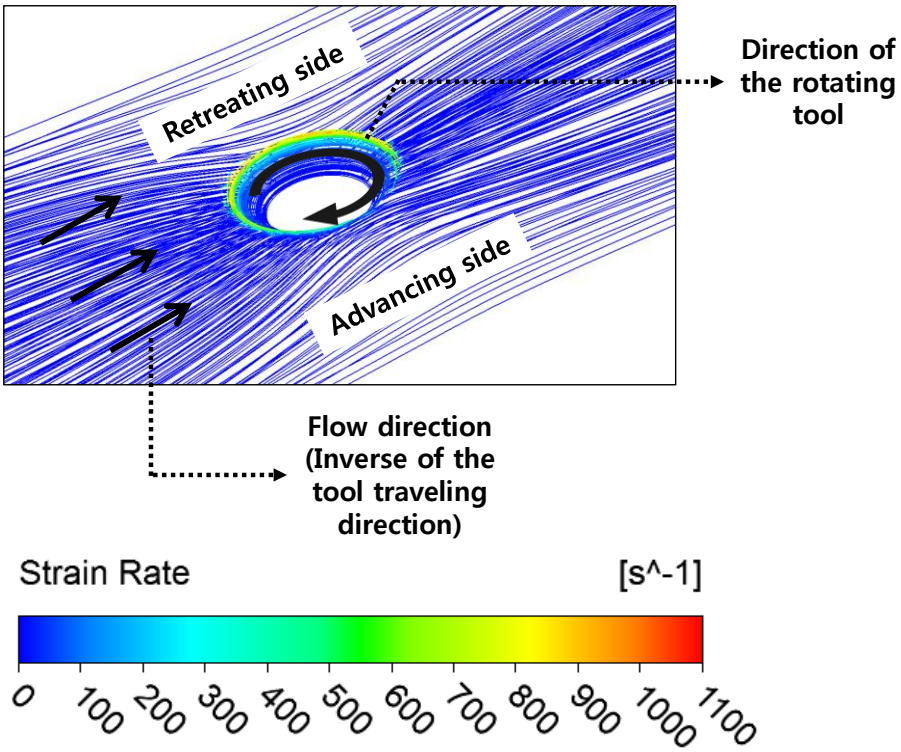

Fig. 33. Streamline with strain rate of Ref. #1.

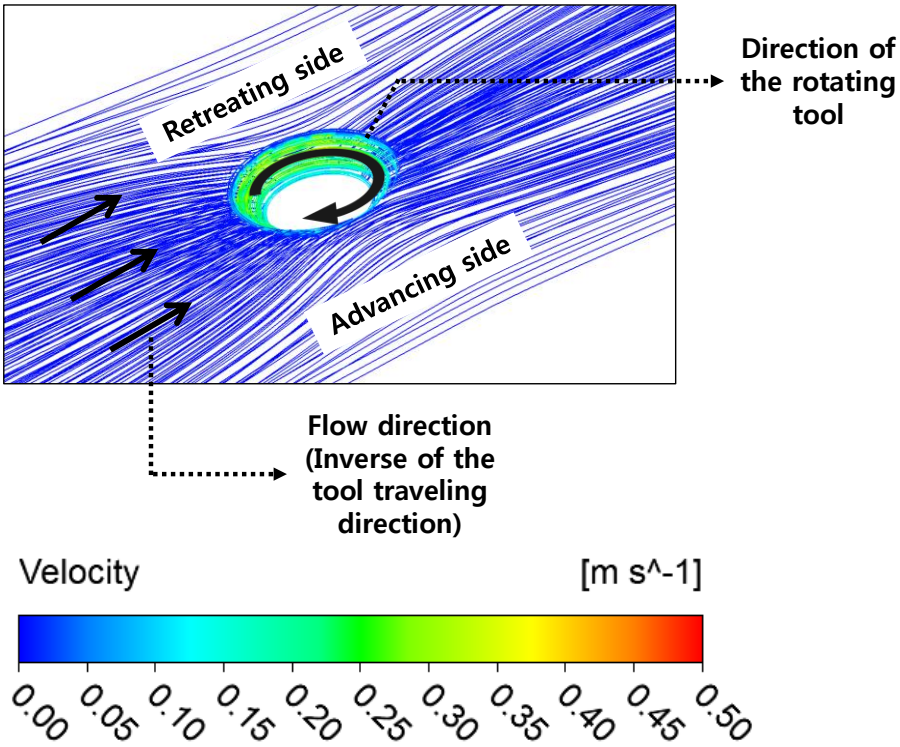

Fig. 34. Streamline with velocity of Ref. #1.

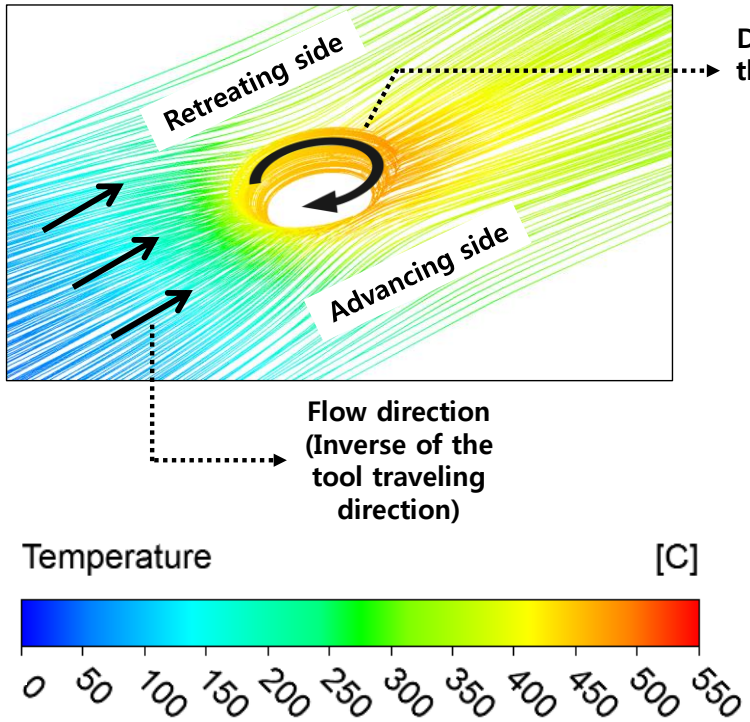

Fig. 35. Streamline with temperature of Ref. #1.

3.4. Summary of three different heat transfer analysis methods

Three different methods of heat transfer analysis were carried out for FSW simulation.

– CASE I is the simplest method, and analysis time is short. However, with this method, it is very difficult to determine the welding efficiency and the friction coefficient value. Thus, accurate experimental data, including the welding efficiency and the friction coefficient in each FSW experiment, is required.

- The CASE II method requires the temperature-dependent friction coefficient of AA6061-T6. This value is calculated on the basis of a comparison with the experimental temperature data. This value is possible to be used in the same material. However, it takes a very long time to simulate it due to the use of a contact element and the need to consider nonlinear behaviors. Moreover, it cannot consider the effect of the tool pin.

- CASE III calculates the temperature distribution under the steady state during the traveling stage. In the real traveling stage of FSW, the heat generation is almost constant. Thus, a FE model can use the temperature data obtained by the CASE III analysis. Then, transient analysis is practicable assuming a quasi-steady state during the traveling stage. Furthermore, the asymmetric effects of FSW, such as temperature and residual stress distributions, also can be considered. The analysis time is reasonable, and the RAZ is more moderate than other unspecified variables. The RAZ is the thermo mechanically affected zone, which is to say, the zone in which plastic deformation occurs. This region can be found as by cross-sectioning the macrostructure, or it can be deduced from the size of the tool. The simulation can reflect the whole shape of the tool.

4. Experiments of friction stir welding

Before, three different heat transfer analysis methods are compared and concluded that CASE III is the most efficient method. In this section, actual FSW experiments were carried out. After that, experimental results will be used to verify the simulation results.

FSW experiments are carried out in TAEKWANG TECH., and the machine No. 1 is used. The experimental equipment is configured as shown in Fig. 36. The aluminum alloy 6061-T6 (AA6061-T6) is used in this experiment.

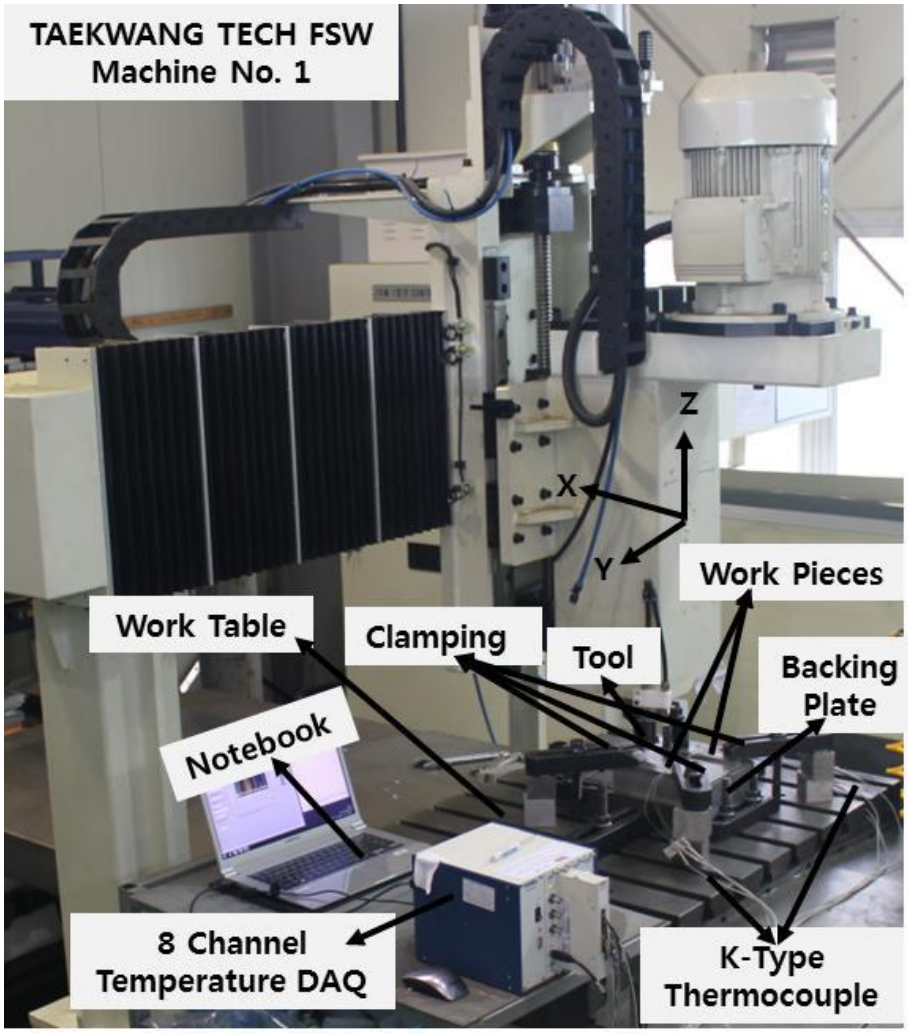

Fig. 36. The FSW experiment equipment.

The tool is made of alloy steel, and the dimensions are listed in Table 13. The welding parameters are listed in Table 14. For butt FSW, the height of the pin is slightly less than the thickness of the work pieces; and for T lap joint FSW, the diameter of the pin is slightly less than the web thickness of the work pieces. The FSW experiments were carried out under various conditions, for the relationship between the residual

stress, and the welding process parameters, such as rotation speed and welding speed. The shape of a work piece are indicated in Fig. 37 and Fig. 38. In this study, three different shape of T-joint FSW were carried out as shown in Fig. 38.

Table 13. The work piece and tool dimensions for the experiments

Plate Size			Tool Size (T1 / T2 / T3)		
W (mm)	L (mm)	t (mm)	Shoulder diameter (mm)	Pin diameter (mm)	Pin height (mm)
100	240	6	18 / 22 / 22	5	5.7 / 5.7 / 6.5

Table 14. The welding parameters of the experiments

Designation	Weld shape	Tool	Rotation speed (RPM)	Welding speed (mm/min)	Plunge depth (mm)
Exp. #1	Butt	T1	600	400	0.1
Exp. #2	Butt	T1	800	400	0.1
Exp. #3	Butt	T2	600	400	0.1
Exp. #4	Butt	T2	800	500	0.1
Exp. #5	Butt	T2	800	400	0.1
Exp. #6	T lap joint	T3	1000	300	0.1
Exp. #7	T lap joint	T3	1000	600	0.1

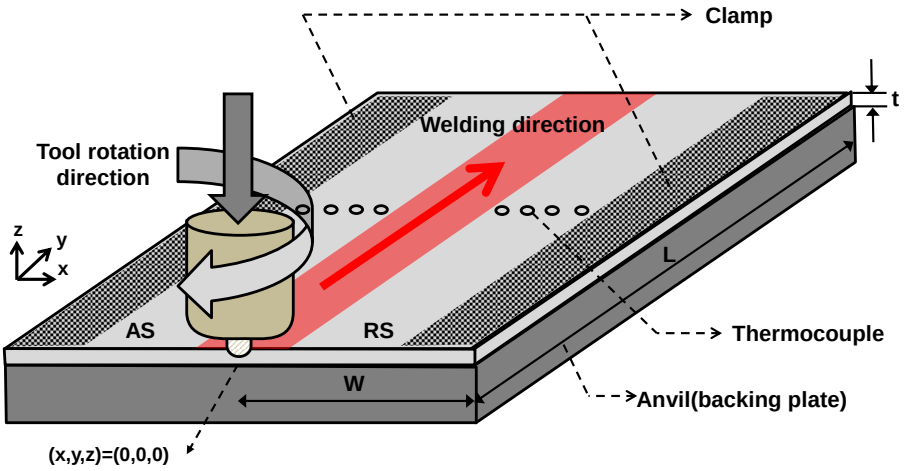

Fig. 37. The configuration of butt FSW experiment

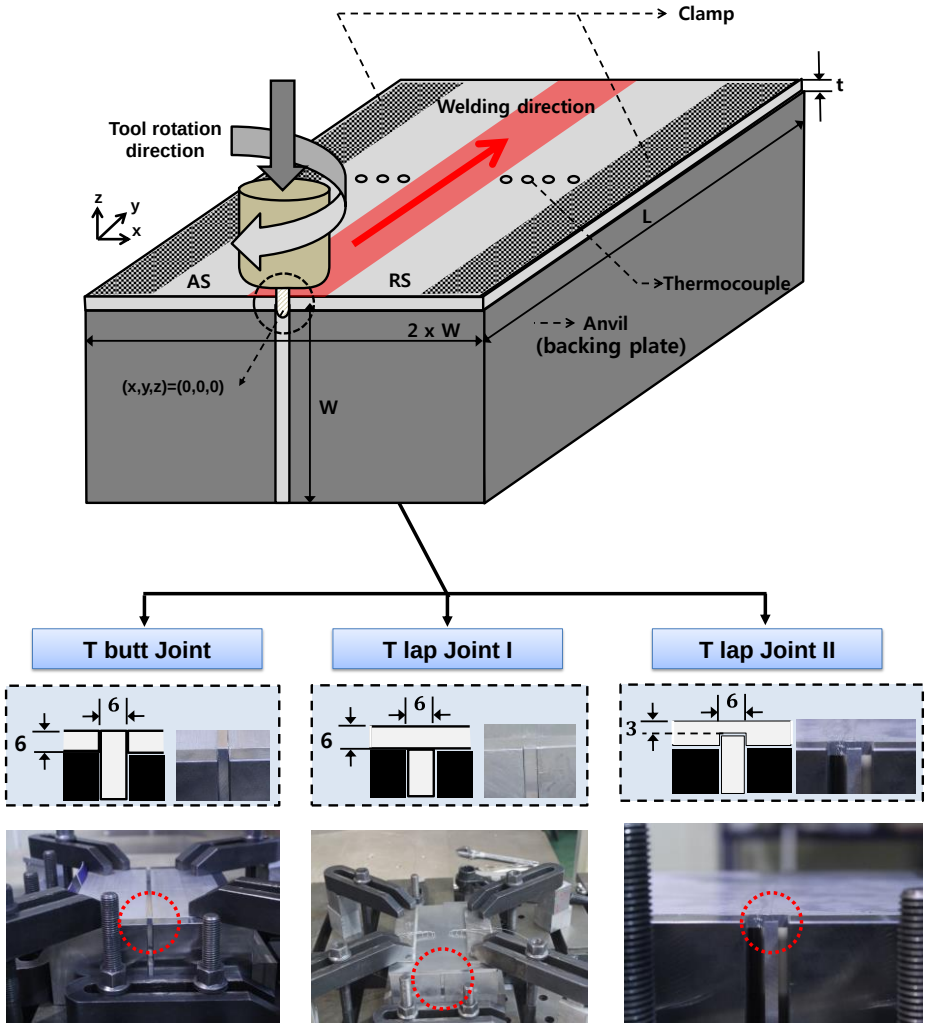

Fig. 38. The configuration of three different T-joint FSW experiments

In this experiment, all the other welding parameters are kept the same. The FSW machine is of the tool plunge depth control type, and this depth is kept at 0.1mm during welding. The tilt angle is zero. The welding starts 20 mm from the edge of the work piece, and stops 20 mm from the opposite side edge.

8 K-Type thermocouples are used to measuring the temperature during the FSW. The locations of thermocouples are 15, 20, 30, and 40 mm from the welding centerline from

side-to-side, and 3 mm below the top surface as shown in Fig. 39. National Instrument 8 channel temperature data acquisition equipment is used. The temperature data are saved in the notebook, and the software is coded using Labview 2009. Fig. 40 is a diagrammatic representation of the entire FSW experimental process.

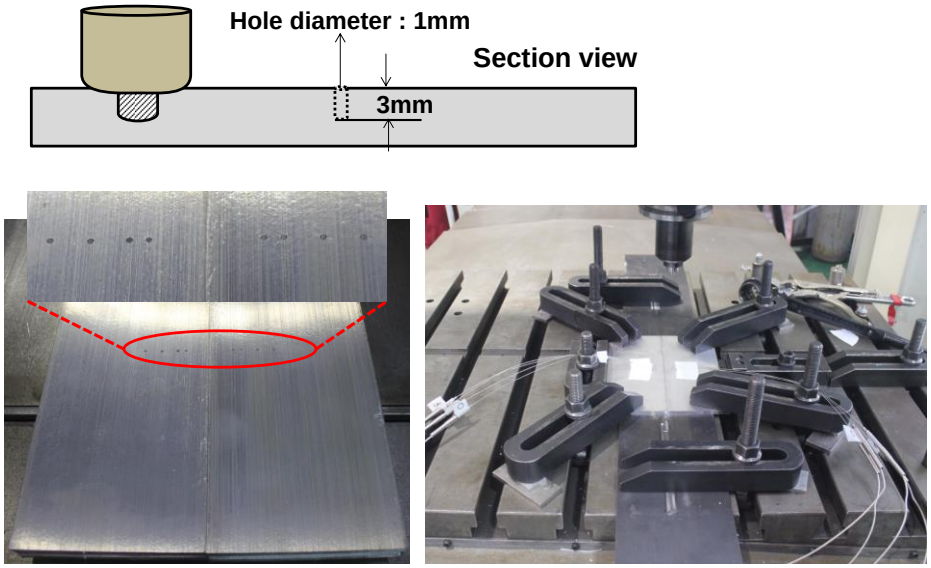

Fig. 39. Installation of thermocouple

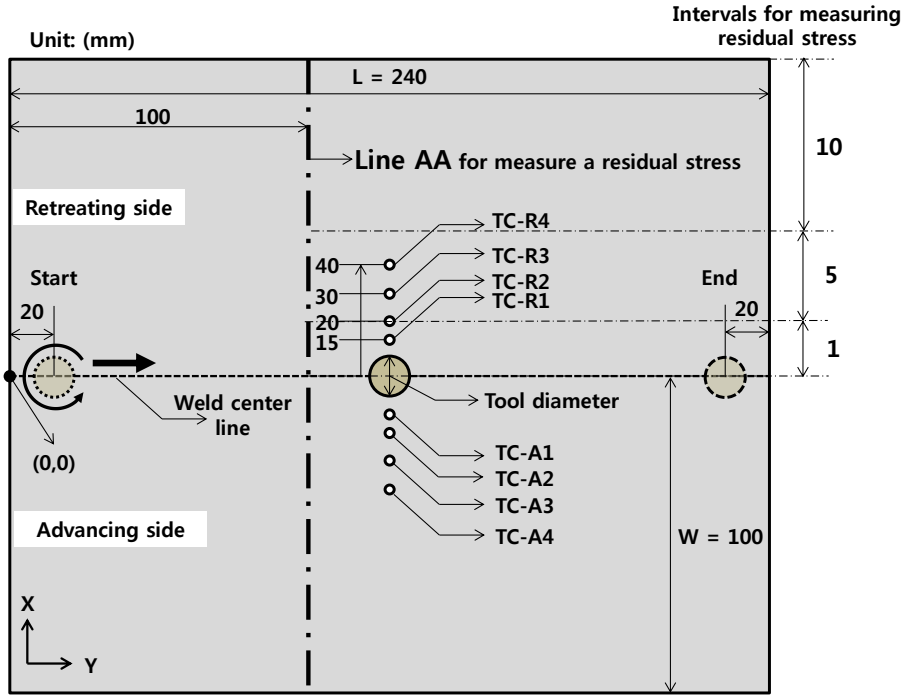

Fig. 40. The entire FSW experimental process

The backing plate material is mild steel. The work pieces are fixed by clamping each plate. A special jig is made for the T lap joint FSW, and prevents movement of the work piece during the T lap joint FSW. During the FSW process, the fixing of a work piece is very important for weldability. Fig. 41 shows the jig shape and size for the T lap joint FSW. Extremely low rotation speeds with fast welding speeds caused some problems for FSW. An initial rotation speed of the tool of 200 RPM does not penetrate into the work pieces as shown in Fig. 42(a). In the case of 400 RPM – 800 mm/min (the first number refers to the rotation speed of the tool and the second refers to the welding speed), the dwelling stage is fine, but the tool pin

breaks during the traveling stage as shown in Fig. 42(b, c). This means that the work pieces are not sufficiently softening to stir the work piece by the tool pin.

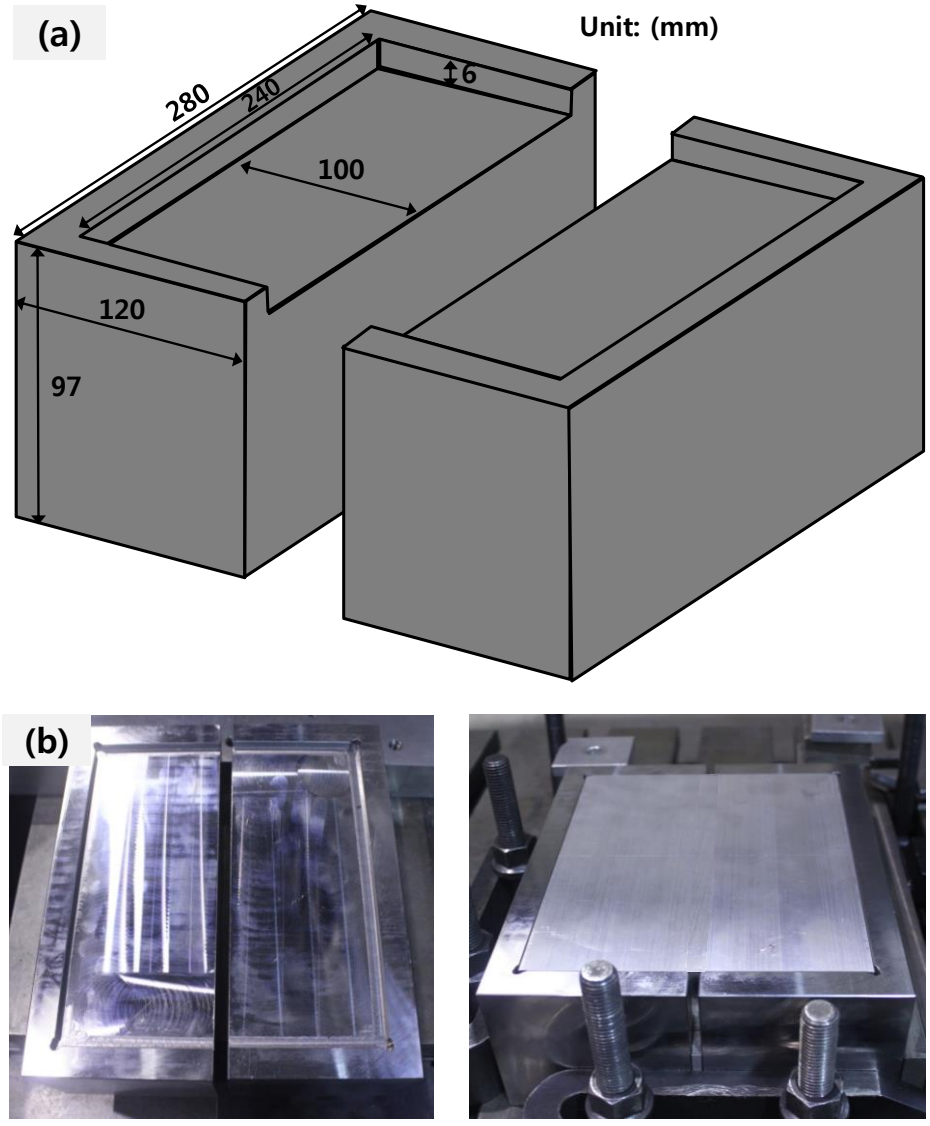

Fig. 41. Special jig for T-joint FSW (a) A schematic diagram; and (b) Real jig.

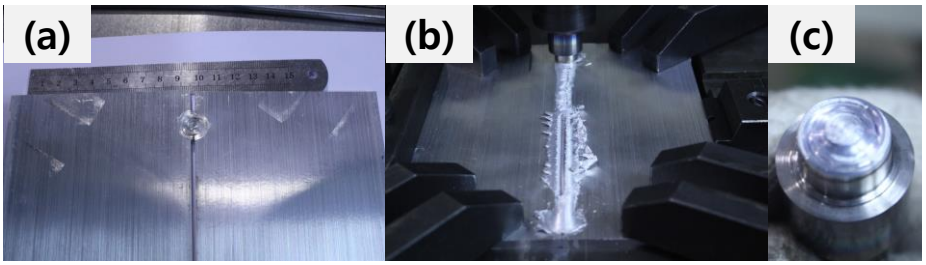

Fig. 42. The failed experiments

The welded work pieces and the tool are displayed in Figs. 43 – 45.

Fig. 43. Butt FS welded work piece

Fig. 44. T-joint FS welded work piece

Fig. 45. Tool for FSW experiments

All the experimental temperatures are measured by thermocouples. Temperature distribution is measured in a perpendicular direction to the welding line when the tool is located at the weld center line. The experimental measuring locations are listed in Table 15.

Table 15. The experimental measuring locations. (The x, y, and z coordinates are shown in Fig. 2)

	Temperature distribution (x_1 – x_8 mm), (y mm), (z mm)
Coordinates	(−40, −30, −20, −15, 15, 20, 30, 40), (120), (3)

The temperature measured in the experiment is used to verify the validity of the CASE III methods.

5. Comparison with experimental and simulation temperature results

5.1. Welding dimension and parameters for heat transfer analysis

Before, seven different experiments were carried out. In this section, two butt FSW heat transfer analysis results are compared with the experimental results and discuss in depth. The description of heat transfer analysis models are summarized in Table 16.

Table 16. Heat transfer analysis model for comparison.

Designation	Weld shape	Tool	Rotation speed (RPM)	Welding speed (mm/min)	Plunge depth (mm)
Exp. #1	Butt	T1	600	400	0.1
Exp. #2	Butt	T1	800	400	0.1

5.2. Heat transfer analysis results and discussions

The CFD results of the temperature distribution on the work piece and the streamline with the temperature in the vicinity of the tool in Exp. #1 are depicted in Fig. 46 (a) and

Fig. 46(b), respectively. The streamlines are tangents to the velocity vectors and it is not changed in a steady state fluid flow. In Fig. 46(b), the streamlines rotate in a complex manner around the tool. Due to the fact that a no-slip boundary condition is applied at the contact boundary region between the work piece and the tool, materials have a sticking behavior there.

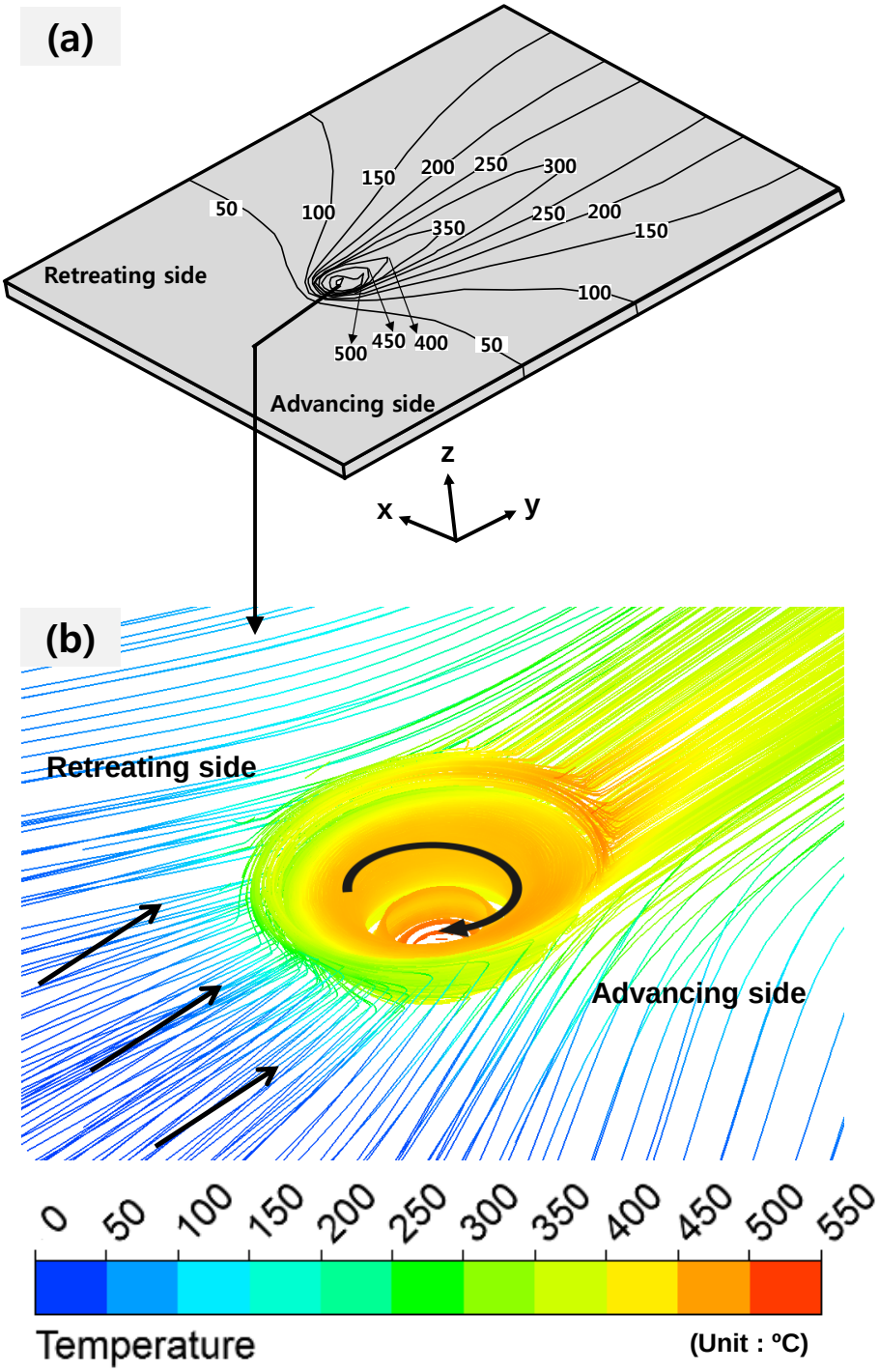

Fig. 46. CFD simulation results of Exp. #1 (a) The temperature distribution; (b) The streamline with the temperature.

As mentioned before, heat transfer analysis method of CASE III is carried out in a steady state. Only the temperature distribution results of CFD are compared with the experimental results. Fig. 47 and Fig. 48 depict the compared results of Exp. #1 and Exp. #2 for Model II, respectively.

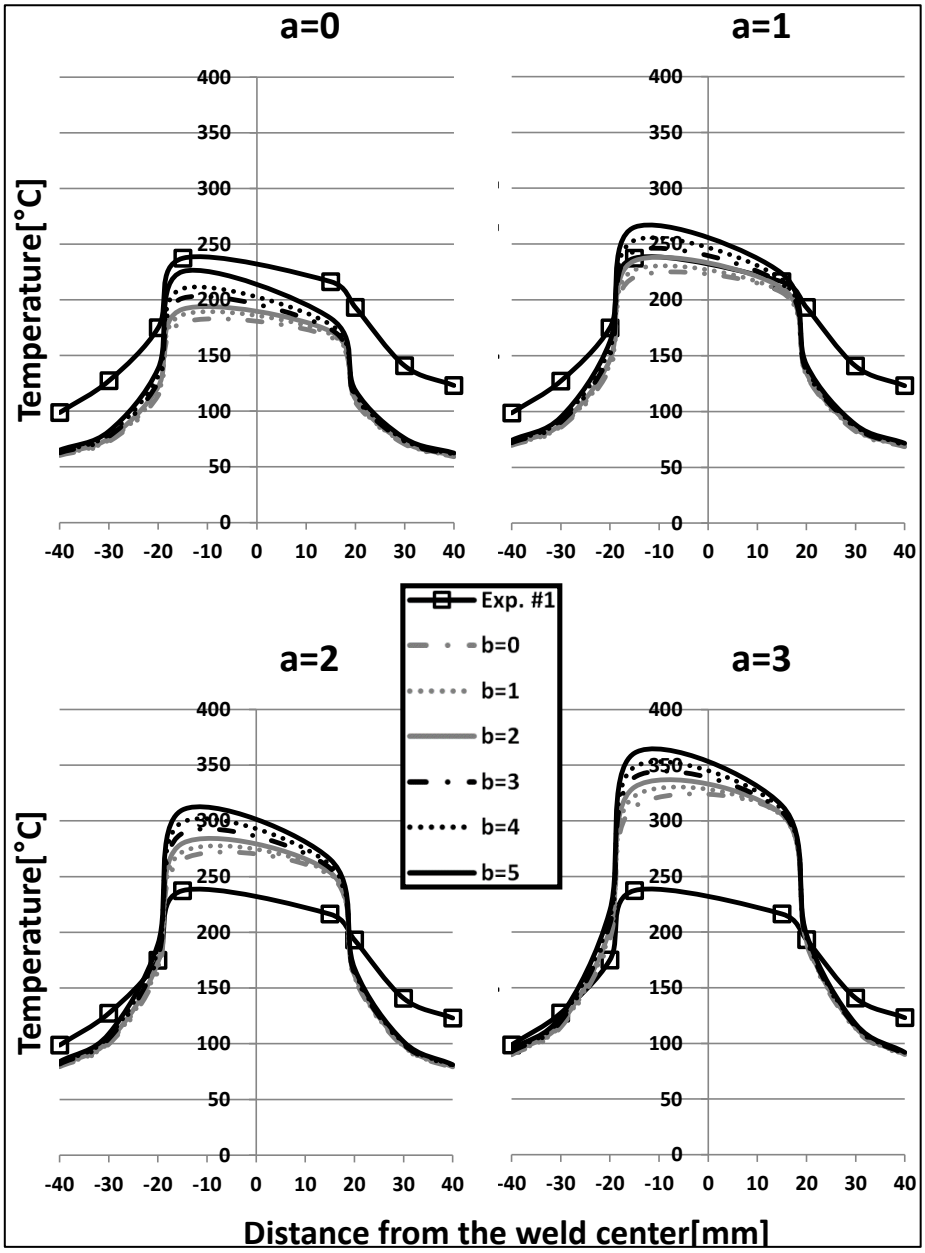

Fig. 47. Temperature distribution of parametric study results of Exp. #1

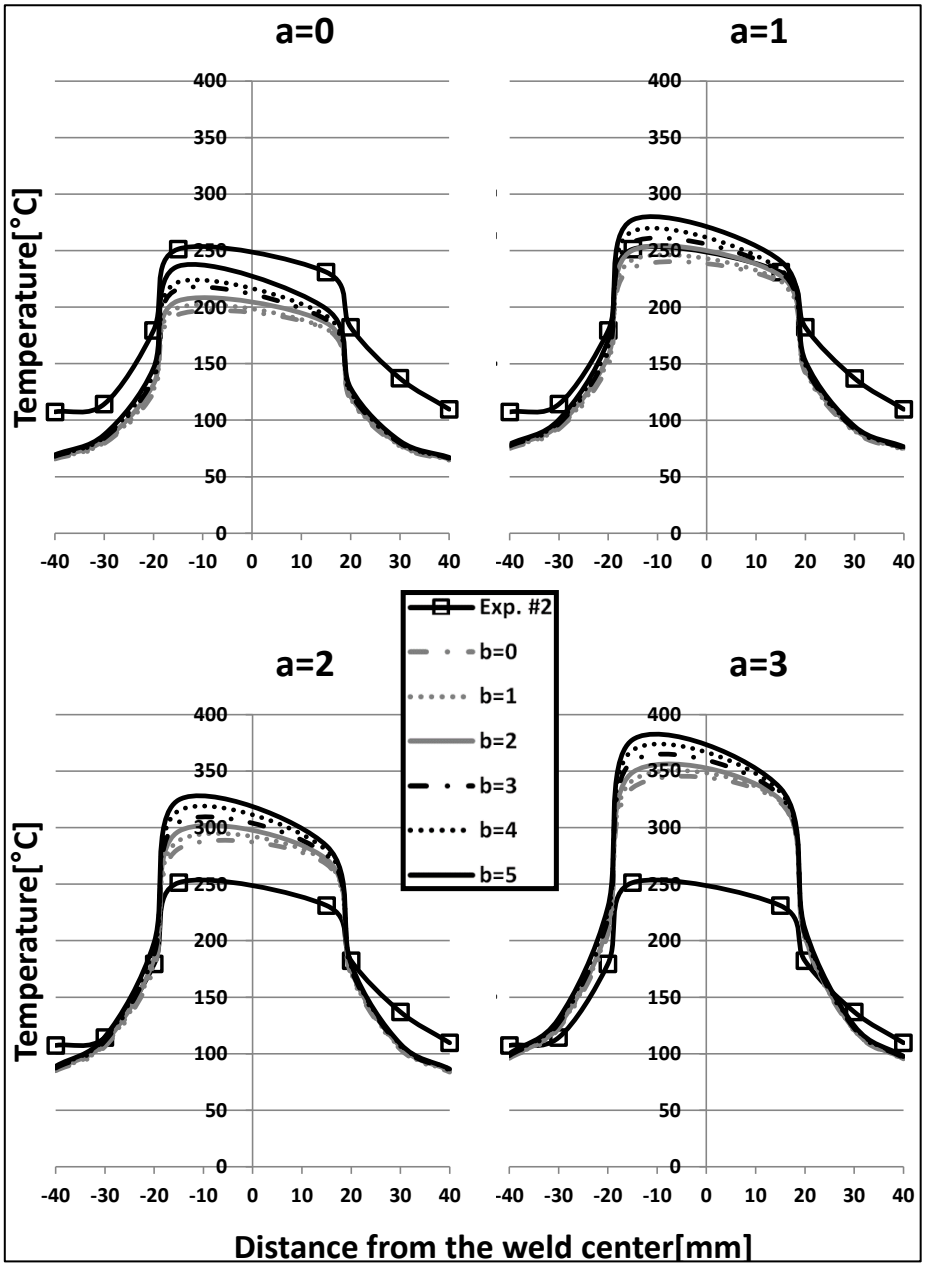

Fig. 48. Temperature distribution of parametric study results of Exp. #2

When the value of ‘a’ is 1 mm and the value of ‘b’ is 2 – 3 mm in Model II, the temperature results show the best agreement with the experimental results in both Exp. #1 and

Exp. #2. They are collected in Fig. 49 along with Model I results. Also, all the cases remarkably show the asymmetry temperature distribution at approximately 10%. This is why the tool has the direction of rotation. The side of the welding tool where surface motion is the same direction as the travel direction is referred to as the advancing side (AS). The opposite side, where surface motion opposes the travel direction, is referred to as the retreating side (RS). The temperature of AS is higher than the temperature of RS due to its higher contact speed.

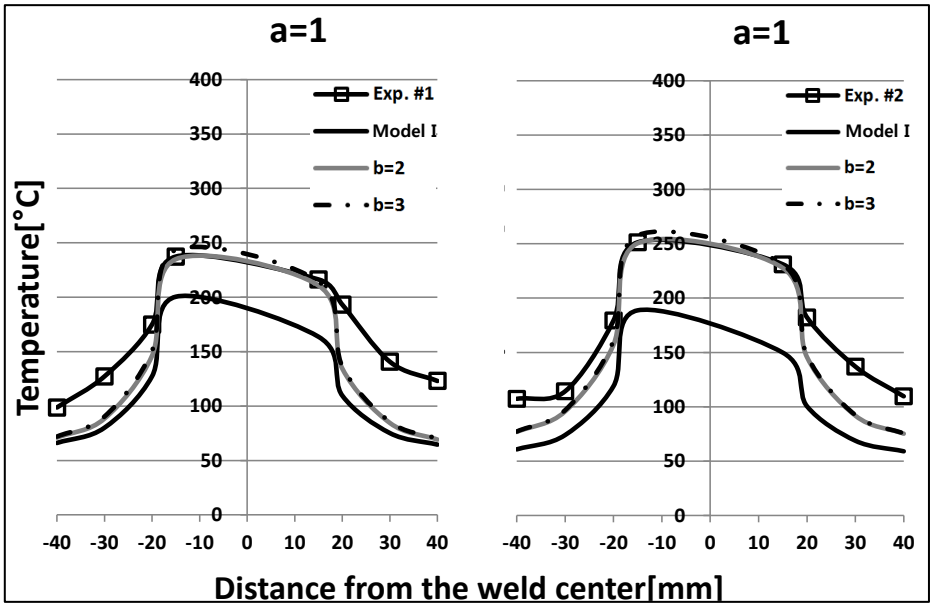

Fig. 49. Model I and most well matching Model II cases with Exp. #1 and Exp. #2.

In Fig. 49, the temperature distribution of Model I is lower than the experimental results. When rotating a contact surface,

the affected flow from rotating is insufficient compared with TMAZ. Thus, the plastic deformation induced heat is smaller than the heat from rotating the RAZ and the overall temperature distribution is lower.

The heat transfer analysis of FSW is affected by lengths ‘a’ and ‘b’. Using analysis of variance (ANOVA), effect on maximum temperature of the parameters (lengths of ‘a’ and ‘b’) is evaluated. In order to assess the influence of factors (‘a’ and ‘b’) on response (maximum temperature), main effects analysis is carried out using Minitab. The results of main effect analysis are depicted in Fig. 50 and Fig. 51. In Fig. 50 and Fig. 51, the slope of ‘a’ is higher than ‘b’. The increase of the value ‘a’ leads to larger volume change of RAZ than the value ‘b’. Moreover, the increased outer strip experiences the largest strain rate and plastic dissipation. Therefore, the increase of the value ‘a’ results in steeper growth of maximum temperature than the value ‘b’.

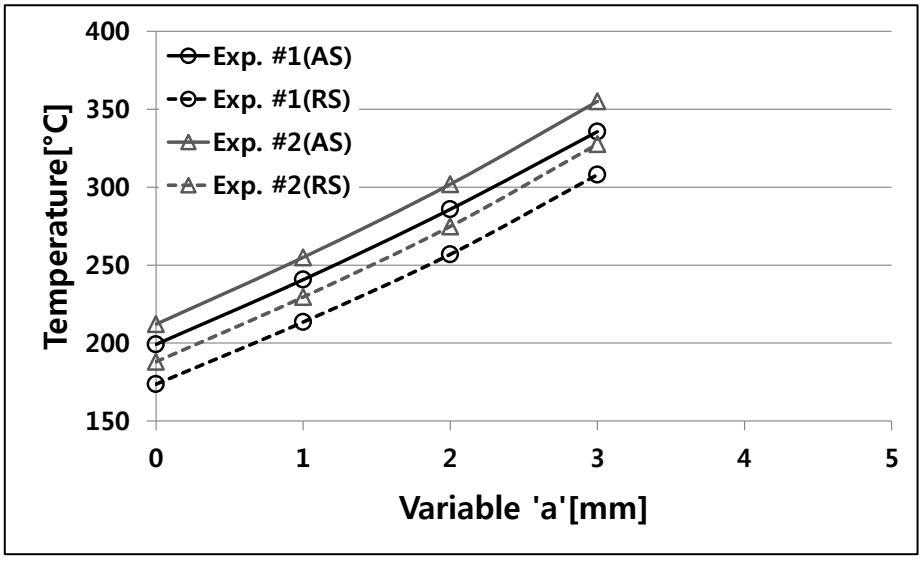

Fig. 50. The main effect plot for temperature with variable 'a'.

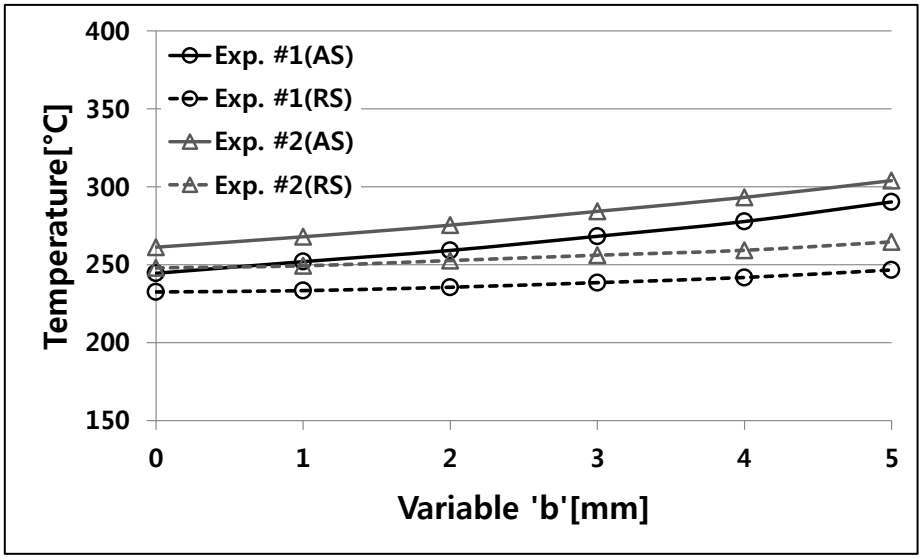

Fig. 51. The main effect plot for temperature with variable 'b'.

In order to verify the relationship between size of RAZ and cross sectional macrostructure of FSW, sectional structure inspections were carried out. For the sectional structure inspections, there are 3 steps. First is the polishing and hot

mounting. In this step, the polishing is the process of creating a smooth and shiny surface like a mirror by rubbing a specimen or using a chemical action, leaving a surface with a significant specular reflection. Hot mounting takes place under pressure in a mounting press, where the specimen is placed in a cylinder together with the appropriate mounting resin. Green resin is used in this experiment. A temperature of up to 200℃, and a pressure of up to 50kN are then applied during the embedding of the specimen. Fig. 52 and Fig. 53 show a polishing process and hot mounting.

Fig. 52. Polishing process.

Fig. 53. Hot mounting specimen.

Second, after finishing a polishing and hot mounting, is an etching process. Etching is the process of using strong acid or mordant to cut into the unprotected parts of a metal surface to create a design in intaglio in the specimen. In this study, etching solution was used in a 1:2 mixture of ethanol and HCl 66%. The process of etching is depicted in Fig. 54.

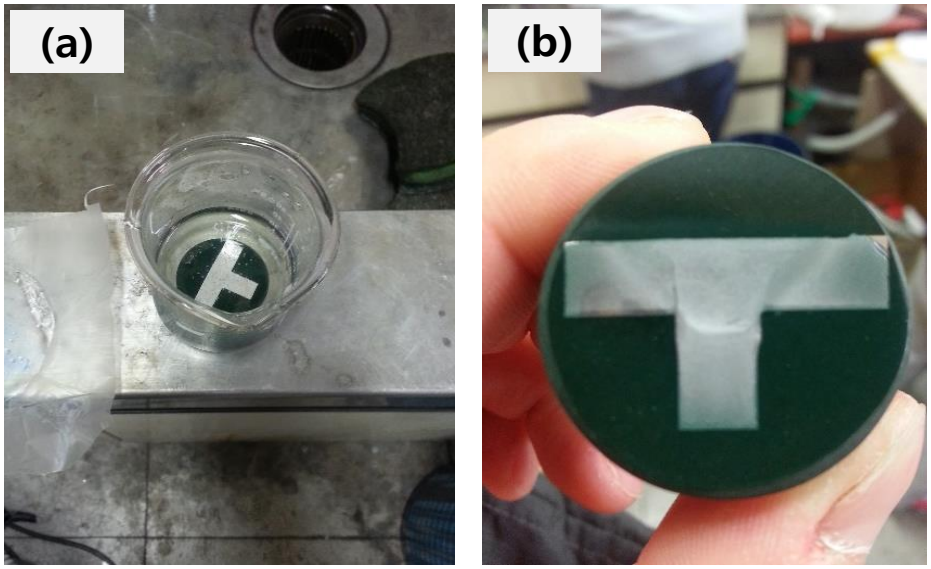

Fig. 54. Etching process (a) Specimen in the etching solution; (b) Finish the etching process.

Finally, cross section of the specimen was taken a photograph by using an electron microscope as shown in Fig. 55. Specifications of electron microscope is Olympus JP/BX51M. Figs. 56 – 58 show a cross sectional macrostructure of Exp. #1 and Exp. #2, respectively. Fig. 58 indicates three different weld shape (T-joint) of a cross sectional macrostructure of Exp. #7.

Fig. 55. Olympus JP/BX51M electron microscope.

Fig. 56. The cross sectional macrostructure of Exp. #1.

Fig. 57. The cross sectional macrostructure of Exp. #2.

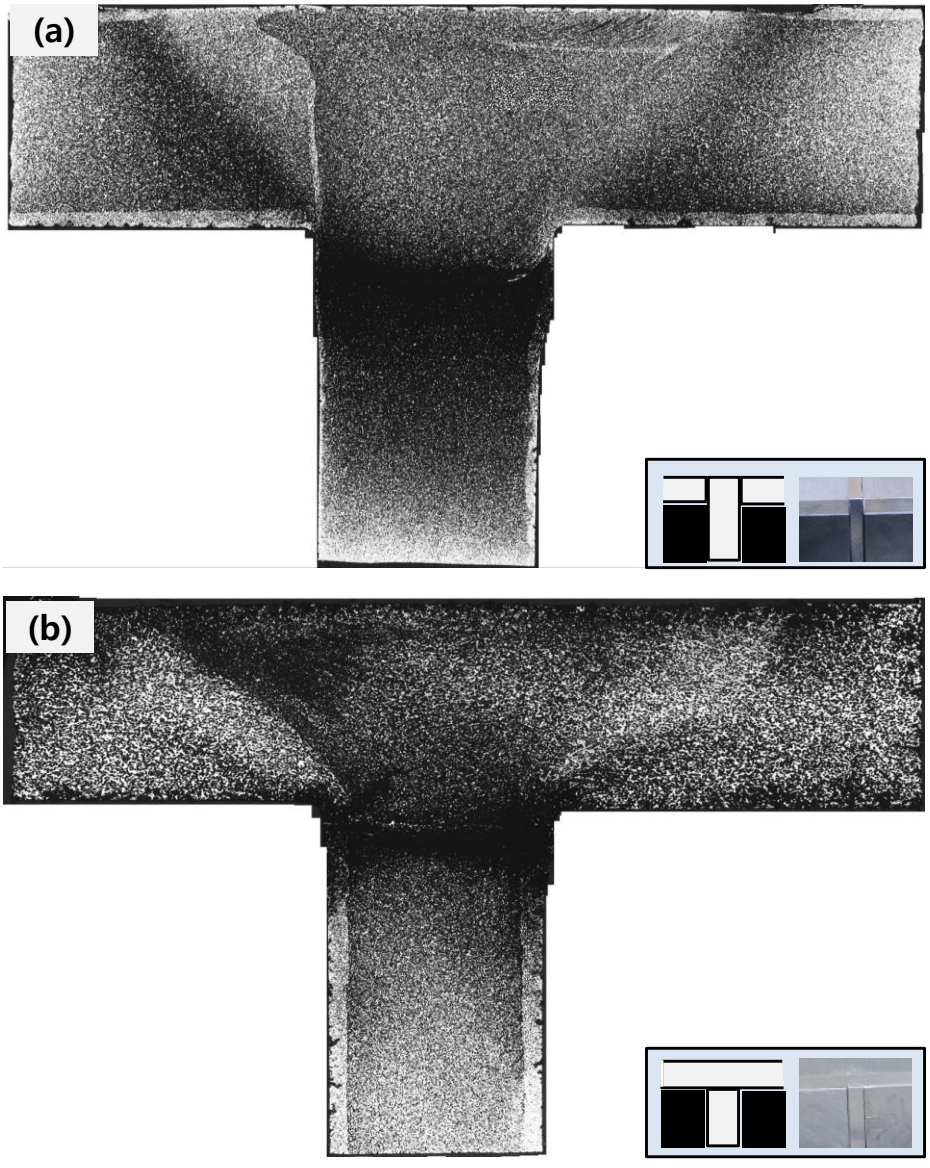

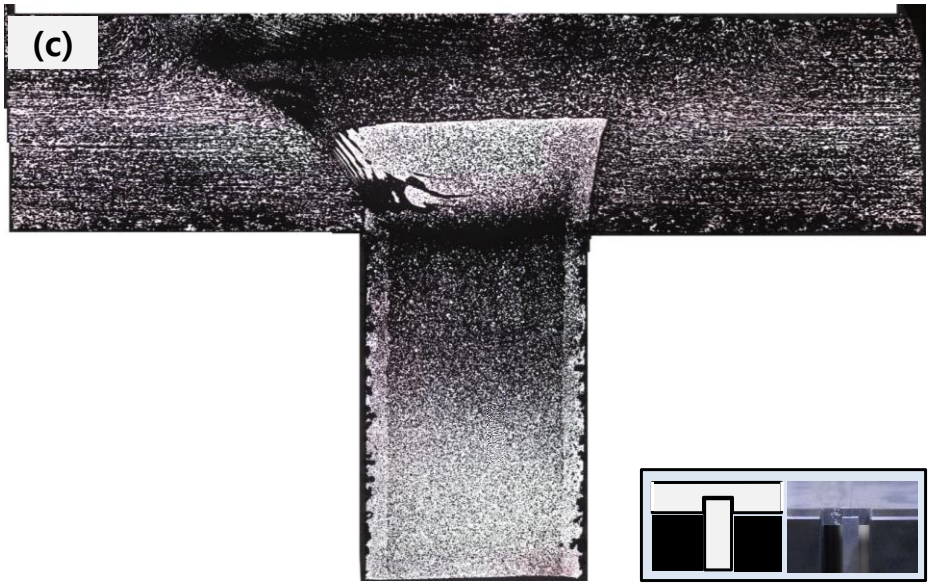

Fig. 58. The cross sectional macrostructure of Exp. #7 (a) T butt joint; (b) T lap joint I; (c) T lap joint II.

Fig. 59 and Fig. 60 are marked the weld nugget, TMAZ, HAZ, and base metal of Exp. #1 and Exp. #2, respectively.

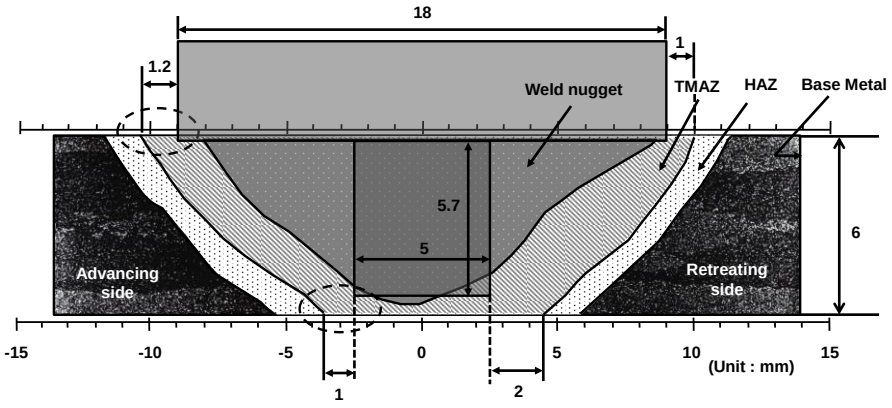

Fig. 59. Marked the weld nugget, TMAZ, HAZ, and base metal of Exp. #1.

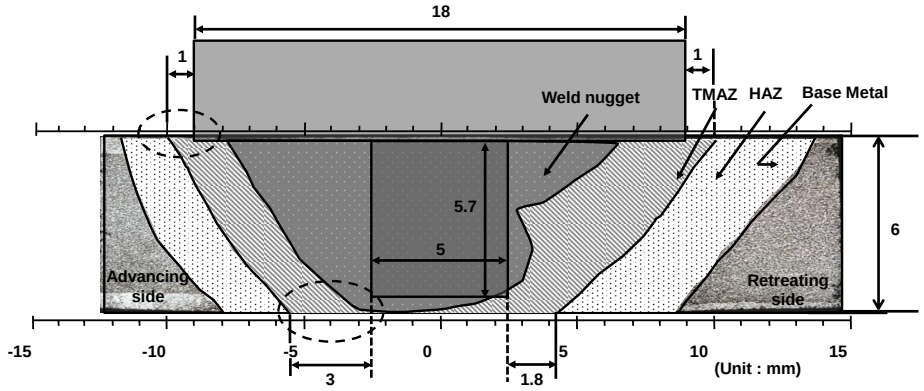

Fig. 60. Marked the weld nugget, TMAZ, HAZ, and base metal of Exp. #2.

A cross sectional macrostructures of the FSW process are depicted in Fig. 59 and Fig. 60. The TMAZ is larger than the tool size. The upper TMAZ size is approximate 1mm larger than the shoulder radius and the lower TMAZ size is 2 – 3 mm larger than the pin radius (marked using dot circles). This observation matches well with the size of RAZ summarized in Fig. 49.

In order to implement the current flow effects of the rotating tool, Model I and Model II were introduced. In order to identify the difference between two models, velocity distribution at the cross section of Exp. #1 is depicted in Fig. 61. Fig. 61 compares three different analysis results with each other. (a) is the results of a=1, b=3 in Model II which matches best with the experimental results. (b) is when a=3, b=3 in Model II and when the temperature is much higher than the experimental results. (c) is the results of Model I of when the tool and only the contact surface is rotated. As shown in Fig. 61,

the difference of velocity distributions between Model I and Model II in the cross section is very much evident. As identified in Fig. 61(c), because only the contact surface is rotated in Model I, high velocity distribution appears near contact areas. On the other hand, when looking at (a) and (b) of Model II, it can be confirmed that the velocity distribution is all the way inside the affected RAZ region. It is also observed that the velocity of the advancing side is higher than the retreating side.

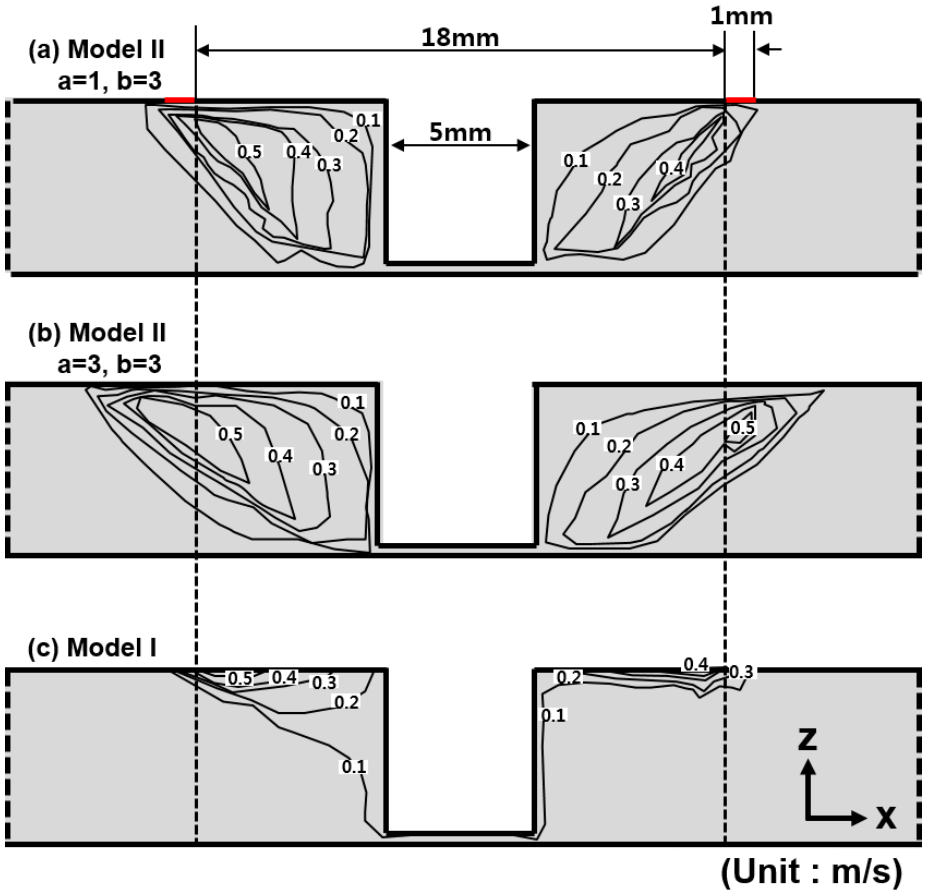

Fig. 61. The cross sectional velocity distribution of Exp. #1.

The cross sectional temperature distribution is shown in Fig. 62. In Fig. 61, the velocity value is high at both ends of the rotation boundary. This is because the velocity becomes higher as it gets farther from the center of the tool. The temperature distribution is bound up with the strain rate and the strain rate is a measure of how fast the velocity changes. Thus, the velocity value is related to the temperature distribution. Looking at Fig. 67 and Fig. 68, Model II has a wider velocity distribution and has a higher temperature than Model I. In Fig. 61(a), when the RAZ area most similar to the TMAZ area from Fig. 59 is rotated, the experimental results are the most consistent with Exp. #1. Furthermore, just as in Fig. 61(b), when the RAZ area is set up bigger than the TMAZ area, the temperature results is very high much like in Fig. 62(b) and Fig. 47. Finally, in the case of Model I, the temperature results are similarly low as in Fig. 61(c) and Fig. 46. Thus, the appropriate determination of the rotation boundary region is important in the FSW heat transfer analysis.

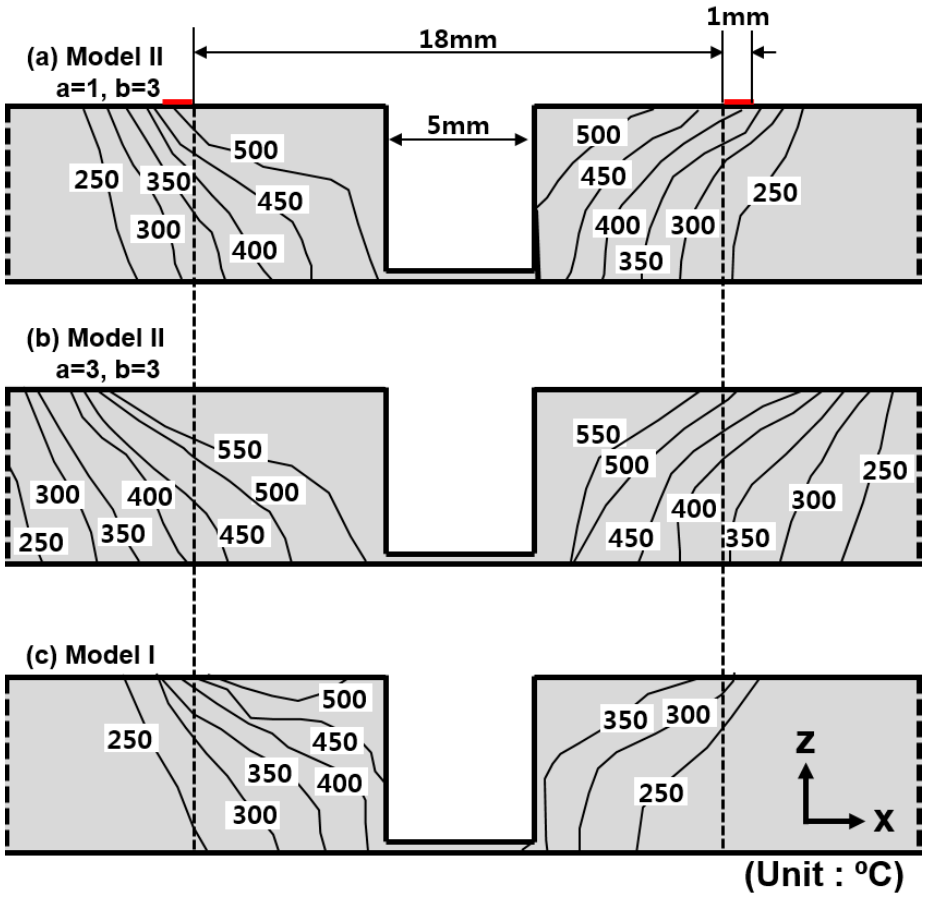

Fig. 62. The cross sectional temperature distribution of Exp. #1.

5.3. Summary of heat transfer analysis

In this study, heat transfer analysis is carried out using the CFD commercial program 'Fluent'. In order to simulate the flow effect of the rotating tool, two methods were compared. In addition, the RAZ concept of rotating and generating a heat source is adopted. The heat transfer analysis is carried out using a parametric study of the RAZ size. The simulated

temperature distribution results are compared with experimental and reference results. Consequently, when the value of 'a' is 1 mm and the value of 'b' is 2 – 3 mm in RAZ, the temperature results correspond in agreement with the experimental results and reference results. On the contrary, when rotating a contact surface, the temperature results are lower than the experimental and reference results. As previously stated, the results are verified by the cross sectional macrostructure of Exp. #1 – 2 and simulation results of the cross sectional velocity and temperature. The results of this study suggest that between the methods of Model I and Model II, Model II is more suitable. In the case of Model II, because the temperature is affected greatly by the RAZ area size it is important to figure out the appropriate RAZ area size for the thermal analysis of FSW. It is found that the analysis results shows the best agreement with the experiment results when the size of RAZ is assumed to be similar to TMAZ, that is, the size of RAZ is 1 mm larger than the radius of the tool shoulder and 2 – 3 mm larger than the radius of the tool pin.

6. Comparison with experimental and simulation residual stress results

When certain mechanisms, including plastic deformations and temperature gradients, occur and release in a structure, stresses remain, due to the shape of the structure, and external constraints. These stresses are referred to as residual stress. In the welding process, base material expands locally in a heating process. When the welding is finished, and cools to room temperature, the residual stresses are left at almost yield strength level. In the case of FSW, the maximum temperature is 80 – 90% of the melting point of the materials. Thus, the residual stresses are smaller than for other fusion welding, and have mostly not been considered before. However, the research carried out in last one decade has revealed that the residual stress in FS welded work piece can be significant. Table 17 summarizes the residual stresses at the weld centerline for various aluminum alloys using previous literatures [43].

Table 17. Summary of residual stress magnitude and other information [43]

Material	Yield stress (MPa) (A)	Max. tensile residual stress (MPa) (B)	Ratio of (B/A) x 100	Rotation speed (RPM)	Welding speed (mm/min)	Thick ness	Measurement technique
2219-T62	390	170	43.6	300	60	12	Hole drilling strain gage method
		130	33.3	400	60	12	
		120	30.8	500	60	12	
		150	38.5	400	100	12	
		135	34.6	400	80	12	
2024-T4	325	65	20.0	750	150	5	Neutron diffraction
		90	27.7	750	475	5	
2024-T3	345	140	40.6	1500	100	1.6	Slot sectioning stress relaxation method
2199-T8E74	400	150	37.5	800	200	5	Synchrotron diffraction
		170	42.5	800	300	5	
		210	52.5	800	400	5	
2195-T8	580	120	20.7	-	-	12.7	Neutron diffraction
2024-T3	345	185	53.6	800	200	5	Neutron and synchrotron diffraction
2199-T8	400	220	55.0	800	400	5	Neutron and synchrotron diffraction
2024-T351	470	56	11.9	750	71.5	3	Cut-compliance technique
2195	**215**	**150**	**69.8**	**300**	**150**	**12.5**	**X-ray diffraction**
2050-T851	500	130	26.0	380	200	15	Cut-compliance technique
2024-	324	165	50.9	-	-	-	Hole drilling

T4							strain gage method
2024-T3	322	125	38.8	576	198	3.2	Synchrotron diffraction
		185	57.5	348	198	3.2	
2024-T351	318	135	42.5	348	96	6.3	
2024-T3	**322**	**287**	**89.1**	**550**	**350**	**2.5**	**X-ray diffraction**
5083-H19	392	60	15.3	-	200	3	Synchrotron diffraction
5083-H321	228	30	13.2	500	80	8	Synchrotron diffraction
5083-H321	228	100	43.9	348	185	6	Synchrotron diffraction
5083-H321	**228**	**155**	**68.0**	**600**	**160**	**3.5**	**Slot sectioning stress relaxation method**
6061-T6	**276**	140	50.7	1250	279	6	**Neutron diffraction**
		200	**72.5**	**1250**	**787**	**6**	
6082-T6	**250**	**150**	**60.0**	**560**	**300**	**3**	**Synchrotron diffraction**
6061-T6	**276**	**235**	**85.1**	**1250**	**787**	**6.35**	**Neutron diffraction**
6013-T4	**203**	**200**	**98.5**	**1500**	**1000**	**1.8**	**X-ray diffraction**
7075-T6	510	92	18.0	715	100	-	Cut-compliance technique
7075-T6	510	225	44.1	280	300	2	X-ray diffraction
7108-T79	400	200	50.0	-	600	-	Ultrasonic wave technique
7050-T7541	469	195	41.6	540	408	6.4	Cut-compliance technique
7749	583	230	39.5	225	250	12.1	Synchrotron diffraction

Most of FSW residual stress researches are focused on aluminum alloys 2XXX, 5XXX, 6XXX, and 7XXX. The reason is related to their extensive use in vehicles such as vessel, aircraft, railcar and automobile. In Table 17, sometimes FSW residual stresses are measured at about 60% or above (Bold in Table 17). Especially, the residual stresses of aluminum alloys 6XXX have a lager ratio of yield stress and maximum tensile residual stress. This residual stress significantly affects fatigue behavior and lifetime like fusion welding residual stress [43 – 45]. Therefore, the residual stress distributions of AA6061–T6 in various welding conditions and shapes of FSW are studied and discussed. In addition, asymmetric feature are considered of temperature distribution and residual stress in this study.

Accordingly, FSW residual stress distribution research has been widely studied. M. Peel et al. [46] investigated the results of microstructural and mechanical properties, and the residual stress of AA5083 FSWs, produced under varying conditions. X. K. Zhu et al. [47] measured residual stress using the neutron diffraction technique, and compared this with the calculated residual stress results of 304L stainless steel. Z. Feng et al. [48] integrated thermal, metallurgical, and mechanical models for the residual stress field, and the softening of AA6061−T6, by using ANSYS. The model predictions were confirmed by experimental temperature, micro hardness, and residual stress data. W. Woo et al. [49] experimented with FSW with two

different tools: a typical tool that includes a pin, and a pinless tool. A high temperature gradient in the thickness direction was observed, using the pinless tool. This is why the differences between the top surface and bottom surface temperatures are higher than for a typical tool. Therefore, the difference of residual stresses is much larger, than when using a typical tool. Also, the angular distortion is large in a pinless tool. V. Dattoma et al. [50] investigated the influence of shoulder geometry on heat generation during FSW. Furthermore, dissimilar (AA6082-T6 and AA20204-T3) FSW experiments were carried out, and measured residual stress. G. Buffa et al. [51] carried out thermo-mechanical rigid viscoplastic simulation using DEFORM, and elasto-plastic simulation, using ABAQUS software. The DEFORM data were manually transferred to a further elasto-plastic finite element (FE) model, using a brick type mesh in the ABAQUS environment. R. Mohammad et al. [52] performed a three-dimensional numerical simulation of FSW, concerning the tool moving speed, in relation to heat distribution and residual stress. L. Z. Jin et al. [53] experimented with an orbital FSW of copper canisters. Heat transfer and elasto-plastic analysis were carried out, using COMSOL Multiphysics version 3.5a. Experimental residual stresses by using an X-ray diffraction (XRD) result were compared with the calculated result. S. Sadeghi et al. [54] calculated residual stress by the same method as G. Buffa et al.

[51], and measured residual stress by using an ultrasonic wave. Measured residual stress using the ultrasonic wave method was well matched with hole-drilling measurement and simulation results.

However, residual stress analysis research is not sufficient for FSW, such as temperature and residual stress distribution. In this study, CFD program, Fluent is used to calculate the asymmetric temperature distribution. Heat-flow analysis is carried out, using Fluent. The temperature data coming from the Fluent simulation are transferred to further elasto-plastic analysis in the ANSYS multi physics environment. The calculated residual stresses are compared with experimental residual stresses. After finishing the FSW, the residual stress is measured at Mokpo National University, by using XRD methods. The XRD equipment is the XSTRESS3000 model, made by STRESSTECH Company, as shown in Fig. 63. The residual stress is measured at the AS and the RS, for an investigation of the asymmetric effect of the FSW. The measured points of residual stresses are located at 0 – 20 mm at 1mm intervals, 20 – 50 mm at 5 mm intervals, and 50 – 100 mm at 10 mm intervals as shown in Fig. 40. Also, the residual stress is measured in the longitudinal and the lateral directions of the weld. At this time, butt FSW and T lap joint shape II FSW are considered.

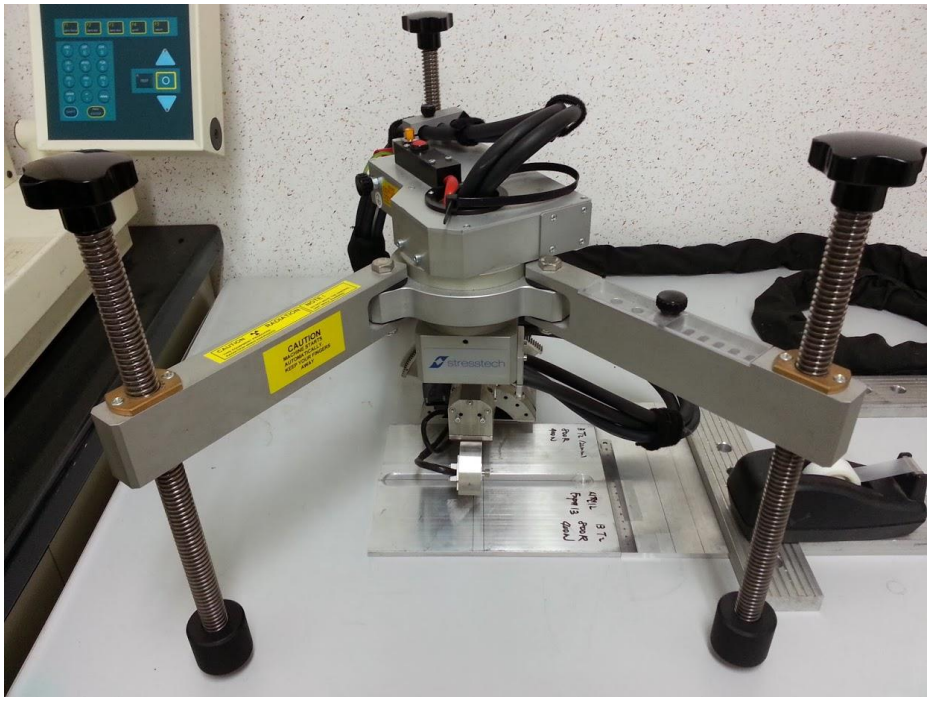

Fig. 63. The XRD equipment for measuring residual stress.

6.1. Welding dimension and parameters for residual stress analysis

In this section, three butt FSW and a T lap joint shape II residual stress analysis results are compared with the experimental results. The description of residual stress analysis models are summarized in Table 18.

Table 18. Residual stress analysis model for comparison.

Designation	Weld shape	Tool	Rotation speed (RPM)	Welding speed (mm/min)	Plunge depth (mm)
Exp. #3	Butt	T2	600	400	0.1
Exp. #4	Butt	T2	800	500	0.1
Exp. #5	Butt	T2	800	400	0.1
Exp. #6	T lap joint	T3	1000	300	0.1
Exp. #7	T lap joint	T3	1000	600	0.1

6.2. Temperature data of CFD analysis mapping to the FE model

First, the temperature distribution and history are compared with the experimental results of Exp. #3 – 7. The temperature distribution, in accordance with the time history that is the result of the heat transfer analysis, can be utilized for the structural analysis. Thus, accurate heat transfer analysis is the most important step for calculating the residual stress distribution. The calculated temperature distribution results are compared with the experimental results, and displayed in Fig. 64.

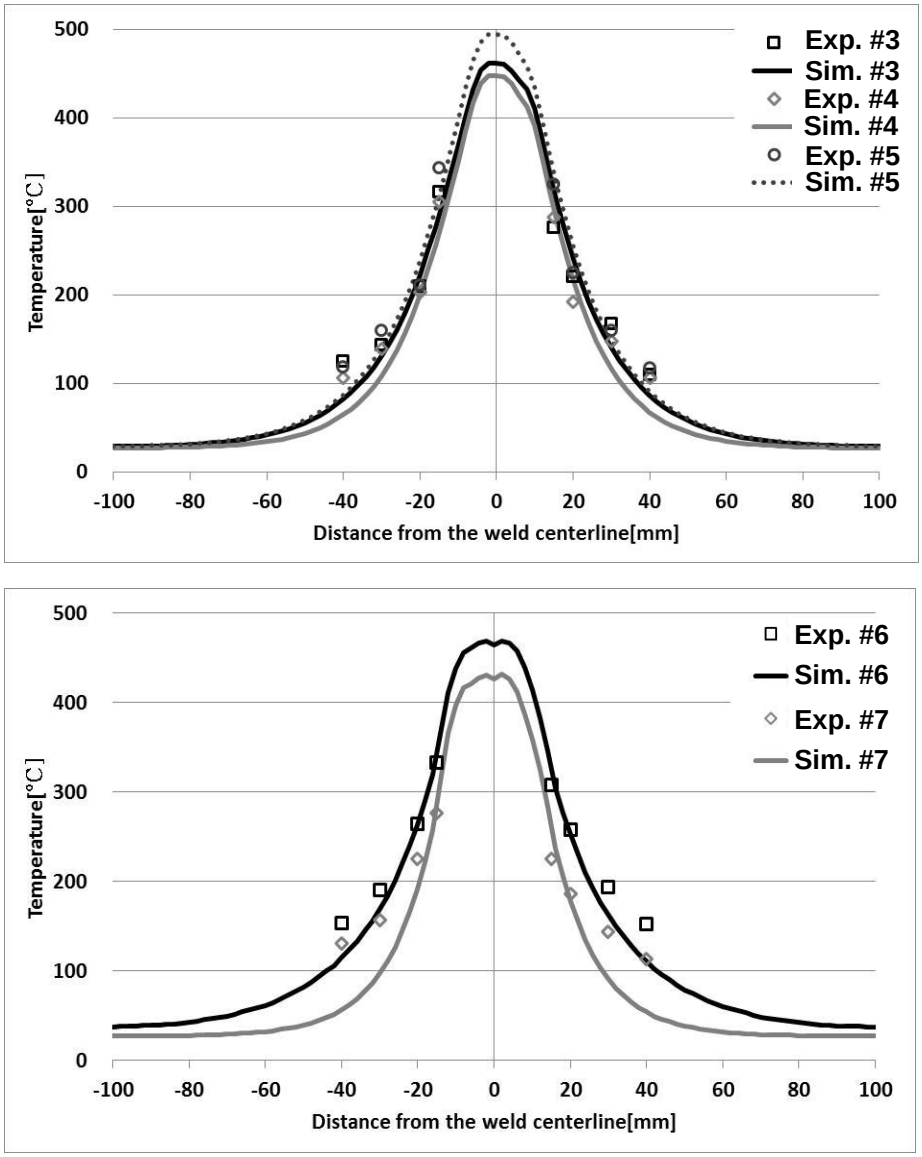

Fig. 64. Temperature distribution of experimental and simulation results of Exp. #3 – 7.

The temperature distribution results in Fig. 64 confirm that the experiments and simulations show fairly good agreement. Steady state heat transfer analysis is carried out in Eulerian description, and then the results are transferred to the FE model, for elasto-plastic analysis. Transient heat transfer

analysis is performed in the FE model, and the temperature is assumed as quasi-steady state during the welding process. At this time, the steady state heat transfer analysis and transient heat transfer analysis are implemented by using Fluent (Eulerian description), and ANSYS multi physics (Lagransian description), respectively. However, the shapes of the mesh differ from each other, as shown in Fig. 65. Thus, the temperature data are extracted at 1 mm interval, and transferred to the FE model nodes.

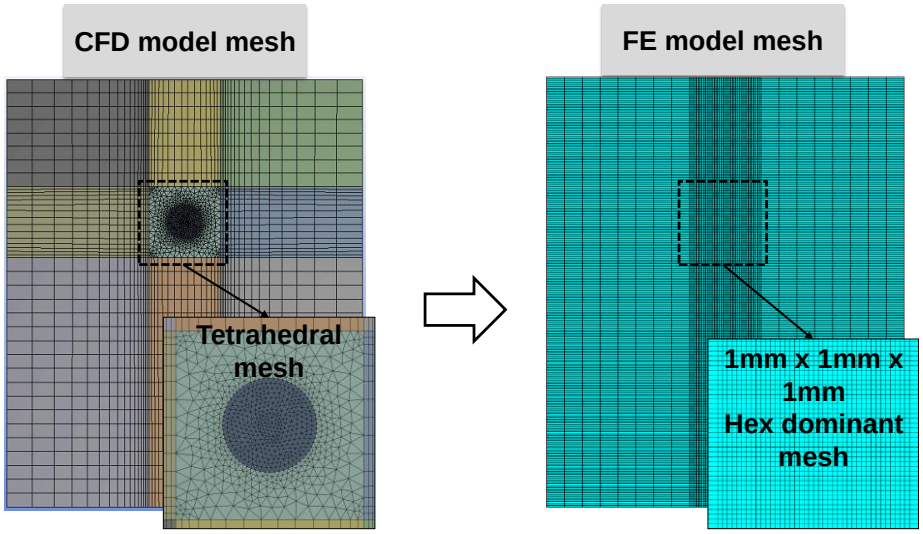

Fig. 65. Heat flow model using the Fluent (Left), and elasto-plastic model using the ANSYS Multi physics (Right).

For the rational temperature data mapping, various parametric studies are carried out for the Exp. #5 model. First, the temperature data are inputted in a square area along the thickness direction, at 1 mm interval. The square lengths are 24

(Rect. 24), 40 (Rect. 40), and 100 mm (Rect. 100). Also, a circular area is considered, of 24 mm (Cir. 24) diameter. In addition, transient heat transfer analysis is performed without the tool region temperature, to know the effect of the tool temperature for Rect. 40 and 100. The temperature spreads out in the work piece, during the transient heat transfer analysis.

Thermal residual stresses occur, due to the operational temperature fields. The thermal strain is expressed in Eq. (17):

$$\varepsilon_{th} = \alpha \times \Delta T \tag{17}$$

where, ε_{th} is the thermal strain, α is the thermal expansion coefficient, and T is the temperature. Thermal strain is a function of the thermal expansion coefficient and temperature gradient. The temperature history is an important factor that affects the residual stress value and distribution. Thus, the temperature history of the simulation is compared with the experimental result. The temperature histories of two points provide comparison target points. The points are located 15 mm from the weld centerline, and denoted as TC-A1 and TC-R1 in Fig. 40. Temperature distributions and histories according to the input regions are plotted in Figs. 66 and 67.

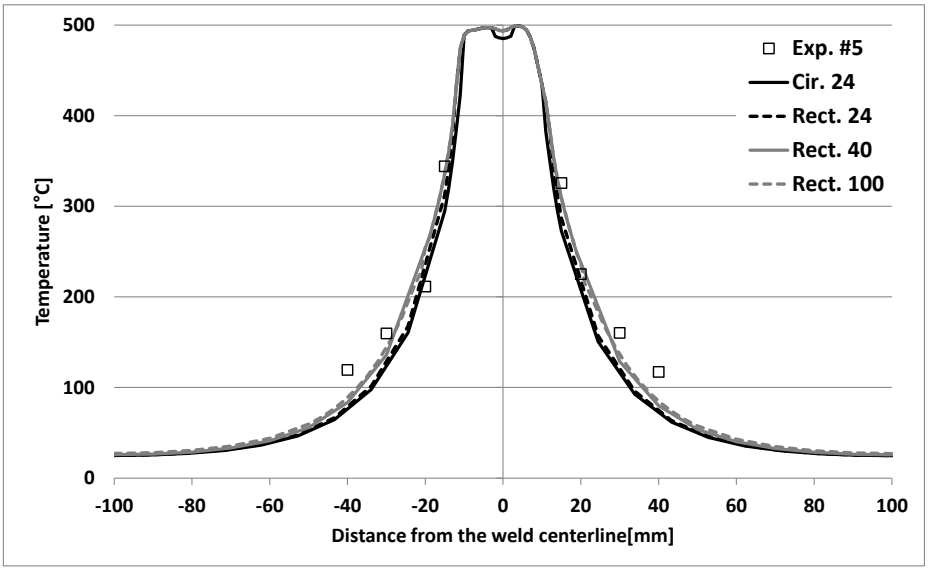

Fig. 66. Temperature distribution of Exp. #5 and simulation results.

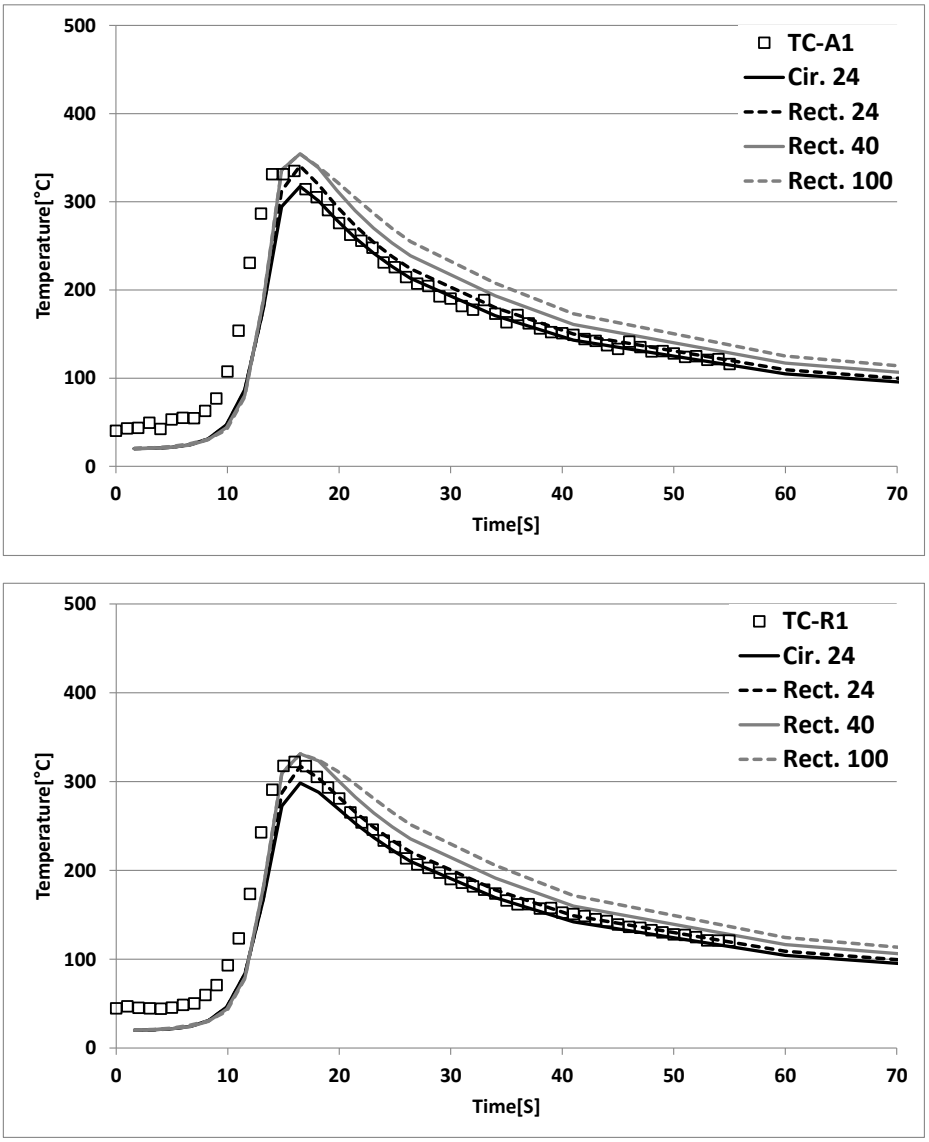

Fig. 67. Temperature history of Exp. #5 and simulation results in AS (Top) and RS (Bottom).

In Fig. 66, the temperature distribution is higher along the perpendicular of the weld centerline with the larger input region. The total temperature history of Cir. 24 and Rect. 24 shows good agreement with the experimental results. In the case of Rect. 40 and 100, the temperature histories are excessively

high in the simulation. In the first step of the transient heat transfer analysis in the FE model, immoderate temperature data are inputted, as shown in Fig. 68.

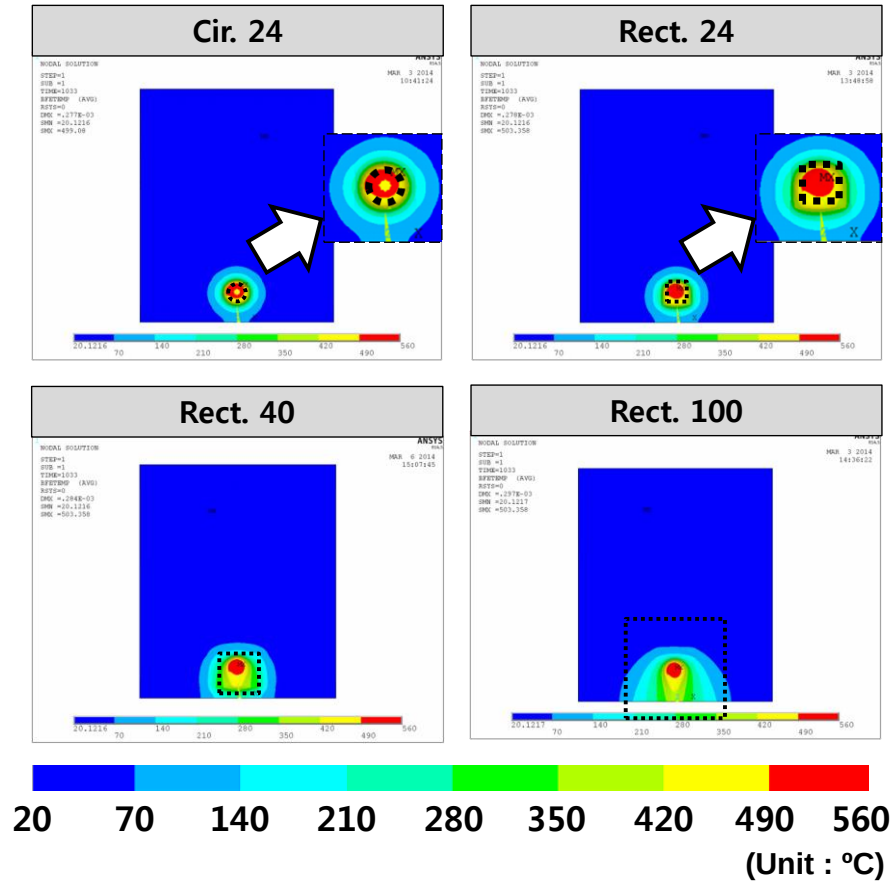

Fig. 68. Temperature distribution at the first heat transfer analysis step.

In practically the primary stage of the FSW, the thermal conduction rises gradually. Thus, the most well matched cases with experimental results are Cir. 24, and Rect. 24.

During the actually FSW process, the tool penetrates the work piece, and traverses along the weld centerline. Accordingly, there is empty space provided by the tool volume.

For this reason, the effect of the tool is studied for Rect. 40 and 100. The temperature distribution and history are compared between the experimental and simulation results in Exp. #5. The results are plotted in Figs. 69 and 70.

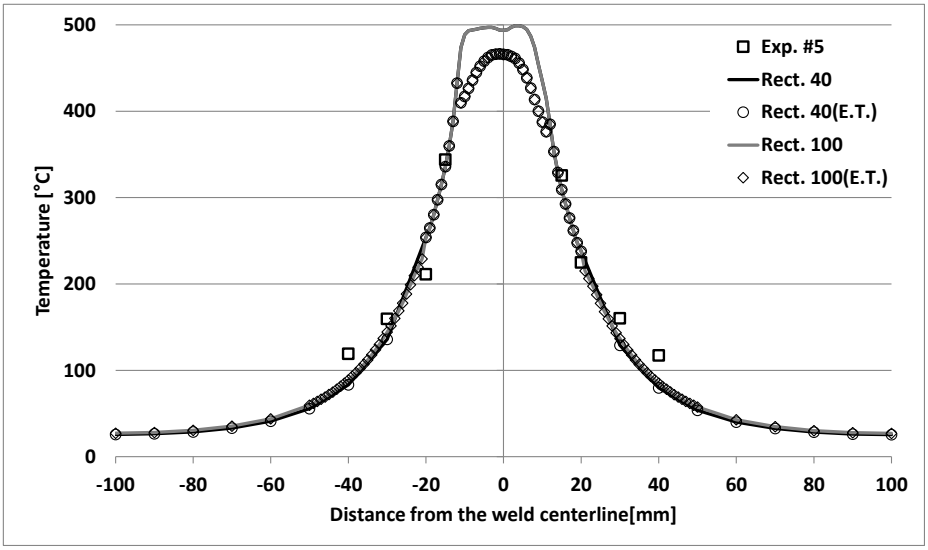

Fig. 69. Temperature distribution of the total region and the region without tool volume (E.T., Empty Tool).

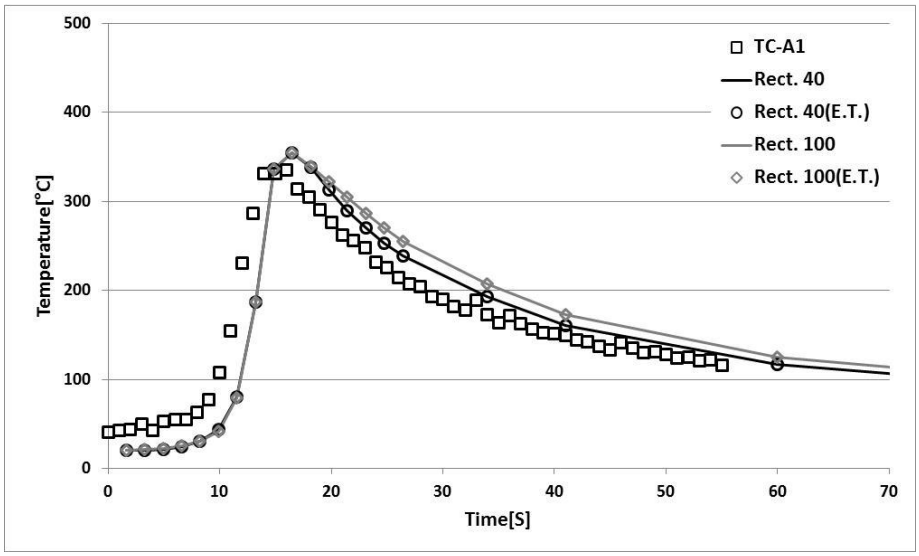

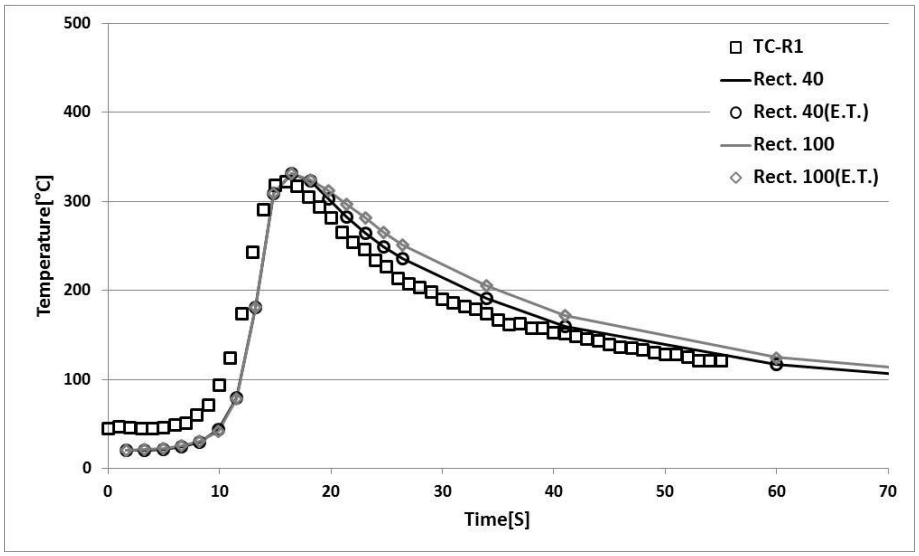

Fig. 70. Temperature history of the total region and the region without tool volume, in AS (Top) and RS (Bottom).

In Fig. 69, the temperature distribution in the vicinity of the center is different, since the temperature is inputted without the tool region (E.T.); and in this case, the temperature is low in the center. However, the temperature of the center is raised, somewhat similar to the input tool region case. In Fig. 70, there

is entirely the same temperature history in TC-A1 and TC-R1. This means whether to input or not input the tool area temperature does not critically affect the heat transfer analysis. Therefore, the case of Cir. 24 is used for the heat transfer analysis for the elasto-plastic analysis in the FE model. Cir. 24 resembles the real heat generation region of the FSW.

6.3. Structural analysis model and results

As mentioned above, residual stresses remain, after welding a structure. These residual stresses effect a reduction in the fatigue and buckling strength, and accelerate stress corrosion cracking. The influence of residual stresses may be identified, and the design should then reflect that influence. Residual stresses occur due to the non-uniform temperature distribution, and these can be simulated by means of thermal elasto-plastic analysis. The material properties are changed by temperature, so residual stress analysis contains a nonlinearity. In this study, heat transfer analysis is carried out, and the temperature data of every step are saved. Elasto-plastic analysis is implemented, using the saved temperature data. This method is referred to as semi-coupled or sequential analysis, and a schematic drawing of the calculation is shown in Fig. 71.

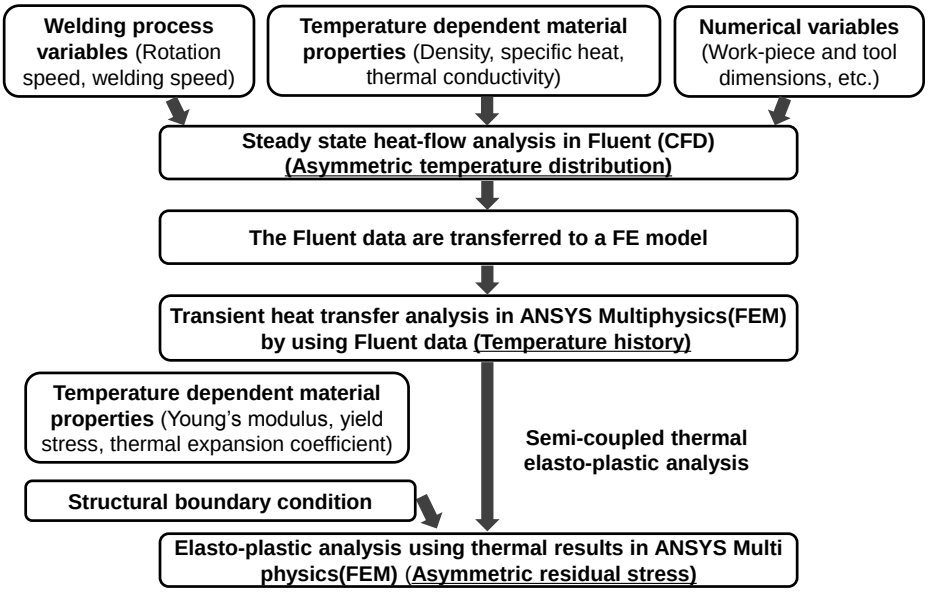

Fig. 71. Calculation flow chart.

The temperature-dependent yield stress, Young's modulus and coefficient of the thermal expansion are used to the structural analysis as shown in Fig. 72 [8].

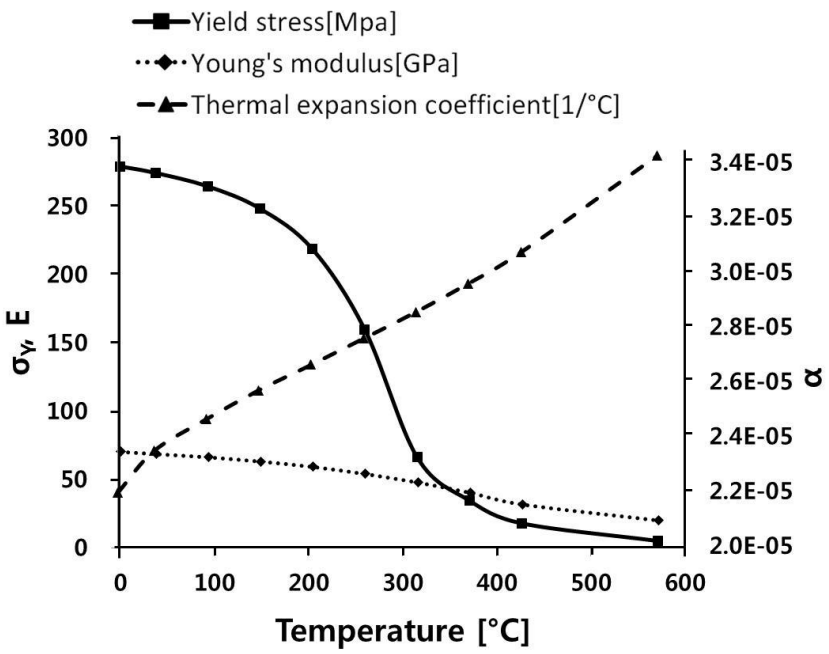

Fig. 72. Temperature dependent material properties for elasto-plastic analysis.

The work piece structural boundary conditions are considered. To simulate the backing plate at the bottom of the work piece, all the bottom nodes of the work piece are constrained in the thickness direction (z-direction). Also, work piece clamps on both sides offer external constraint. The nodes along the long edges in the range of 20 mm are constrained in all degrees of freedom. After the work piece reaches room temperature, all the constrained conditions are released. The final residual stresses are measured along the Line AA in Fig. 40, on the longitudinal (SY) and perpendicular direction of the weld centerline (SX), and compared with the simulation results.

6.4. Residual stress analysis results and discussions

The residual stresses results of Exp. #3 – 7 are depicted in Fig. 73, and all the cases are positively matched in AS and RS. Thus, the proposed a coupled CFD–FEM simulation is good approach to residual stress analysis of FSW.

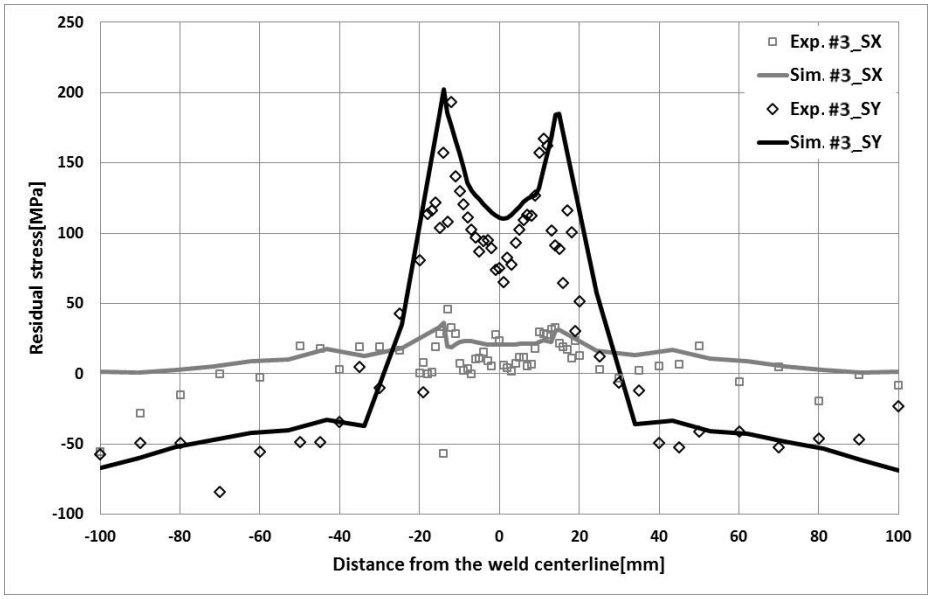

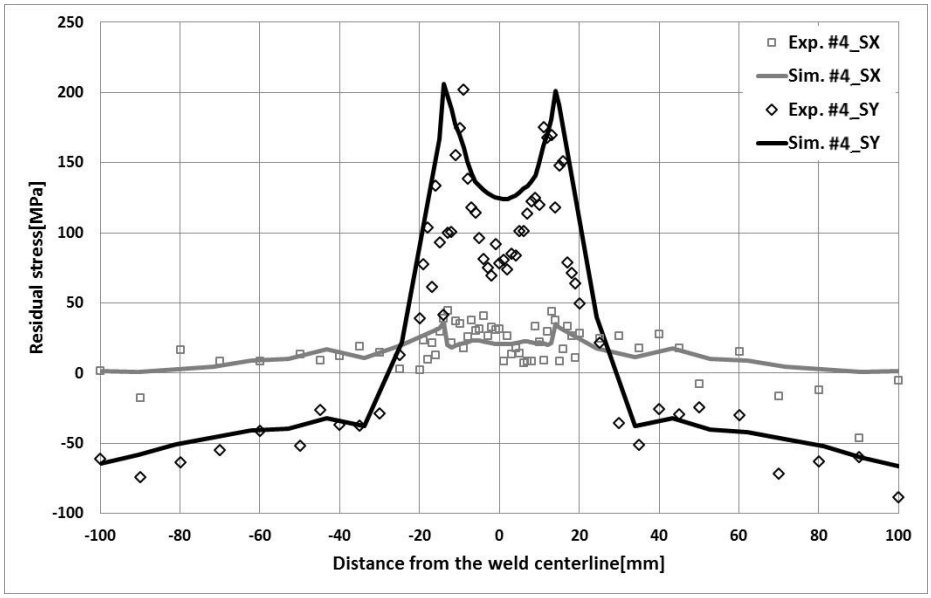
Exp. #4_SX
Sim. #4_SX
Exp. #4_SY
Sim. #4_SY
Residual stress[MPa]
Distance from the weld centerline[mm]
250
200
150
100
50
0
-50
-100
-100
-80
-60
-40
-20
0
20
40
60
80
100

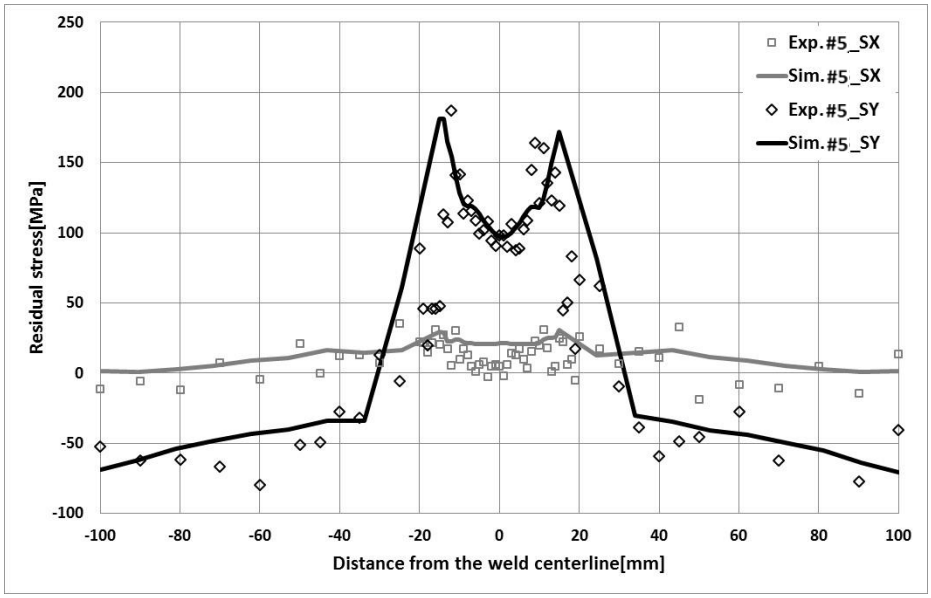
Exp.#5_SX
Sim.#5_SX
Exp.#5_SY
Sim.#5_SY
Residual stress[MPa]
Distance from the weld centerline[mm]
250
200
150
100
50
0
-50
-100
-100
-80
-60
-40
-20
0
20
40
60
80
100

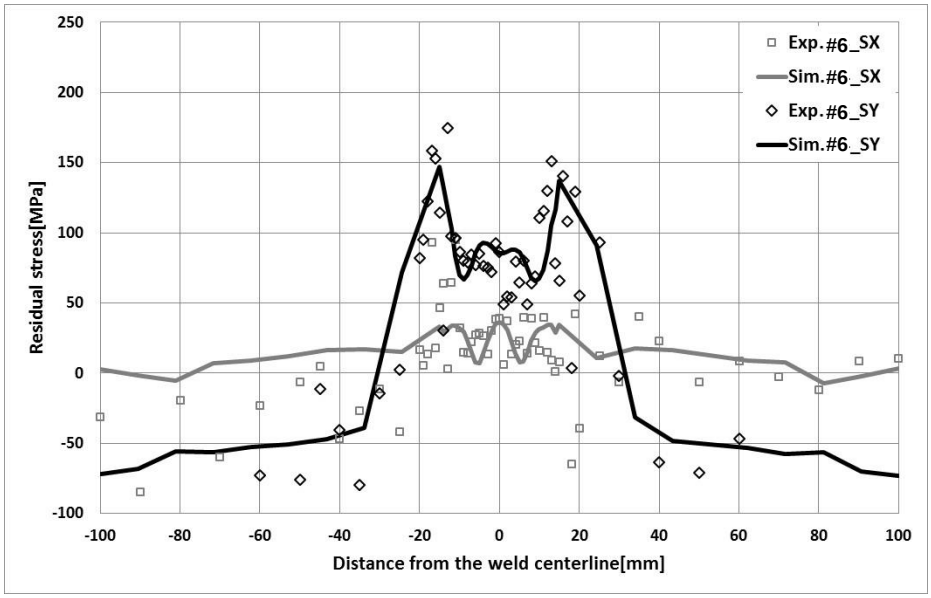

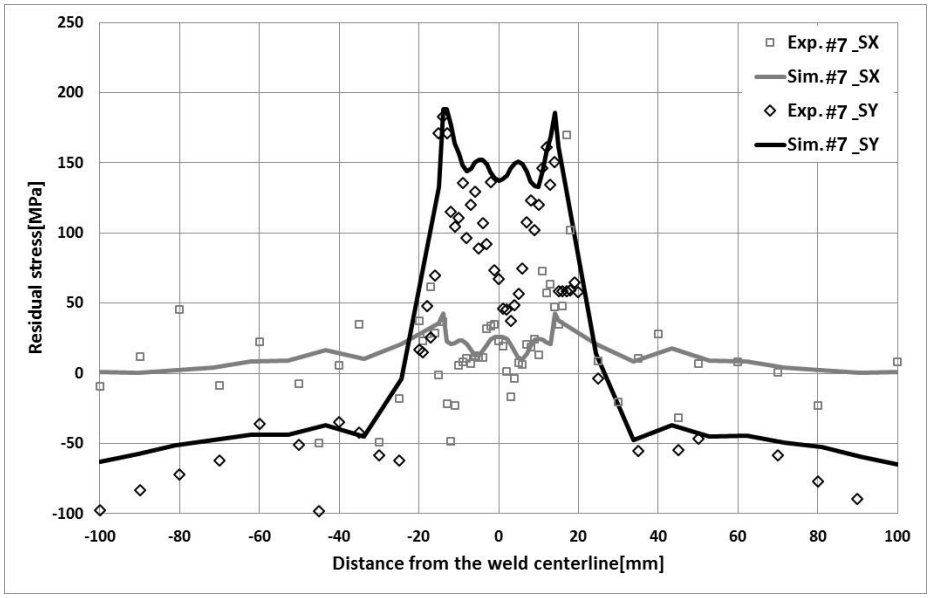

Fig. 73. Residual stresses results of experiment and simulation for Exp. #3 – 7.

For considering the asymmetric effects of FSW, heat transfer analysis is carried out, using the CFD software Fluent. Through this steady state heat transfer analysis, the asymmetric temperature distribution is calculated, and this

temperature data is inputted into the FE model. The temperature is assumed as quasi-steady state during the welding, and nonlinear transient heat transfer analysis is carried out. When the input volume sets a cylinder shape, which has a shoulder diameter (Cir. 24), the temperature distribution and history are well matched with the experimental results. Heat sources are generated between the work piece and the tool, since the preceding analysis is reasonable. Other cases, such as Rect. 40 and 100, have an inordinate temperature result. Asymmetric residual stresses are calculated using the asymmetric temperature data. The maximum tensile residual stress tends to be observed at 2 – 3 mm from the tool shoulder edge. This is probably through the linear velocity of the tool having the fastest value at the edge of the tool shoulder. The HAZ may be located at 2 – 3 mm from the tool shoulder edge, and this region has the largest temperature gradient. This is the reason the residual stress is observed in a similar position for Exp. #3 – 7, using a 24 mm tool shoulder diameter. Moreover, the longitudinal residual stress is larger than the lateral residual stress, because during the welding process, the temperature gradient is changing faster in the longitudinal direction, than other directions.

To find the relationship between the rotation speed of the tool, and the longitudinal residual stresses, Exp. #3 and Exp. #5 are compared in Fig. 74. The lateral residual stresses

scarcely differ. As the rotation speed of the tool increases, the longitudinal residual stress decreases slightly. When the tool has a higher rotation speed, the heat is spread out far away in the perpendicular direction of the weld centerline. The temperature gradient has a slow grade, and enough time to relax the stress. Finally, it has affected the maximum tensile residual stress.

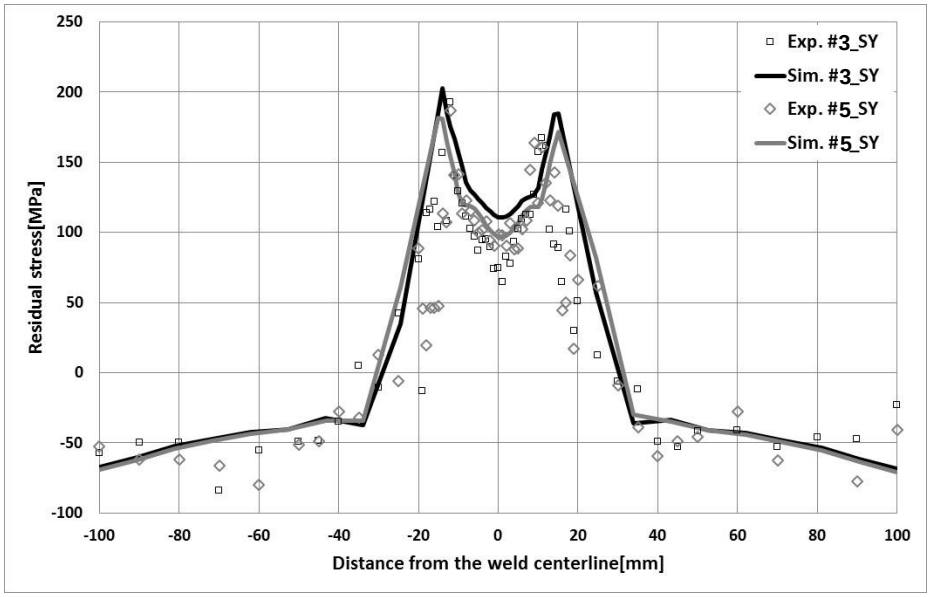

Fig. 74. The residual stress distribution, compared to knowing the effect of the rotation speed.

To confirm the effect of the welding speed on the residual stress, Exp. #4 and Exp. #5 in butt FSW and Exp. #6 and Exp. #7 in T lap joint shape II FSW are conducted. Similarly, only the longitudinal residual stresses are compared in Fig. 75.

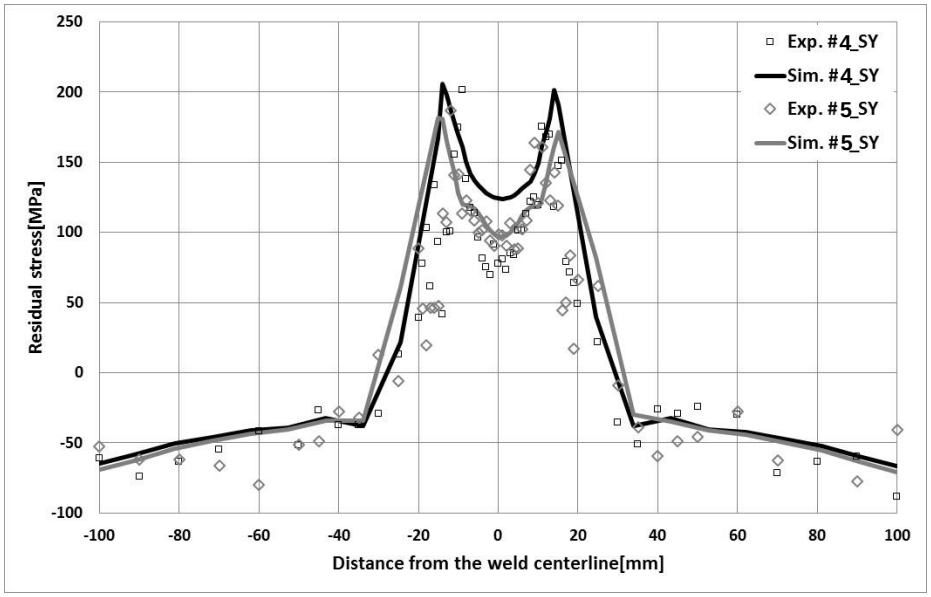

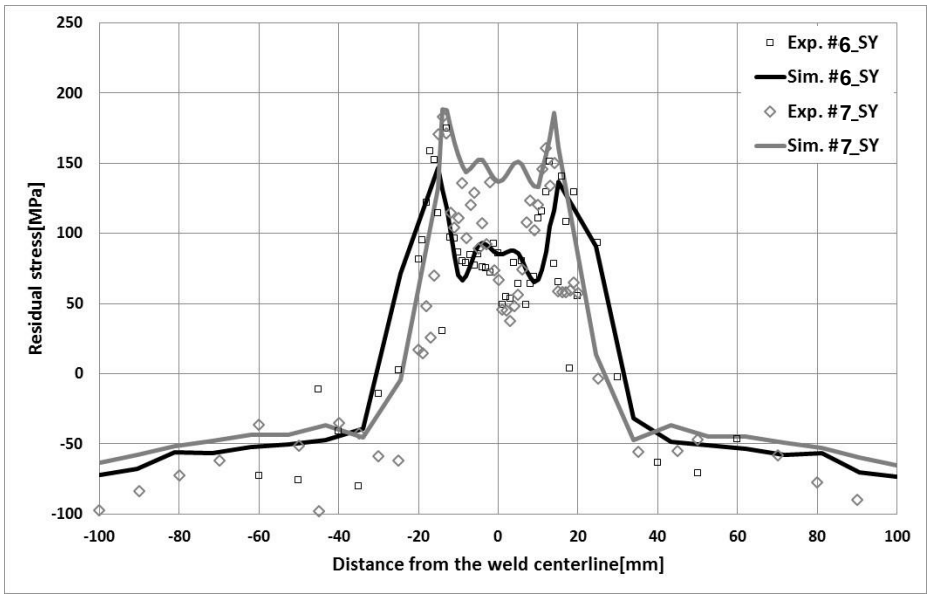

Fig. 75. The residual stress distribution, compared to knowing the effect of the welding speed.

Maximum residual stresses have a large difference from changing the welding speed [45, 48]. In fast welding speed, the temperature gradient has a steep grade, and an insufficient stress relief time. Consequently, the maximum residual stress

is larger for fast welding speed. The maximum tensile residual stress of FSW is known to be small. However, this is limited to a slow welding speed, which leads to a gradual temperature gradient, and adequate stress mitigation time. When the welding speed is fast, the maximum longitudinal tensile residual stress reaches 70% of the yield strength of the AA 6061-T6, and it can be problematic to the fatigue life of the structure. These maximum tensile residual stresses were also confirmed in previous literature [48].

More parametric studies are carried out under varying welding conditions, as shown in Table 19 and then the effects of maximum temperature, maximum residual stress, and width of residual stress are analyzed, by using a coupled CFD-FEM simulation. The work piece and the tool dimension used in the parametric studies are the same as for the butt FSW condition of Exp. #3.

Table 19. Welding conditions for parametric study.

Designation	Rotation speed (RPM)	Welding speed (mm/min)
No. 1	800	100
No. 2	800	200
No. 3	800	400
No. 4	800	500
No. 5	800	600
No. 6	600	400
No. 7	800	400
No. 8	1000	400
No. 9	1200	400
No. 10	1400	400

In Table 19, the cases of No. 1 – 5 will be used to check the effect of the welding speed, and the others are for the rotation speed of the tool. These ranges of welding conditions are generally used in FSW. Thus, the results of parametric studies are comprehensive. If the welding speed is faster than 600 mm/min, or the tool rotation speed is larger than 600 RPM, these conditions only go a little way to stir the work piece. In this respect, they are sensible conditions for analysis of the welding parameters.

The effect of the welding speed and the tool rotation speed at maximum temperature are represented. Fig. 76 shows the temperature distribution at the middle stage of the welding. Also, Fig. 77 denotes the residual stress distribution after cooling, and releasing external constraint. At a low welding speed, the maximum temperature is high, and the temperature distribution has a wide range along the perpendicular of the weld centerline. At a higher tool rotation speed, on the other hand, little difference exists in the maximum temperature and the temperature distribution, as in Fig. 76.

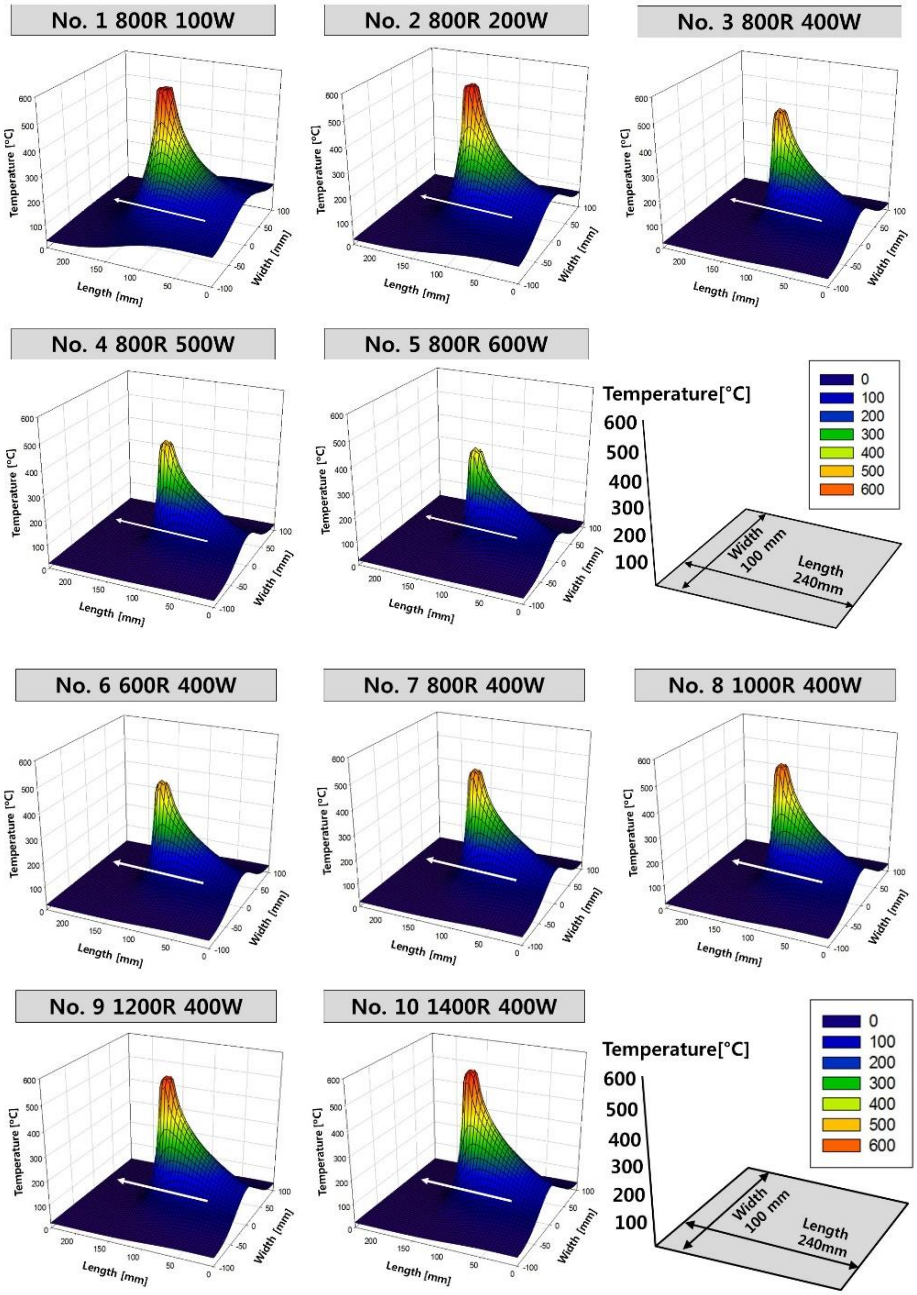

Fig. 76. 3D temperature distribution at the middle stage of the welding.

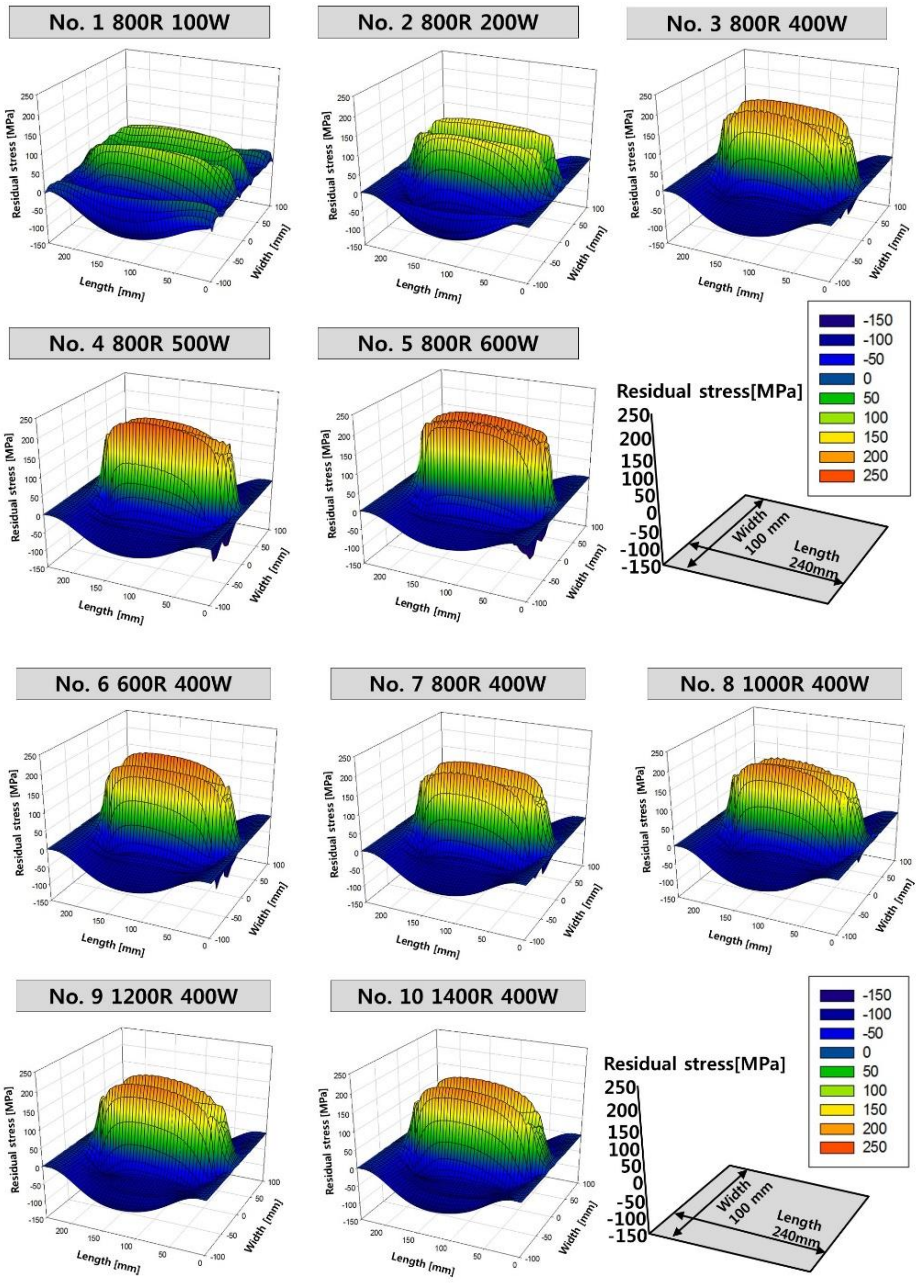

Fig. 77. 3D longitudinal residual stress distribution after the cooling.

In Fig. 77, the maximum tensile residual stress and distribution have the same result as Fig. 75, for various welding speeds. In the varied rotation speed, the maximum and the width of the tensile residual stress have little difference, like

the temperature distribution during welding.

As before, the residual stresses are compared with No. 1 – 10 at Line AA in Fig. 78.

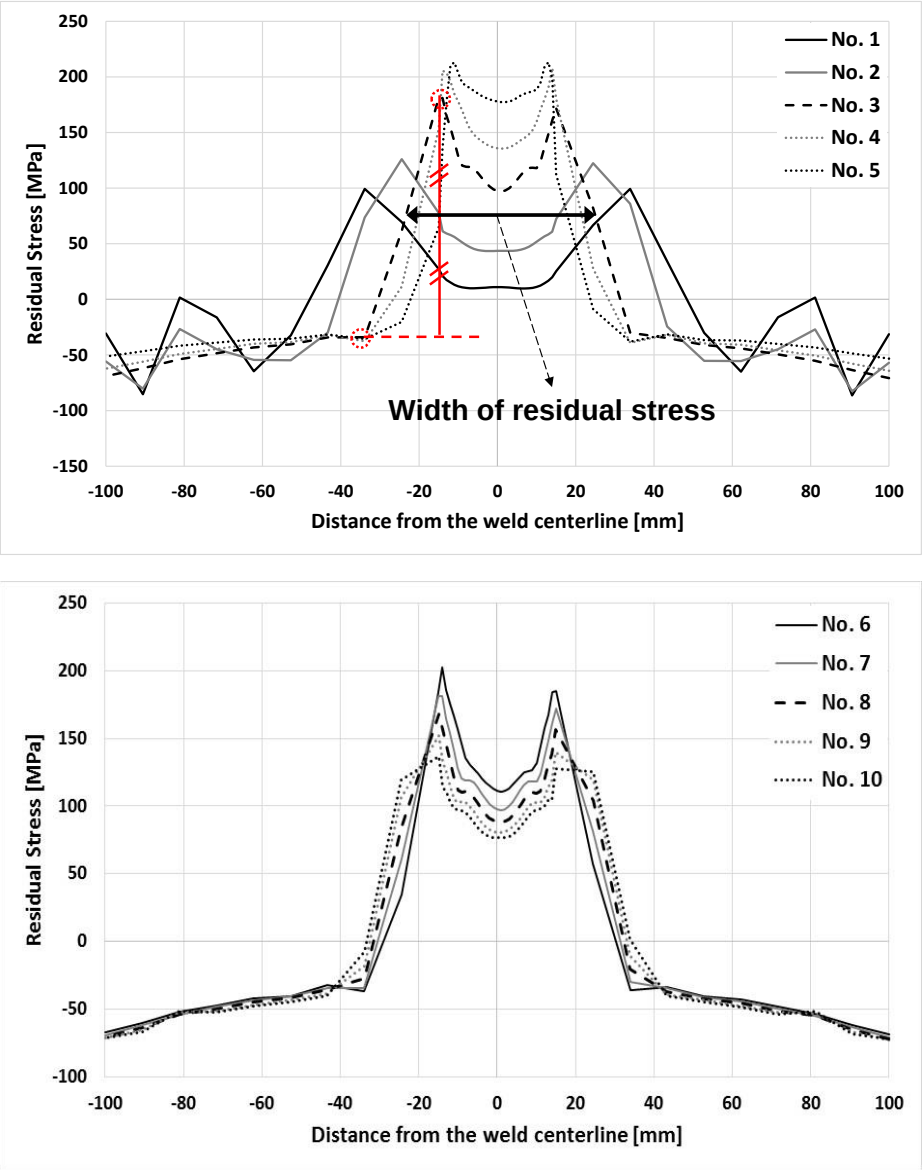

Fig. 78. The longitudinal residual stress distribution at 'Line AA'.

In Fig. 78, the results of the maximum longitudinal residual stresses are shown more clearly. Furthermore, the width of tensile residual stress is sensitive to the welding speed (No.1 – 5). The width of tensile residual stress is used as the indicator of the criteria where it is defined as an average of the saddle point value right before the maximum and the maximum residual stress at AS. Therefore a line which has the average value can be drawn from AS to RS, as in Fig. 78 (for No. 3 case is shown).

The effects of welding parameters on the maximum temperature, maximum tensile residual stress, and the width of the tensile residual stress are analyzed. The results of the parametric studies are depicted in Fig. 79 and Table 20.

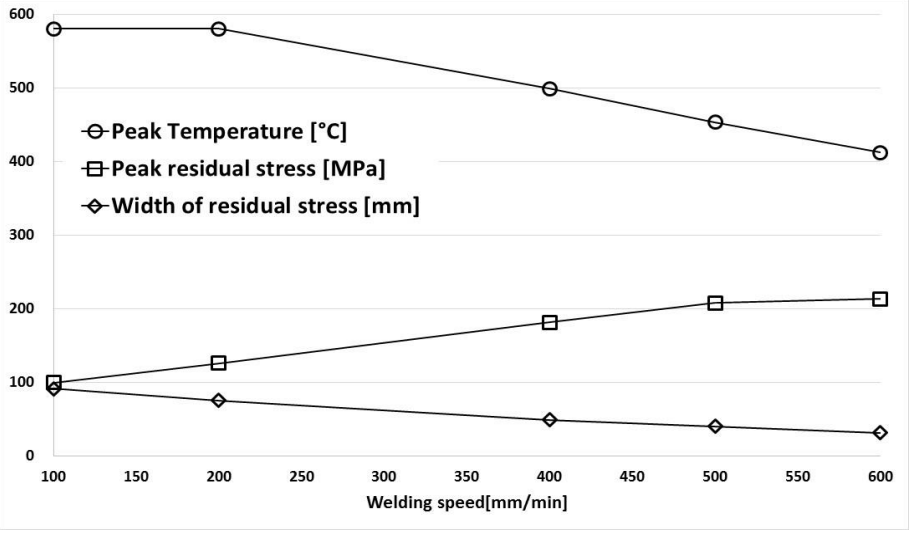

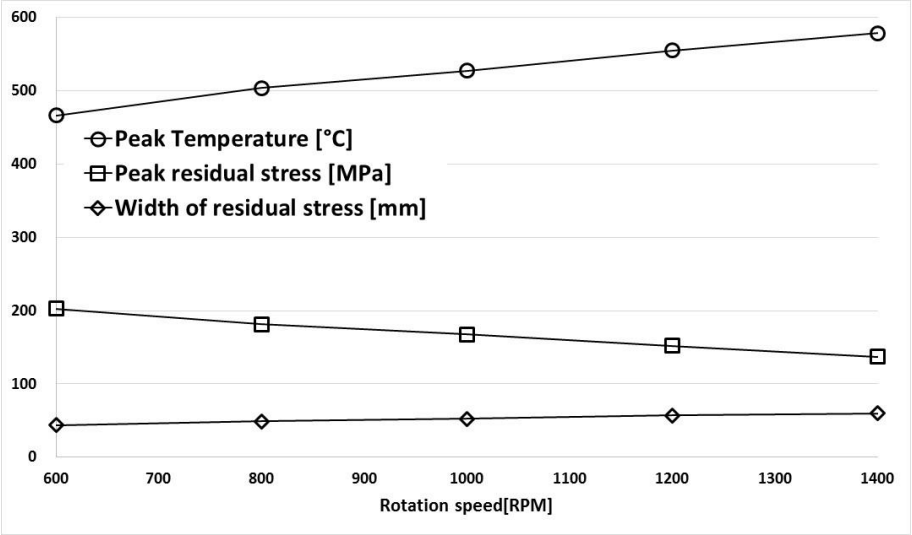

Fig. 79. Summary of the parametric study results with variable welding speed (top) and rotation speed (bottom).

Table 20. Summary of the parametric study results.

Designation	Maximum temperature (℃)	Maximum residual stress (MPa)	Width of residual stress (mm)
No. 1	580.17	99.38	91.27
No. 2	580.01	126.02	75.51
No. 3	503.93	181.35	48.98
No. 4	453.20	207.80	40.59
No. 5	411.92	213.21	31.44
No. 6	466.52	202.54	43.56
No. 7	503.93	181.35	48.98
No. 8	527.54	167.73	52.37
No. 9	554.91	151.76	57.03
No. 10	578.62	136.94	59.75

In Fig. 79, the maximum temperature has a strong relationship with the welding speed and the tool rotation speed. The maximum and width of the tensile residual stress have a distinct welding speed; while there is a weak correlation with

the tool rotation speed. When the welding speed is low, the heat spreads out in a large region. This means that HAZ is large, and the width of the residual stress is also widely formed. Therefore, the width of the residual stress is spread over a wide range of the work piece in No. 1. In this case, the temperature gradient is gentle close to the region, and this shows up as the result of the residual stress leading to a low value.

6.5. Summary of residual stress analysis

In this a coupled CFD-FEM simulation, the steady state temperature distribution data are properly transferred to the FE model, and elasto-plastic analysis is carried out. An 'M' shaped temperature distribution appears during the FSW, and the temperature of AS is greater than of RS. The calculated asymmetrical residual stress is compared to that from the analysis of the experimental results, and verifies the simulation method. The following conclusions may be drawn:

- ✓ The maximum tensile longitudinal residual stress is shown to be about 70% of the yield strength of the AA 6061-T6. This value is not negligible.
- ✓ The transversal residual stress has little value.
- ✓ The longitudinal residual stress is distributed as an 'M' shaped temperature distribution.

- ✓ The maximum tensile residual stress is observed at 2 – 3 mm from the tool shoulder edge in Exp. #3 – 7. This is the boundary between the HAZ and the base material, the point at which the temperature gradient is rapidly changing.
- ✓ The longitudinal residual stress is proportional to the welding speed; whereas, the tool rotation speed has no significant impact on the longitudinal residual stress.
- ✓ At slow welding speed, the 'M' shape of the longitudinal residual stress is more widely distributed. When the welding speed is slow, there is a more spacious area of HAZ. Thus, the distribution of the tensile residual stress distribution is more widely spread.
- ✓ The longitudinal residual stress value is approximately 10% higher in the AS.

7. Welding analysis based on equivalent strain method to cover external constraint during friction stir welding

To predict and control of welding deformation and residual stress, thermal elasto-plastic analysis method is used widely. The best advantage of this method, the solution would be accurate. However, it has a huge computational time as increasing number of element. Because this methods solve a non-linear analysis.

In order to overcome a huge computational time, a several simplified assessment methods such as equivalent load method and equivalent strain method based on inherent strain are researched since 1980's. A detailed history of simplified assessment methods are explained in a previous literature [55].

Most recently, Kim [55] developed an improved equivalent strain method to cover external constraint during cooling stage. FSW has a strong relationship with external constraint. However, Kim method is not matched in FSW, it cannot reflect a feature of FSW. Thus, in this section, improved equivalent strain method will be modified for FSW. The basic governing equations are referred in a previous literature [55]. The whole calculation flow chart of inherent strain method to cover external constraint during FSW is shown in Fig. 80.

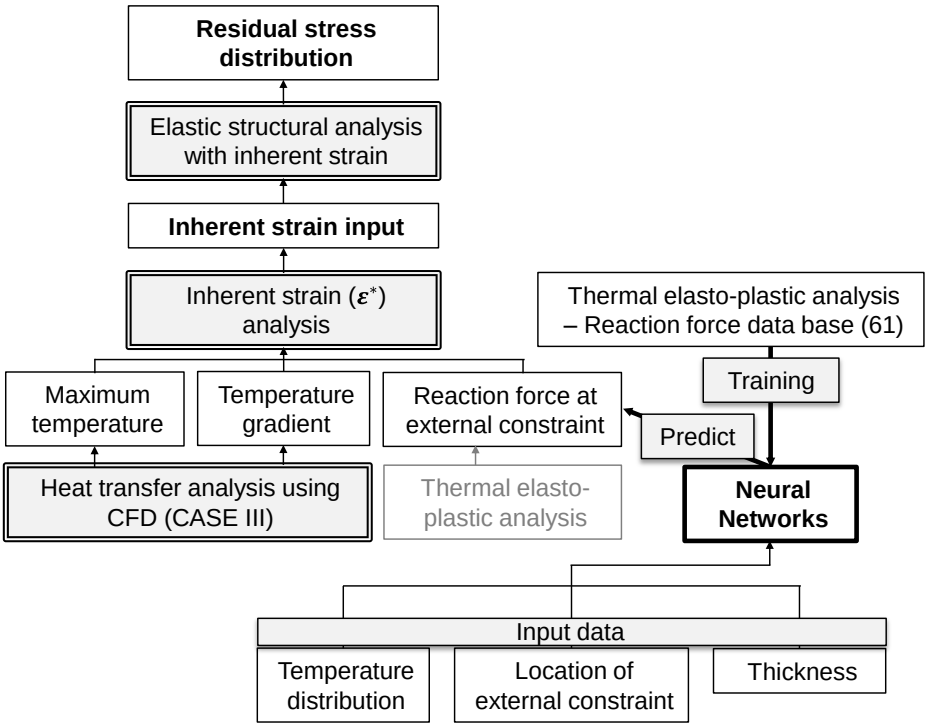

Fig. 80. Calculation flow chart of inherent strain method to cover external constraint during FSW.

In Fig. 80, reaction force is originally calculated by using thermal elasto-plastic analysis and reaction force is different in heating and cooling stage. Thus, several assumption and prediction method is used to find a reaction force. Finally, inherent strain chart is calculated in various conditions. This inherent strain value is used to calculate a residual stress distribution. A detailed calculation flow chart of inherent strain method will be explained sequentially.

7.1. Definition of inherent strain

During the welding process, total strain is divided 4 strains as shown in Fig. 81.

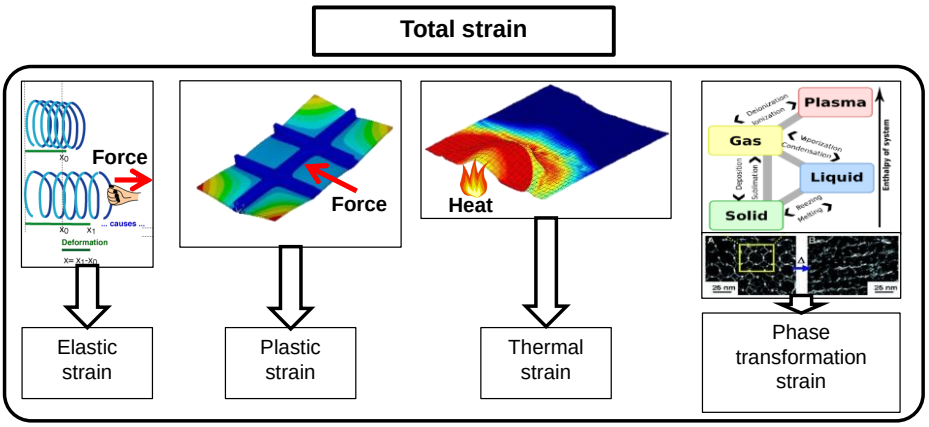

Fig. 81. Total strain is divided 4 strains.

$$\varepsilon = \varepsilon_e + \varepsilon_p + \varepsilon_{th} + \varepsilon_{pt}$$

$$\varepsilon^* = \varepsilon - \varepsilon_e = \varepsilon_p + \varepsilon_{th} + \varepsilon_{pt}$$

where, ε is total strain, ε_e is elastic strain, ε_p is plastic strain, ε_{th} is thermal strain, ε_{pt} is phase transformation strain, and ε^* is inherent strain. Thus, inherent strain is defined difference between total strain and elastic strain.

Inherent strain value is affected several factors such as maximum temperature, temperature gradient of three direction, restraint, external constraint. Kim [56] considered maximum temperature, and restraint to calculate an inherent strain. However, Kim [55] suggested that maximum temperature, temperature gradient in three direction, and external constraint

are most important factors to calculate an inherent strain. Restraint has a little effect, whereas temperature gradient in three direction, and external constrain have a large effect on inherent strain.

In this study, maximum temperature, temperature gradient in three direction, and external constraint are considered to calculate an inherent strain. However, several details are revised in accordance with FSW features.

7.2. Inherent strain method to consider friction stir welding features

For calculate an inherent strain, heat-flow heat transfer analysis result in needed as shown in Fig. 80. After heat transfer analysis, maximum temperature and temperature gradient are calculated. In this research, the temperature gradient is represented by an index named TG and there are three temperature gradient such as TG_x, TG_y, and TG_z. Where x, y, and z mean the temperature gradient of each direction. TG is a value which is greater than 0 and less than or equal to 1. For example, if there is no temperature gradient, then TG=1. The temperature gradient is in inverse proportion to TG value [55]. Like Kim, TG_y is assumed as 1. Because the temperature gradient of welding direction (TG_y) will be almost zero and it means that TG_y value is 1. In addition, the temperature gradient of plate thickness direction (TG_z) is also almost 1 in FSW. Fig.

82 shows the sectional temperature distribution of FSW.

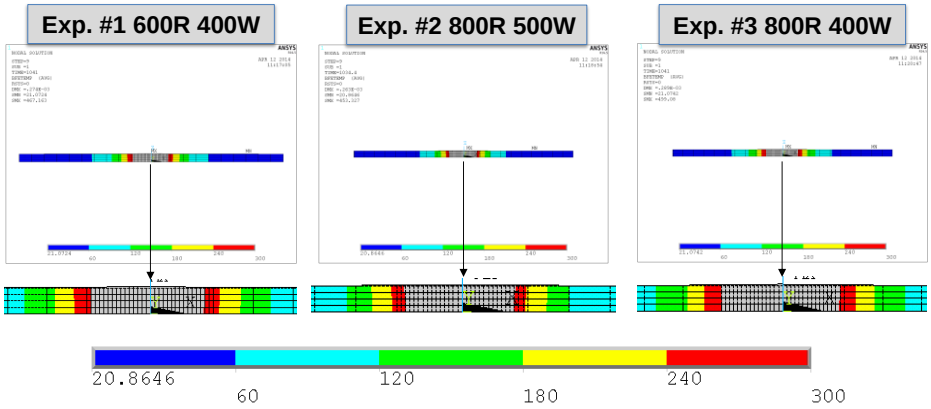

Fig. 82. Sectional temperature distribution of FSW.

There is almost no temperature gradient between the surface of top and bottom (during the FSW, heat is not applied only a top surface, but a bottom surface). Thus, almost no angular distortion due to the temperature gradient of the top and bottom surface. The work piece is expanding laterally during the heating, and then contract during the cooling. In Fig. 82, the gray color indicate over a 300℃.

Inherent strain is calculated in existing external constraint during welding. Generally, external constraint is applied until the work piece temperature reached at a room temperature during the FSW. It prevents movement of the work piece and welding deformation. Thus, inherent strain is calculated in existing external constraint of heating and cooling stage as shown in Fig. 83.

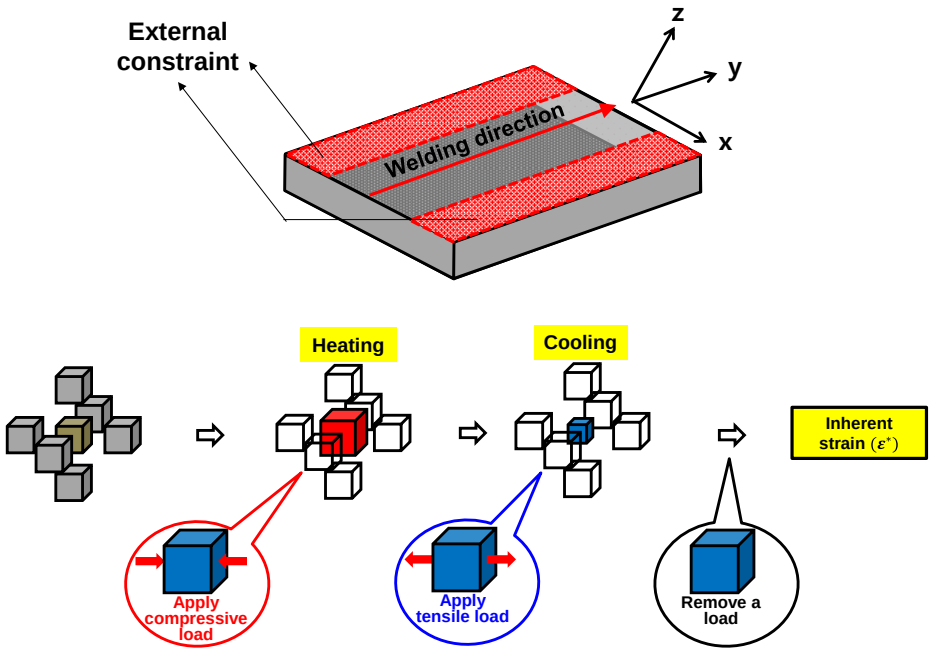

Fig. 83. Inherent strain model considered external constraint during FSW

When calculate inherent strain, add an x-direction compressive load and tensile load during the heating and cooling stage, respectively. After temperature of the work piece is reached a room temperature, remove an x-direction load. This is the final inherent strain.

In a previous literature [55], value of external constraint is not defined. In this study, value of external constraint is defined as distance from the weld centerline as shown in Fig. 84.

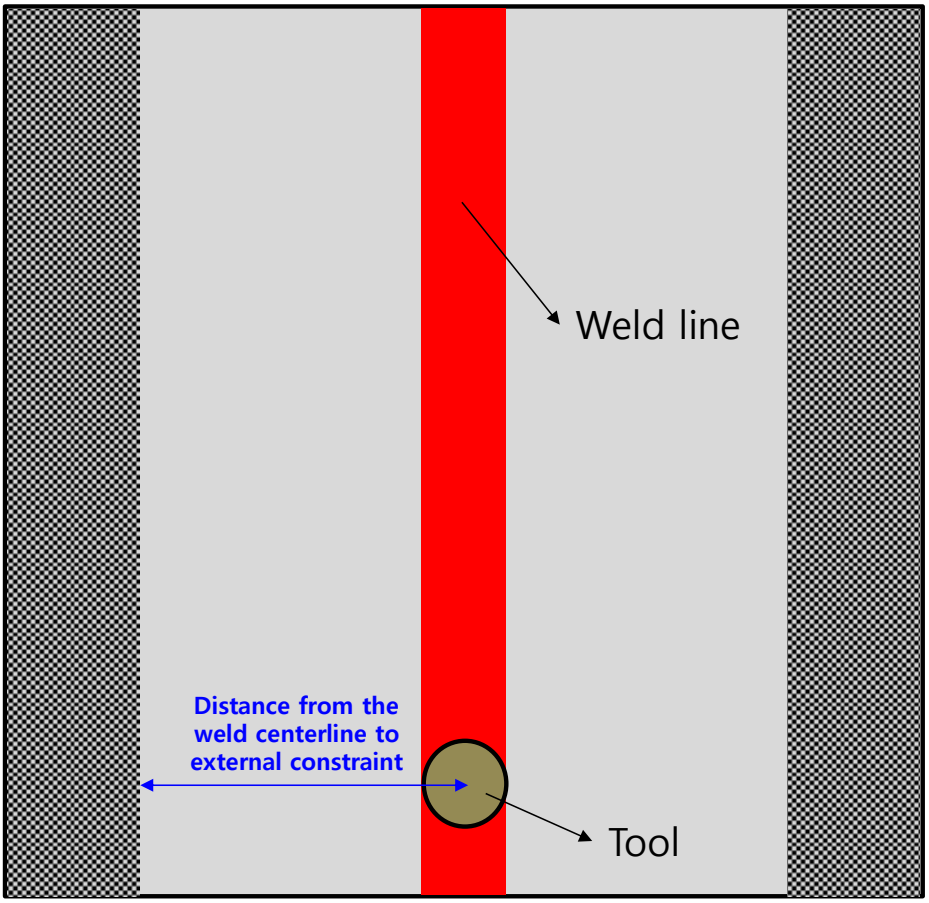

Fig. 84. Distance from the weld centerline to external constraint

As mentioned before, when calculate an inherent strain, add an x-direction load during the heating and cooling stage. In this time, x-direction force is defined by reaction force in external constraint. The reaction force is different during heating and cooling. Generally, inherent strain is greatly affected during cooling stage. However, there is a serious problem to calculate a reaction force. Because a reaction force is calculated by using thermal elasto-plastic analysis. Thus, other method is necessary to predict a reaction force. Before, predict a reaction force, the effect of reaction force during heating and cooling to

the residual stress distribution using reaction force of thermal elasto-plastic analysis results. Total 61 different thermal elasto-plastic analysis are carried out and welding condition and parameters are listed in Table 21. Of these, most serious three cases (No. 1, No. 25, and No. 47 in Table 21) are considered to compare a residual stress distribution in thermal elasto-plastic analysis and inherent strain method.

Table 21. Welding condition and parameter for reaction force data base

No	Rotation speed (RPM)	Welding speed (mm/min)	Thickness (mm)	Tool (SD x PD x PH mm)	External constraint (distance: mm)
1	800	100	6	22 x 5 x 5.7	80
2	800	200	6	22 x 5 x 5.7	80
3	800	400	6	22 x 5 x 5.7	80
4	800	500	6	22 x 5 x 5.7	80
5	800	600	6	22 x 5 x 5.7	80
6	600	400	6	22 x 5 x 5.7	80
7	800	400	6	22 x 5 x 5.7	80
8	1000	400	6	22 x 5 x 5.7	80
9	1200	400	6	22 x 5 x 5.7	80
10	1400	400	6	22 x 5 x 5.7	80
11	800	400	6	22 x 5 x 5.7	25
12	800	400	6	22 x 5 x 5.7	30
13	800	400	6	22 x 5 x 5.7	35
14	800	400	6	22 x 5 x 5.7	40
15	800	400	6	22 x 5 x 5.7	45

16	800	400	6	22 x 5 x 5.7	50
17	800	400	6	22 x 5 x 5.7	55
18	800	400	6	22 x 5 x 5.7	60
19	800	400	6	22 x 5 x 5.7	65
20	800	400	6	22 x 5 x 5.7	70
21	800	400	6	22 x 5 x 5.7	75
22	800	400	6	22 x 5 x 5.7	80
23	800	400	6	22 x 5 x 5.7	85
24	800	400	6	22 x 5 x 5.7	90
25	800	400	6	22 x 5 x 5.7	95
26	800	400	3	22 x 5 x 5.7	80
27	800	400	12	22 x 5 x 5.7	80
28	1000	300	3	12 x 3 x 2.5	25
29	1000	300	3	12 x 3 x 2.5	30
30	1000	300	3	12 x 3 x 2.5	35
31	1000	300	3	12 x 3 x 2.5	40
32	1000	300	3	12 x 3 x 2.5	45
33	1000	300	3	12 x 3 x 2.5	50
34	1000	300	3	12 x 3 x 2.5	55
35	1000	300	3	12 x 3 x 2.5	60
36	1000	300	3	12 x 3 x 2.5	65
37	1000	300	3	12 x 3 x 2.5	70
38	1000	300	3	12 x 3 x 2.5	75
39	1000	300	3	12 x 3 x 2.5	80
40	1000	300	3	12 x 3 x 2.5	85
41	1000	300	3	12 x 3 x 2.5	90
42	1000	300	3	12 x 3 x 2.5	95
43	600	300	12	32 x 10 x 9	35
44	600	300	12	32 x 10 x 9	40
45	600	300	12	32 x 10 x 9	45
46	600	300	12	32 x 10 x 9	50

47	600	300	12	32 x 10 x 9	55
48	600	300	12	32 x 10 x 9	60
49	600	300	12	32 x 10 x 9	65
50	600	300	12	32 x 10 x 9	70
51	600	300	12	32 x 10 x 9	75
52	600	300	12	32 x 10 x 9	80
53	600	300	12	32 x 10 x 9	85
54	600	300	12	32 x 10 x 9	90
55	600	300	12	32 x 10 x 9	95
56	1250	280	6.4	19 x 6.35 x 6	20
57	1250	280	6.4	19 x 6.35 x 6	40
58	1250	280	6.4	19 x 6.35 x 6	55
59	1250	280	6.4	19 x 6.35 x 6	60
60	1250	280	6.4	19 x 6.35 x 6	65
61	1250	280	6.4	19 x 6.35 x 6	80

The reaction force of No. 1, No. 25, and No. 47 using thermal elasto-plastic analysis are plotted in Fig. 85.

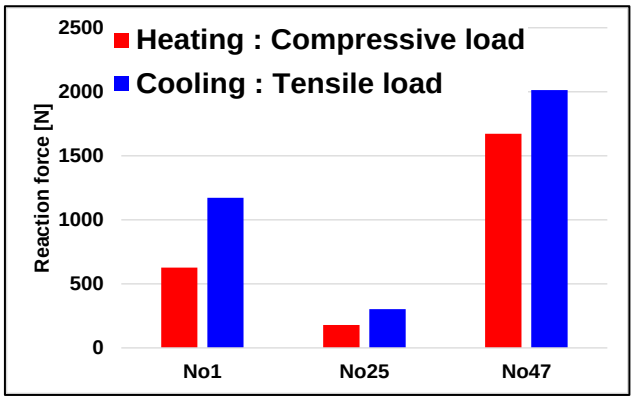

Fig. 85. Reaction force of three different cases.

In this study, three different methods for calculate an inherent strain. Assumed that reaction force during heating is $-|A|$, and reaction force during cooling is $|B|$. CASE III is reflected a real phenomenon Whereas, CASE I and CASE II are used to representative value A and B for inherent strain calculation.

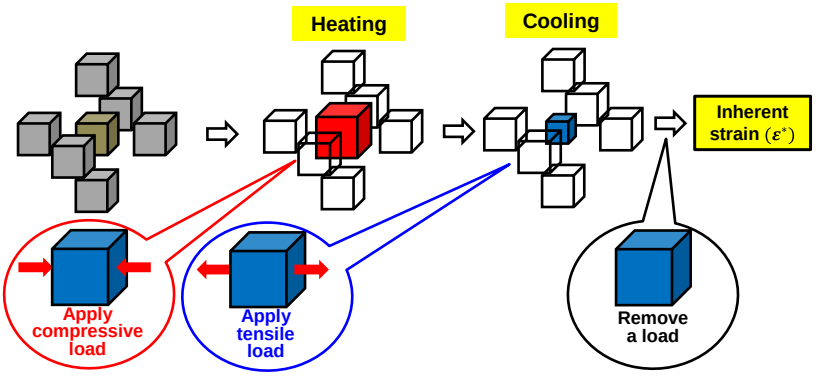

Method	Heating	Cooling
CASE I	$-\|A\|$	$\|A\|$
CASE II	$-\|B\|$	$\|B\|$
CASE III	$-\|A\|$	$\|B\|$

Fig. 86. Effect of reaction force during heating and cooling for residual stress distribution.

Three different inherent strain values are calculated using three different methods as shown in Fig. 86. These inherent strain values are inputted in FE model. This stage is expressed as inherent strain input in Fig. 80.

In a previous literature [55], welding analysis model is divided into two regions, i.e. 1st and 2nd heat affected areas, depending on the level of temperature variation. Then, TG is determined by average temperature gradient of each region as

shown in Fig. 87. Inherent strain value is inputted in twice of leg length. It is applied in the conventional fusion welding.

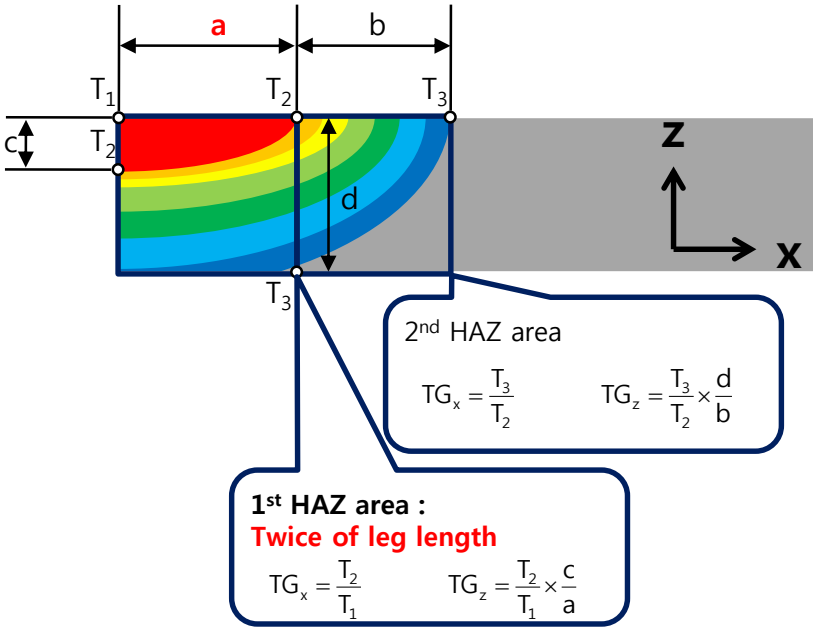

Fig. 87. Definition of TG in the conventional fusion welding analysis model [55].

However, above method cannot be reflected the characteristic of FSW. In this study, TG_x is defined as T_2 over T_1.

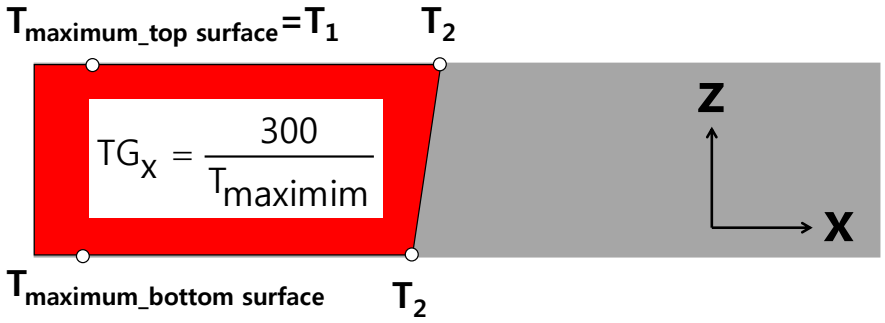

Fig. 88. Definition of TG in the FSW analysis model

T_2 in Fig. 88 is defined by location of maximum tensile residual stress. This temperature will be related with HAZ region. For the value of T_2, several thermal elasto-plastic analysis results of Table 19 are used. In Fig. 78, ten cases residual stress distribution are compared. The maximum residual stress location in advancing side and the temperature of its location are listed in Table 22.

Table 22. Maximum residual stress location in AS and the temperature of it location in Fig. 78.

No	Rotation speed (RPM)	Welding speed (mm/min)	Temperature (° C)	Maximum residual stress location in AS (mm)
No. 1	800	100	246.65	34
No. 2	800	200	266.47	24
No. 3	800	400	294.56	15
No. 4	800	500	274.58	14
No. 5	800	600	337.36	11
No. 6	600	400	300.61	14
No. 7	800	400	294.56	15
No. 8	1000	400	310.22	15
No. 9	1200	400	325.39	15
No. 10	1400	400	338.49	15

On the whole, the maximum residual stress is located in about 300℃ temperature. Thus, the T_2 temperature is fixed as 300℃ in this study. The location of T_2 will be used to input a calculated inherent strain in next step. Table 23 shows the difference of maximum residual stress location between the

thermal elasto-plastic result and when T_2 is fixed as 300℃. Actually, TG_x value is different in each nodes. However, the difference is a little, and represent value of TG_x can be used. Thus, in over a 300℃ region, represent value of TG_x is used to calculate an inherent strain. Furthermore, inherent strain value is different in each nodes. Because maximum temperature is different in each nodes. However, its difference is little effected in inherent strain value. Thus, in the present study, we will use represent value of TG_x using maximum temperature and 300℃, and represent value of inherent strain using maximum temperature. At this time, the inherent strain value at maximum temperature In addition, external constraint will be considered to calculate an inherent strain. Structural analysis will be carried out using above calculated inherent strain which is inputted in the location of 300℃.

Table 23. Maximum residual stress location in different conditions

Design ation	Results of thermal elasto-plastic		At the 300° C	
	Tempe rature (° C)	Maximum residual stress location at top AS (mm)	Tempe rature (° C)	Maximum residual stress location at top AS (mm)
No. 1	246.65	34	300	27
No. 2	266.47	24		22
No. 3	294.56	15		15
No. 4	274.58	14		14
No. 5	337.36	11		12
No. 6	300.61	14		14
No. 7	294.56	15		15
No. 8	310.22	15		16
No. 9	325.39	15		17
No. 10	338.49	15		18

In Table 23, low welding speed such as No. 1 and No. 2, the

difference of maximum residual stress location is large. However, the maximum residual stress location is generally corresponded in Table 23. Thus, the assumption, T_2 is 300℃, is reasonable.

Now, TG_x can be calculate as shown in Fig. 89, and Eq. (18).

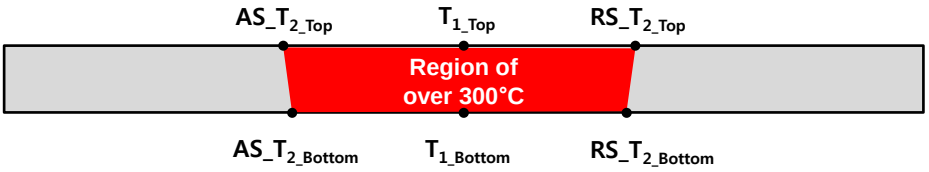

Fig. 89. Temperature gradient of x-direction (TG_x)

$$TG_{x_Top} = \frac{300}{T_{1_Top}}$$
$$TG_{x_Bottom} = \frac{300}{T_{1_Bottom}} \quad (18)$$

In Fig. 89, $AS_T_{2_Top}$, $AS_T_{2_Bottom}$, $RS_T_{2_Top}$, and $RS_T_{2_Bottom}$ (these are represented as T_2) are fixed 300℃.

In summary, inherent strain method is depicted in Fig. 90.

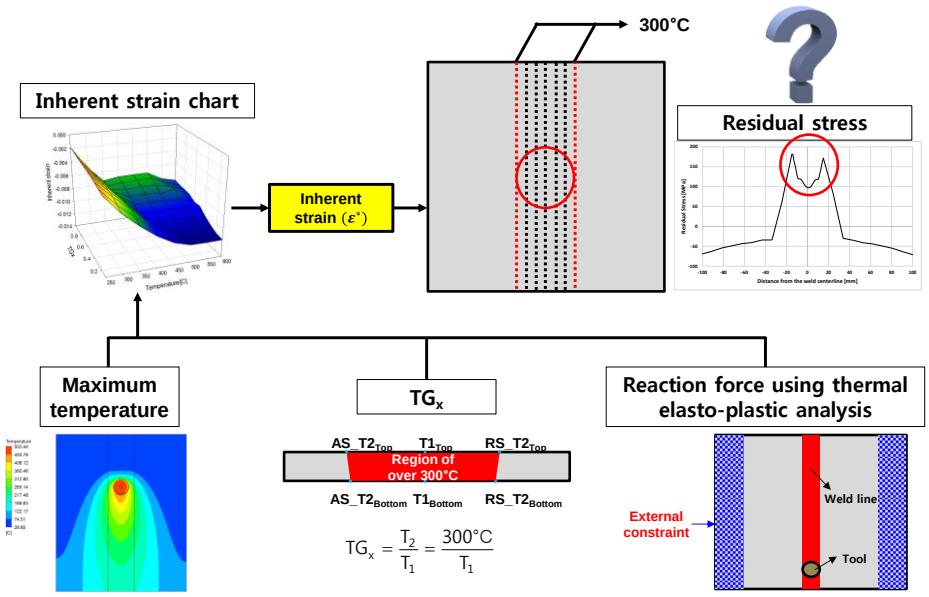

Fig. 90. Location of inherent strain input and weighting of center value.

In Fig. 90, inherent strain value is calculated using maximum temperature, temperature gradient in x-direction, and reaction force. Inherent strain value is inputted in 300℃. However, the final residual stress distribution has an 'M' shape. Generally, temperature distribution of FSW is plotted in Fig. 91. The linear velocity of the tool is linearly proportional to the distance from the center of the tool. Thus, the temperature of center is lower than the edge of the tool.

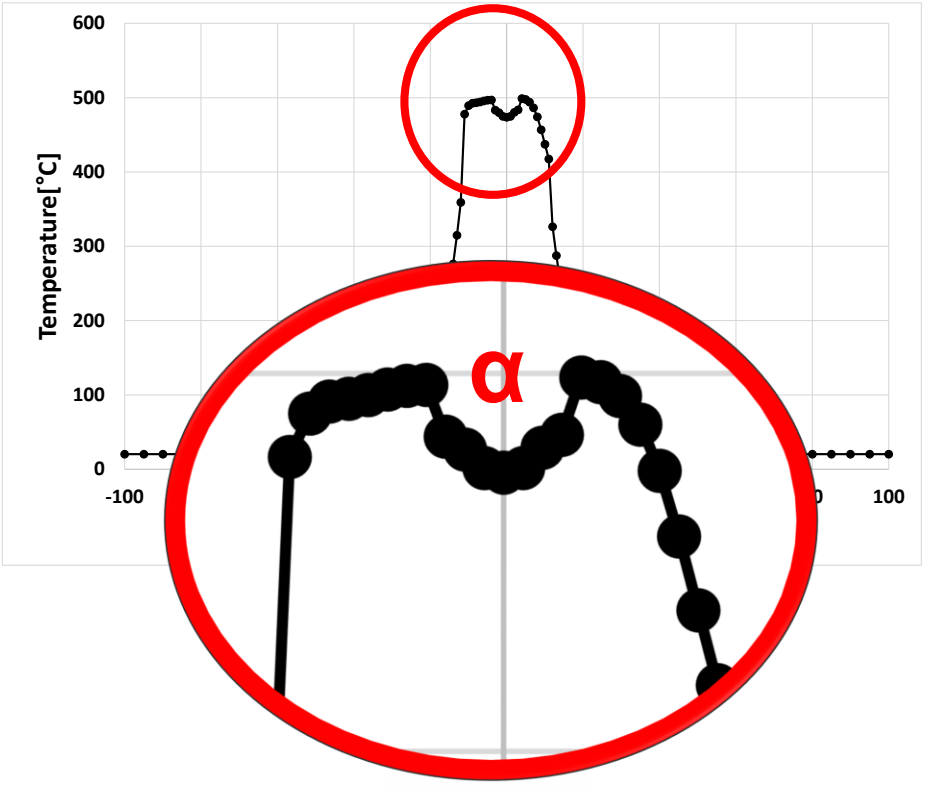

Fig. 91. Temperature distribution of FSW.

The ratio between the center and edge of the tool is defined α and it multiply by inherent strain. This fixed inherent strain is defined $\varepsilon^{*\prime}$ and inputted in center of FE model. Other nodes which is located between the center and 300℃ are linearly interpolated as shown in Fig. 92.

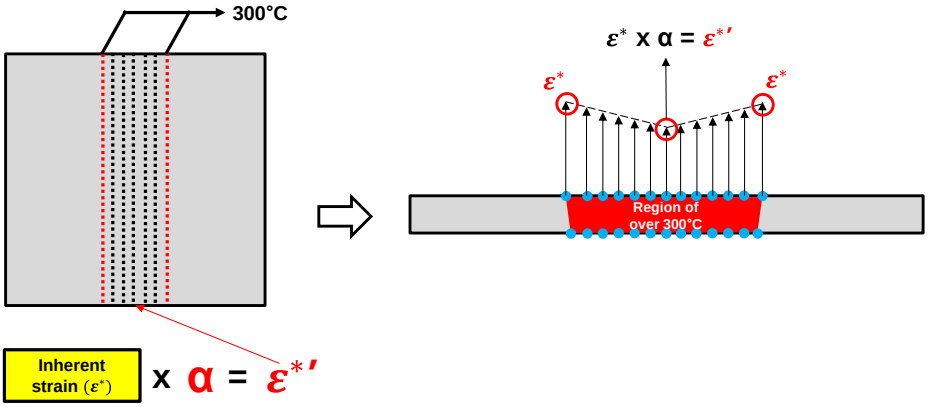

Fig. 92. Interpolated inherent strain values and input location.

Now, residual stress distribution is calculated using elastic structural analysis with inherent strain for No. 1, No. 25, and No. 47. Maximum tensile residual stress in y−direction are compared in Fig. 93.

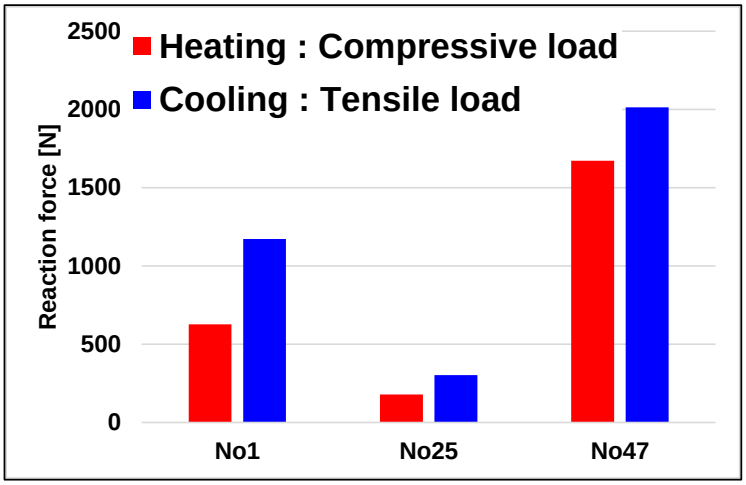

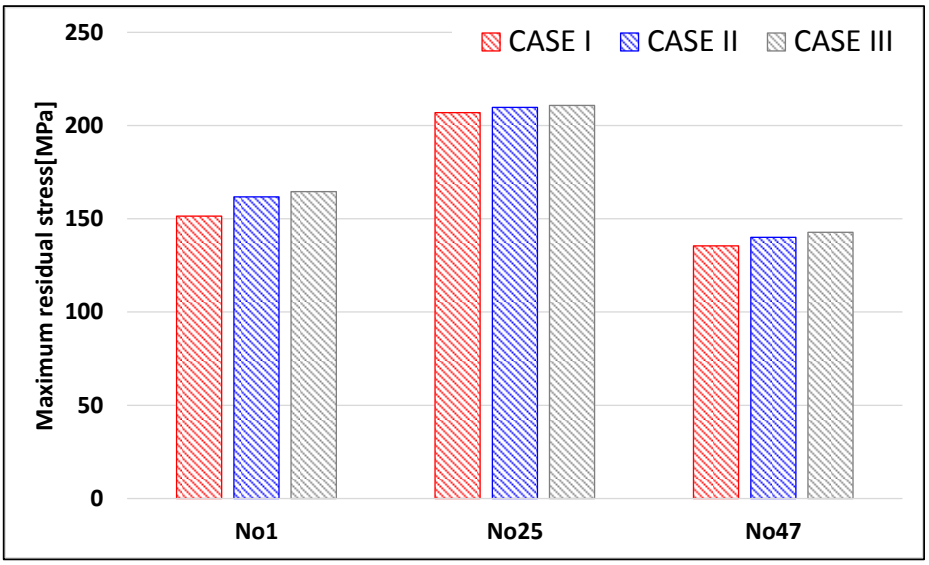

Fig. 93. Maximum tensile residual stress in y−direction using three different methods.

Residual stress distribution in y−direction of No. 1 is plotted in Fig. 94.

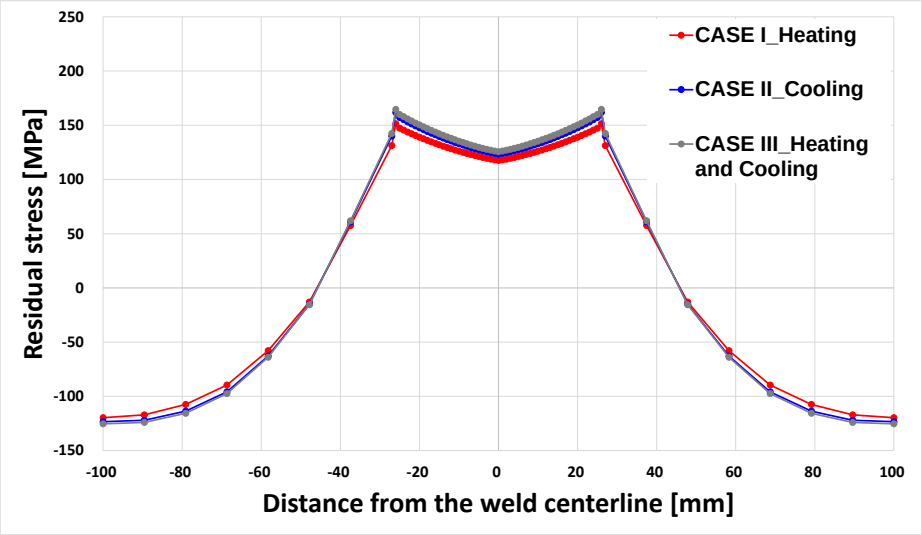

Fig. 94. Residual stress distribution in y-direction of No. 1

In Figs. 93 – 94, CASE II and CASE III results are almost same. This means that inherent strain is decided during cooling. Yield stress is higher during cooling stage. Thus, the absolute value of the inherent strain is large during cooling stage. From this time forward, reaction force is considered during cooling stage (CASE II in Fig. 85).

7.3. Predict a reaction force during cooling stage using neural networks

In section 7.2, reaction force is calculated using elasto-plastic analysis. However, it also takes a lot of calculation time. In addition, it is not correspond with advantage of inherent strain method. Thus, in this section, the reaction force is calculated by using other prediction method.

In order to calculate an inherent strain, the maximum temperature, temperature gradient in x−direction, and reaction force during cooling stage should be known. Maximum temperature and temperature gradient are calculated by using CFD heat transfer analysis. As mentioned above, the problem is the reaction force. Fig. 95 (a) – (c) shows the inherent strain according to maximum temperature, temperature gradient in x−direction, and reaction force, respectively.

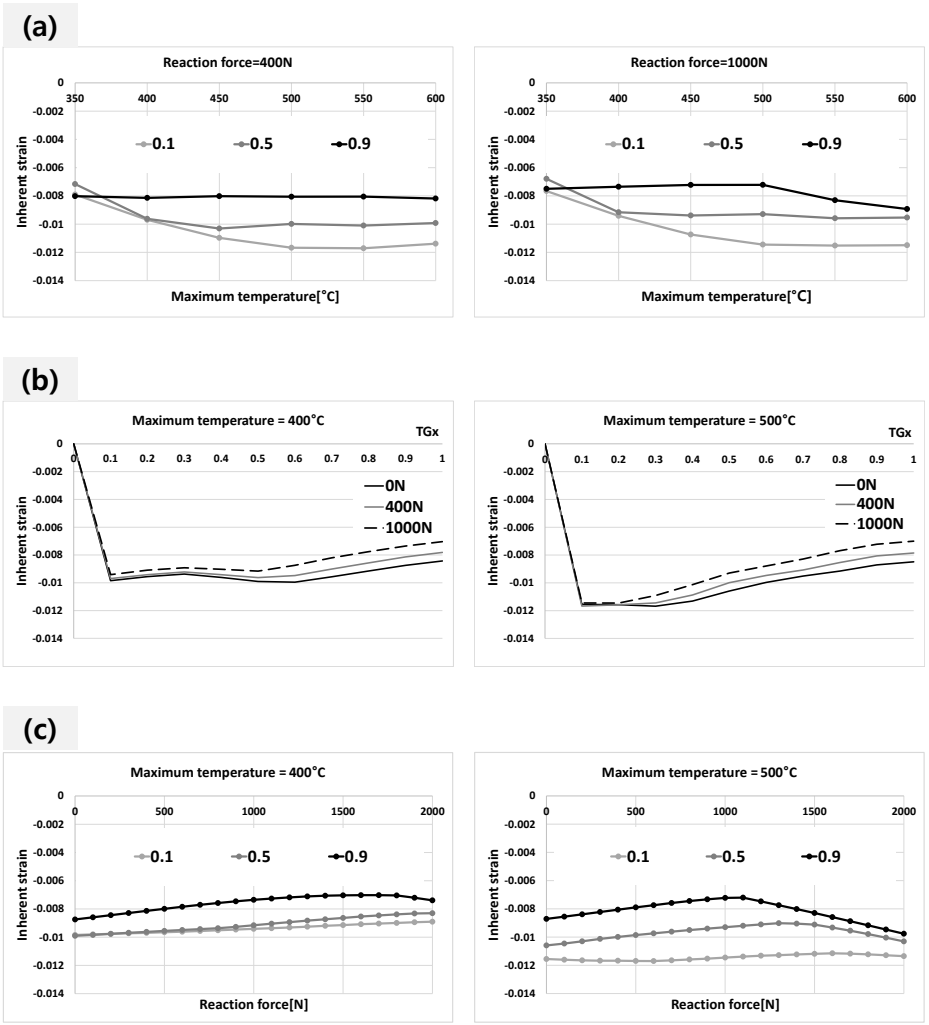

Fig. 95. Inherent strain according to (a) maximum temperature, (b) temperature gradient in x-direction, and (c) reaction force.

In Fig. 95, an inherent strain is affected by above three values. In the present study, neural networks are considered.

Neural networks are defined as follows: in order to solve the problem in a manner similar to the method of processing problems using the human brain, the structure being used in the computer. To process the signal, neurons are connected to the neurons tissue of the basic structure in the human brain.

Likewise in forming a network of neurons as a mathematical model are connected to each other, it is a neural network. In distinction to the neural network biological, it is referred to as an artificial neural network. An interconnected network of simple processing elements. It is powerful data modeling tool that is able to capture and represent complex input and output relationships.

The neural network, because the role of the handler that operates each neuron independently, parallelism is excellent. Furthermore, since the information is spread across many extensions, there is a fault tolerance without a significant impact on the overall system even if a problem occurs in some neurons. Since the learning ability of a given environment, it has been used in the field of artificial intelligence, and it is used in many fields such as character recognition, image processing, natural language processing, and voice recognition. The advantages of neural network are as follows.

- ✓ It can solve data easily for complex and diverse.
- ✓ Regardless of the quantitative variables and qualitative variables, all analyzes are possible.
- ✓ Non-linear combination of input variables between are possible, predictive power is superior.

On the other hand, it has the following disadvantages.

- ✓ It show only the prediction results and classification results.
- ✓ It is hard to explain the reason and cause of the generation of the results.
- ✓ It select a sample at random when analyzing the data, the result of the regression analyses are not match in the same input environment.

A neural network consists input layer, hidden layer, and output layer. Each layer have input nodes (x in Fig. 96), hidden nodes (H in Fig. 96), and output nodes (y in Fig. 96) as shown in Fig. 96. Each layer consist of one or more nodes and the arrow lines between the nodes indicate the flow of information from on node to the next.

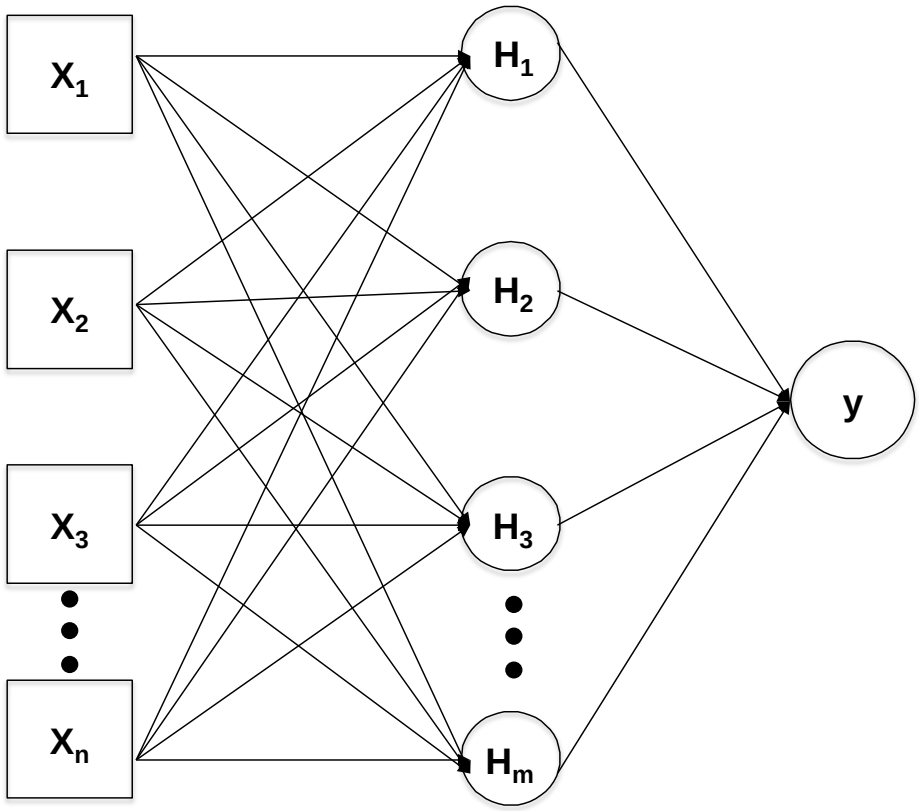

Fig. 96. Conceptual diagram of a neural network.

There are several type of neural networks depending on the purpose. In this case, use input values (temperature distribution and geometry conditions) to predict some output (reaction force during cooling stage), and it is called prediction network type. Thus, back propagation networks are used. Back propagation is an example of a feed forward network, which means that the data flows only in a forward direction. Deciding how the processing element in a network are connected, how the processing element's process their information, and how the connection strengths are modified all go into creating a neural network.

Once a network has been structured for a particular application, that network is ready to be trained. To start this process the initial weights are chosen randomly. So, the result of the regression analyses are not match in the same input environment. Then, the training, or learning, begins. The training approaches are divided into two: supervised and unsupervised. Supervised training involves a mechanism of providing the network with the desired output either by manually grading the network's performance or by providing the desired outputs with the inputs. On the other hand, unsupervised training is where the network has to make sense of the inputs without outside help. In this study, 61 cases in Table 21 of thermal elasto-plastic analysis were carried out, and the reaction force data were collected each case. Thus, supervised training is used to make neural networks. In supervised training, the error is computed the difference between the prediction value and desired output as shown in Fig. 97.

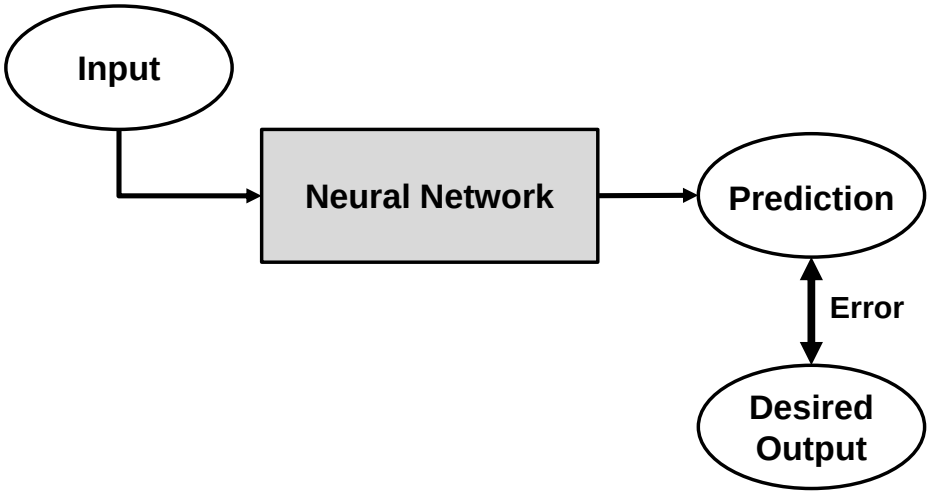

Fig. 97. Supervised training in neural network.

For a training neural network, input data which is affected on reaction force were investigated. There are welding speed, rotation speed, maximum temperature, temperature gradient, location of external constraint (distance from the weld centerline to external constraint), thickness of work piece, tool dimension, and etc. All the input data is expressed a constant value except temperature gradient. Thermal stress affects to the reaction force, and the temperature gradient severely affects to the thermal stress. Thus, in order to consider temperature gradient as input data in neural networks, it should be represented by other factors that has a constant value. The relationship between the reaction force and welding parameters are denoted in Fig. 98.

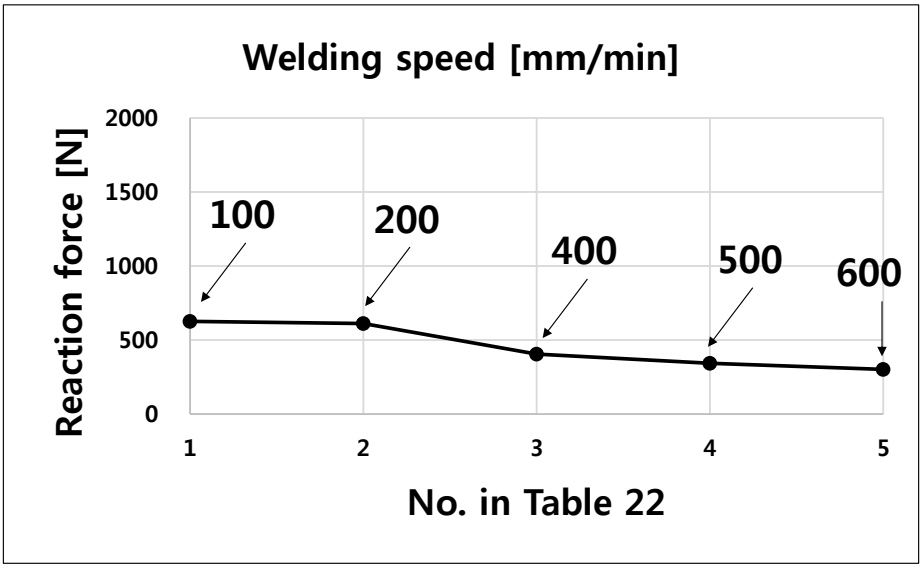
Welding speed [mm/min]
Reaction force [N]
2000
1500
1000
500
0
100
200
400
500
600
1
2
3
4
5
No. in Table 22

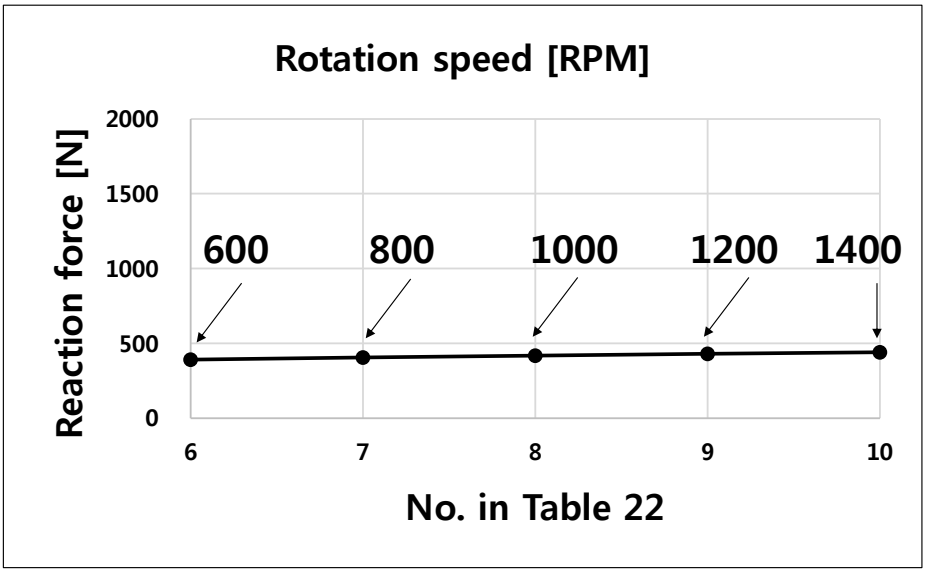
Rotation speed [RPM]
Reaction force [N]
2000
1500
1000
500
0
600
800
1000
1200
1400
6
7
8
9
10
No. in Table 22

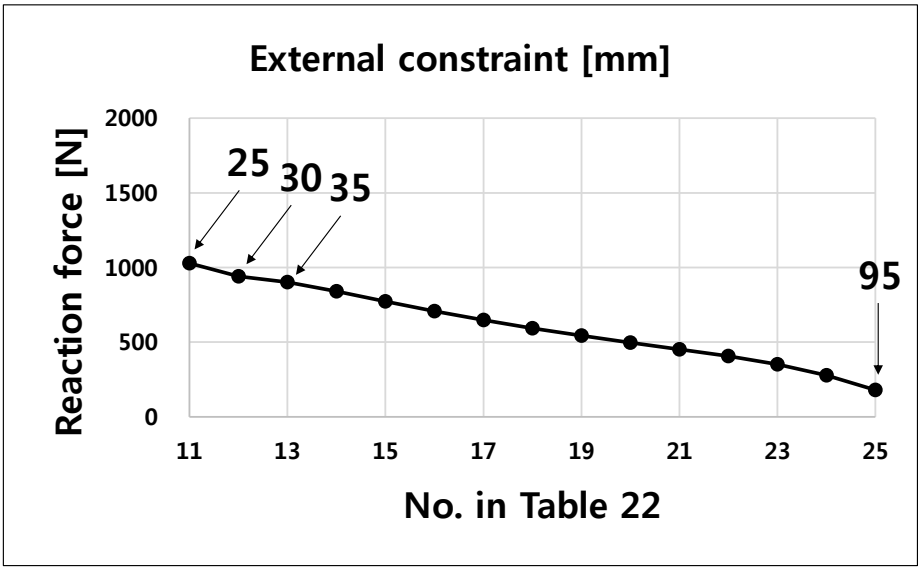
External constraint [mm]
Reaction force [N]
2000
1500
1000
500
0
25
30
35
95
11
13
15
17
19
21
23
25
No. in Table 22

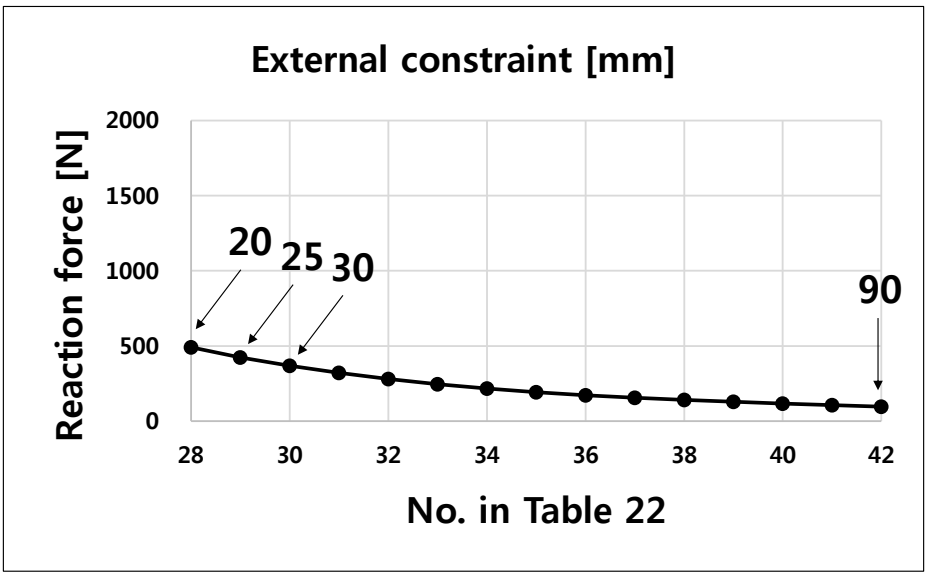
External constraint [mm]
Reaction force [N]
2000
1500
1000
500
0
20
25
30
90
28
30
32
34
36
38
40
42
No. in Table 22

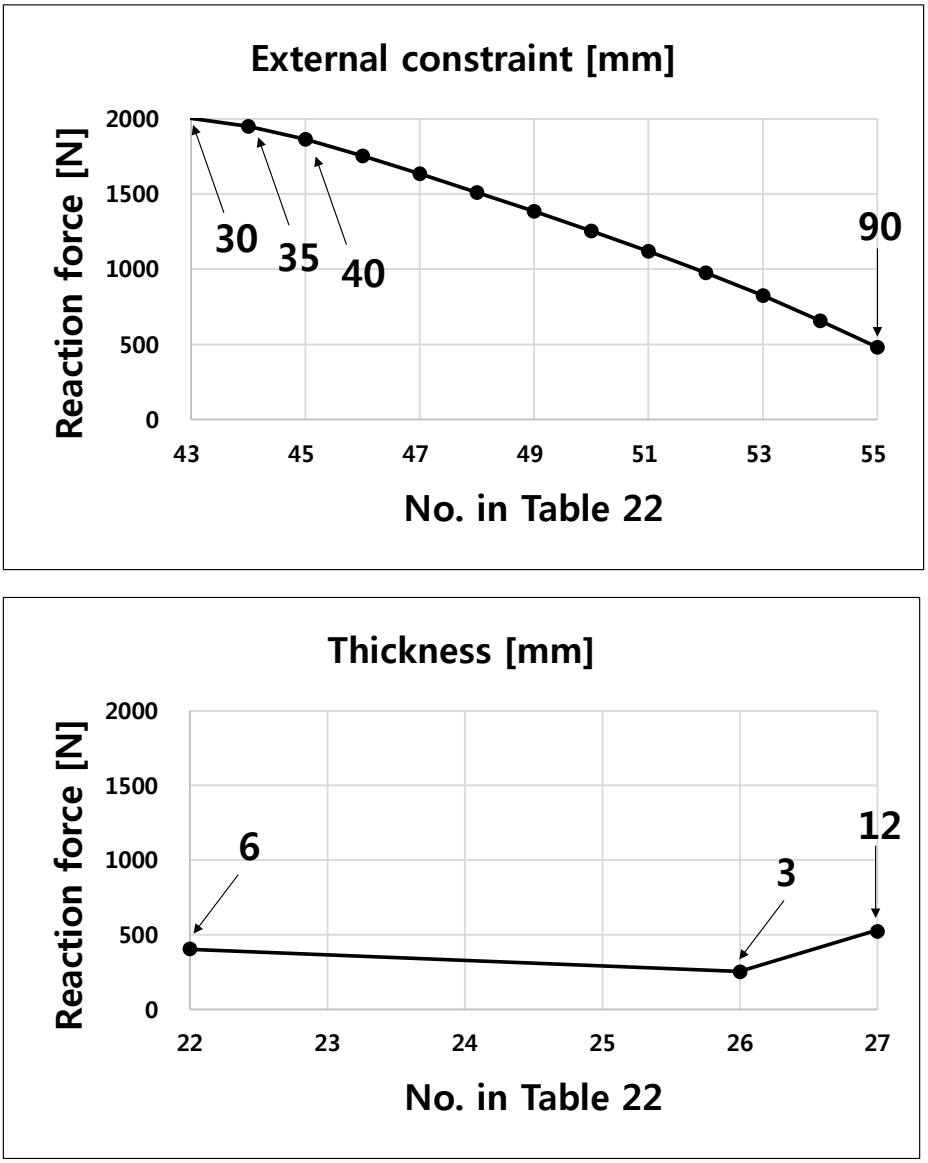

Fig. 98. Relationship between reaction force and welding parameters

In this study, welding speed, rotation speed of the tool, and tool dimension are represented by maximum temperature and temperature gradient. Thus, input data can be summarized as shown in Fig. 99.

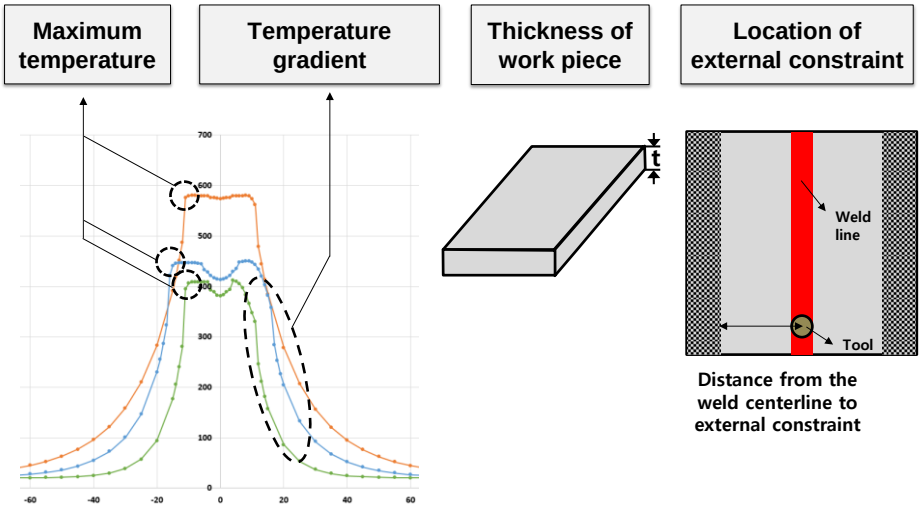

Fig. 99. The factors affecting the reaction force.

In order to quantify the temperature gradient, it is intended approximated using a polynomial function or a log function. At this time, whether considering the maximum temperature of the temperature distribution function was examined first. In Fig. 100, (a) is considering the maximum temperature of No. 1 in Table 22, (b) is a case where it does not take into account the maximum temperature. In consideration of the maximum temperature, it is difficult to approximate data of temperature gradient by a trend line. Maximum temperature is already considered in order to act as a factor for calculating the reaction force using neural network. Thus, there is no problem maximum temperature is missing in temperature distribution graph.

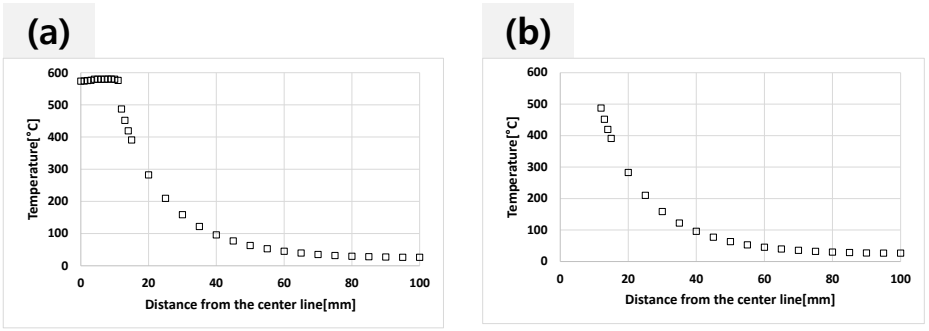

Fig. 100. Temperature distribution of No 1 case: (a) Consider the maximum temperature, (b) Do not consider the maximum temperature.

Next, it was examined for when taking the natural logarithm of the temperature distribution data. Taking the natural logarithm of the temperature distribution data, as shown in Fig. 101, it can be seen that the slope of the graph changes gently.

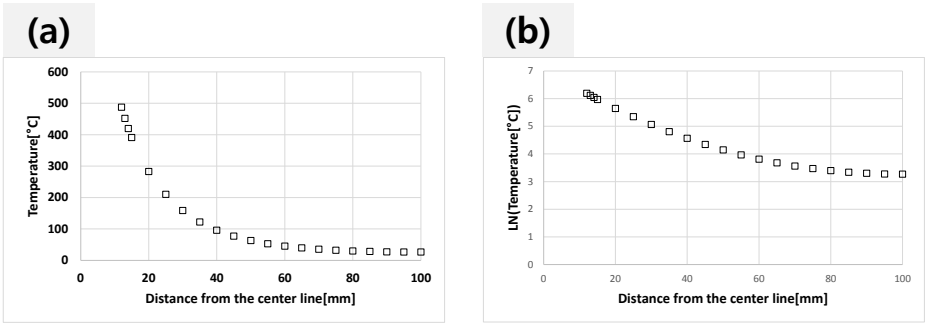

Fig. 101. Temperature distribution of No 1 case (a) As it is, (b) Taking the value of the natural logarithm.

Using this, several cases in Table 22(except No. 7) are used to approximate a trend line. In the present study, logarithm function, and 2 – 4 order polynomial function were used and the results are plotted in Figs. 102 – 105. In Figs. 102 – 105, square box is the heat transfer analysis result of the

temperature data, and dot line represents a trend line of the temperature data.

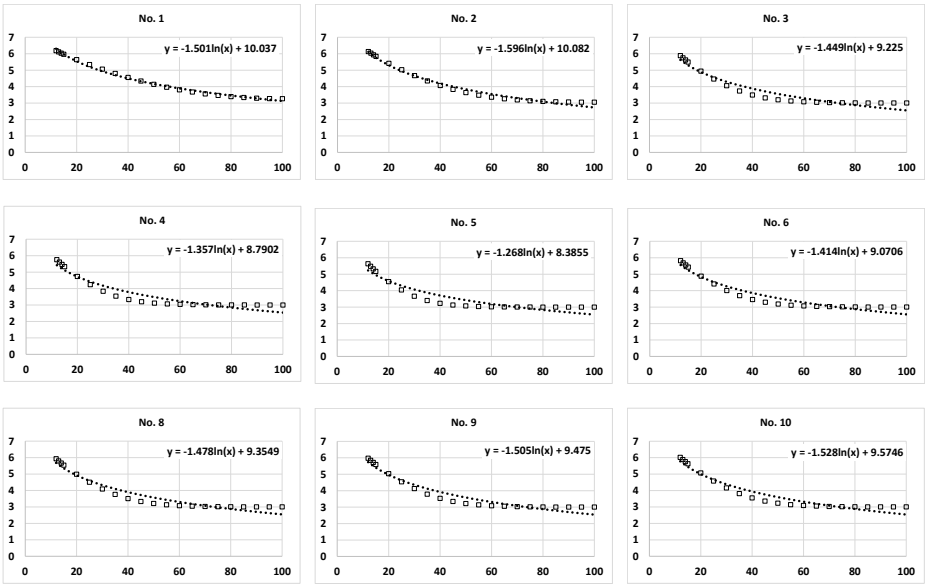

Fig. 102. Approximated temperature distribution by a logarithmic function.

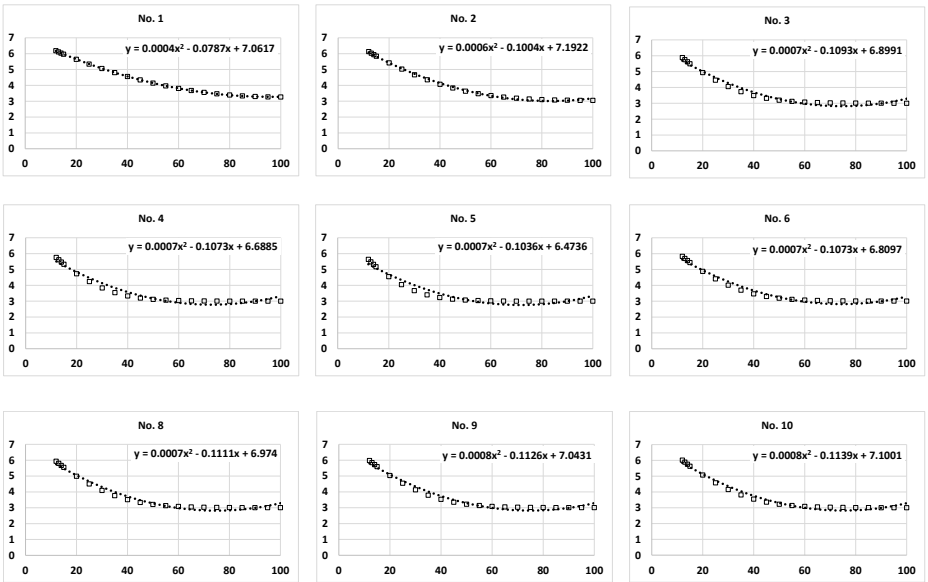

Fig. 103. Approximated temperature distribution by a 2nd-order polynomial function.

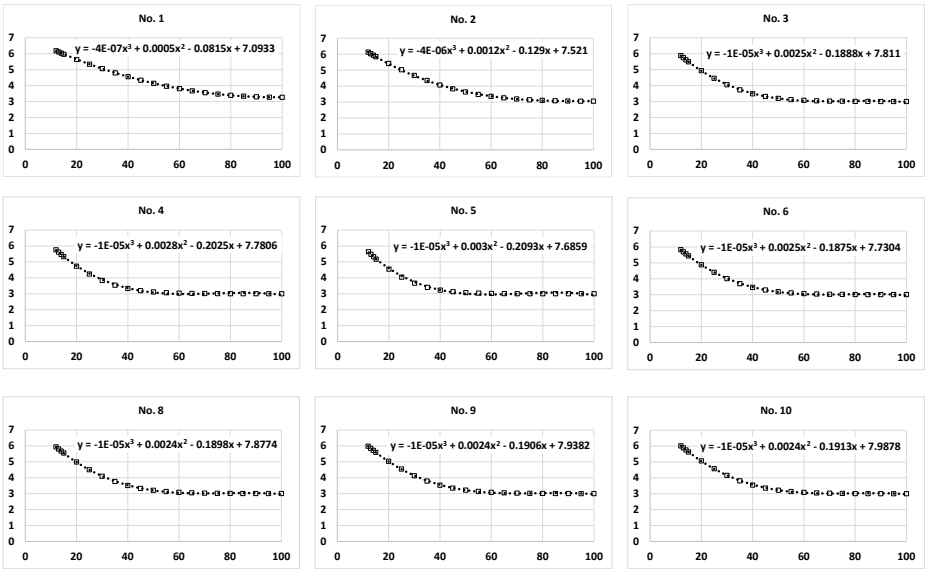

Fig. 104. Approximated temperature distribution by a 3rd-order polynomial function.

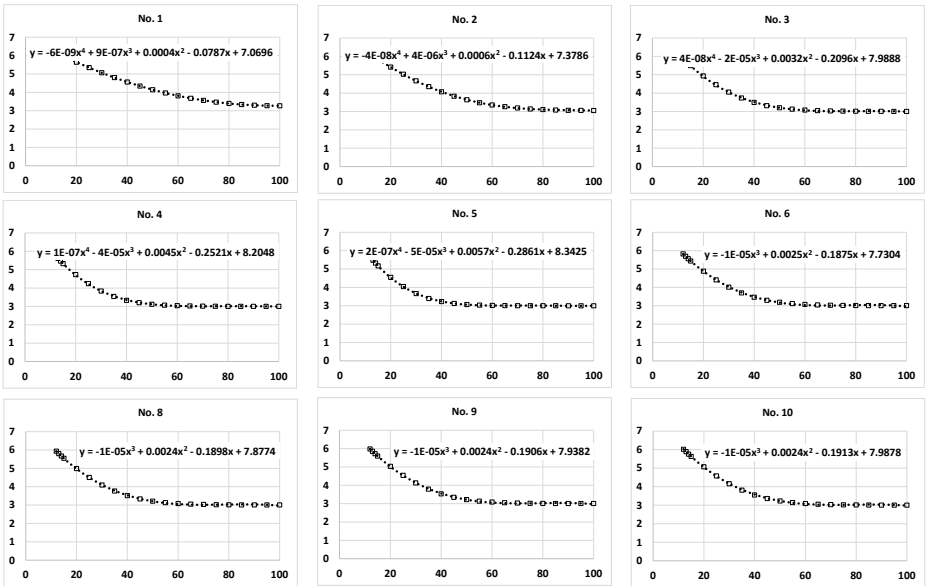

Fig. 105. Approximated temperature distribution by a 4th-order polynomial function

Temperature data were approximated by a quadratic polynomial functions and logarithmic functions, it can be seen that there is a difference between the temperature distributions.

In contrast, when it was approximated by a third order or quartic polynomial, it is possible to know that substantially the same temperature distribution in practice. Therefore, in this study, in order to minimize the input factors using the temperature trend line approximated by a third order polynomial function.

In this study, the structure of the neural network is used to predict the reaction force during cooling stage is shown in Fig. 106. In Fig. 106, the number of node in the input layer is 7, the number of node in the output layer is 1, and the number of node in the hidden layer is 9. In general, the number of node in hidden layer is equal or greater than the sum of the node in input and output layer.

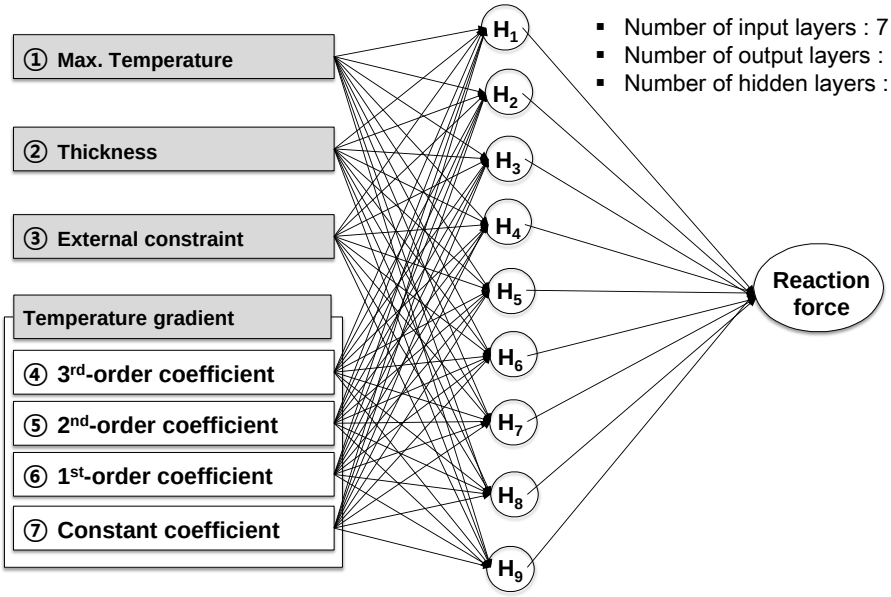

Fig. 106. The structure of the neural networks for predict a reaction force during cooling stage.

In order to make a function of neural networks thermal elasto-plastic analysis were carried out, and the welding parameters are summarized in Table 21.

Thermal elasto-plastic analysis were carried out about total 61 cases in Table 21. Then, input data and output data were arranged as Fig. 107.

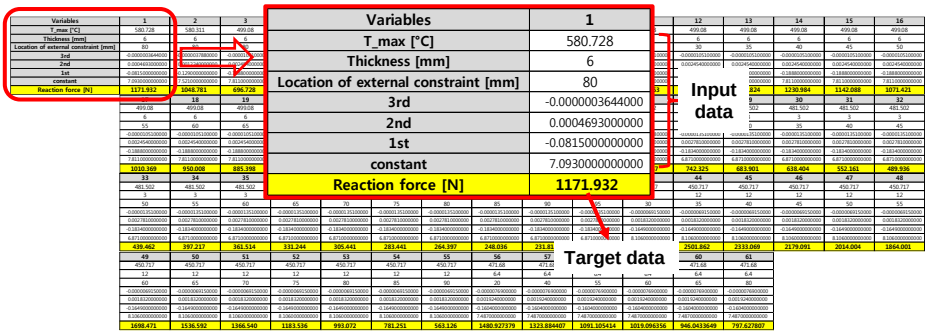

Fig. 107. Input and target data base for make a neural networks function.

Of the database constructed in this way, randomly select the 55 cases and train the neural network. Then, it was verified work put in function of the neural network trained by using the data of the remaining six. In this method, it is repeated five times as shown in Fig. 108. Finally, it is confirmed that input value was appropriate to predict the reaction force during cooling stage by using a neural network. The verified results are listed in Table 24. In Table 24, TEP means thermal elasto-plastic and NN means neural network.

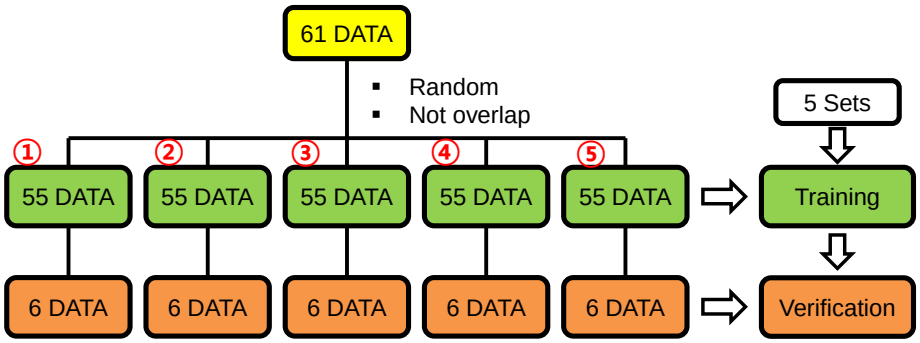

Fig. 108. Verification of neural networks.

Table 24. Comparison of thermal elasto-plastic analysis and neural networks results for reaction force during cooling stage

①	Reaction force [N]		Error
	TEP	NN	
4	578.50	465.19	19.59
29	683.90	668.85	2.20
34	397.22	371.28	6.53
37	305.44	261.54	14.37
50	1536.59	1534.98	0.10
54	781.25	867.71	-11.07

②	Reaction force [N]		Error
	TEP	NN	
3	696.73	619.23	11.12
17	1010.37	977.59	3.24
30	638.40	519.01	18.70
38	283.44	251.55	11.25
47	2014.00	2045.69	-1.57
55	563.13	596.90	-6.00

③	Reaction force [N]		Ratio
	TEP	NN	
10	828.55	778.48	6.04
20	821.64	829.78	-0.99
26	453.23	518.71	-14.45
32	489.94	545.41	-11.32
35	361.51	352.15	2.59
48	1864.00	1859.80	0.23

④	Reaction force [N]		Error
	TEP	NN	
7	696.73	697.72	-0.14
14	1230.98	1181.19	4.04
41	231.81	212.54	8.32
52	1183.54	1131.34	4.41
53	993.07	955.73	3.76
58	1091.11	1154.41	-5.80

⑤	Reaction force [N]		Error
	TEP	NN	
8	742.47	741.46	0.14
18	950.01	943.85	0.65
22	696.73	691.45	0.76
25	302.90	441.59	-45.79
33	439.46	436.79	0.61
44	2501.86	2487.09	0.59

In Table 24, predict of reaction forces used to neural network are suitable.

In order to implement the neural networks, 'Neural Network Toolbox in MATLAB' is used. In summary, an interactive process for training neural networks is described in Fig. 109.

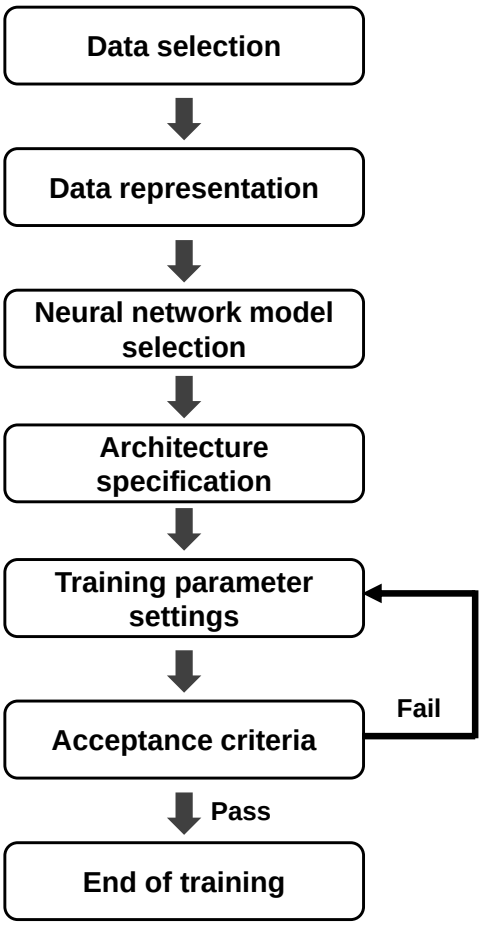

Fig. 109. Interactive process for training neural networks.

After finish a verified effectiveness of neural network, final neural network function is trained using 61 data in Table 25.

Maximum temperature, thickness, external constraint, and temperature gradient (coefficients of 3rd polynomial expression) are needed for input data. Reaction force during cooling (output data) is predicted by using below neural networks function. Thus, thermal elasto-plastic analysis is unnecessary. The final neural networks structure is shown in Fig. 110.

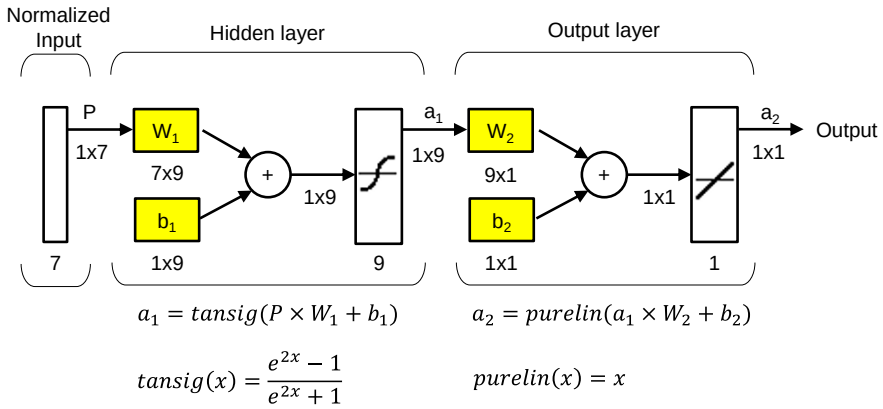

Fig. 110. Structure of neural networks.

In Fig. 110, weight and bias matrix for reaction force during cooling stage is listed in Table 25.

Table 25. Weight and bias matrix for reaction force.

W_1 [7x9]	1	2	3	4	5	6	7	8	9
1	-0.60478	-1.2369	0.68571	-1.0285	0.89775	-0.80415	-0.7936	-1.1837	1.218
2	0.31821	-0.21229	0.32402	-1.1476	0.41112	-0.35437	-0.3257	-1.6651	-1.6728
3	-0.28887	3.6072	-1.1977	-0.0308	-1.8327	-1.5638	0.27493	1.859	1.226
4	-0.63557	0.027068	-2.0955	-0.19695	0.44926	0.2955	2.1101	1.3407	-0.51481
5	-0.98615	0.30253	-0.01931	-0.24815	-0.71709	0.78561	0.27987	-0.75542	0.5932
6	1.0545	0.062125	-0.10121	0.11339	0.40685	-1.0694	0.79619	-0.22846	-1.2511
7	1.3656	0.4157	-0.33967	0.78327	0.55699	-0.14886	1.2671	1.4765	-0.69644

b_1 [7x9]	1	2	3	4	5	6	7	8	9
1	1.7659	1.4783	-1.7885	2.0688	0.65073	0.37809	1.6804	-2.9523	2.8605

W_2 [9x1]	1
1	-0.34976
2	-0.07029
3	0.20203
4	-0.56513
5	0.15895
6	0.066158
7	0.64697
8	-1.0464
9	-0.64364

b_1 [1x1]	1
1	-0.21693

When using this function, input nodes and output node have to normalize. The minimum and maximum data are listed in Table 26, and these are used to normalize process.

Table 26. Minimum and maximum values of input data for 61 data base using thermal elasto-plastic analysis results

	Minimum	Maximum
Maximum temperature [°C]	412.1	580.7
Thickness [mm]	3	12
Location of external constraint [mm]	20	95
3^{rd}-order coefficient	-1.397E-05	-3.644E-07
2^{nd}-order coefficient	4.693E-04	3.012E-03
1^{st}-order coefficient	-2.093E-01	-8.150E-02
constant coefficient	6.871	8.106
Reaction force [N]	212.94	2632.49

7.4. Inherent strain chart

Inherent strain chart considering external constraint is calculated using maximum temperature, temperature gradient, and reaction force. Temperature gradient is divided as TG_x, TG_y, and TG_Z. As mentioned before, TG_y is 1, and TG_z is almost 1 as shown in Fig. 82. In this study, TG_z is assumed 0.98. Maximum temperature is 300℃ to 600℃ at 50℃ intervals. The melting point of AA 6061-T6 is about 580℃. In addition, when the maximum temperature is not reached at 300℃, the weldabiliy is bad. Temperature gradient of x-direction (TG_x) is 0.5 to 1.0 at 0.1 intervals. Compressive load during heating, and tensile load during cooling in x-direction is 0 N to 3000 N at 100 N intervals.

Inherent strain charts are depicted in Fig. 111.

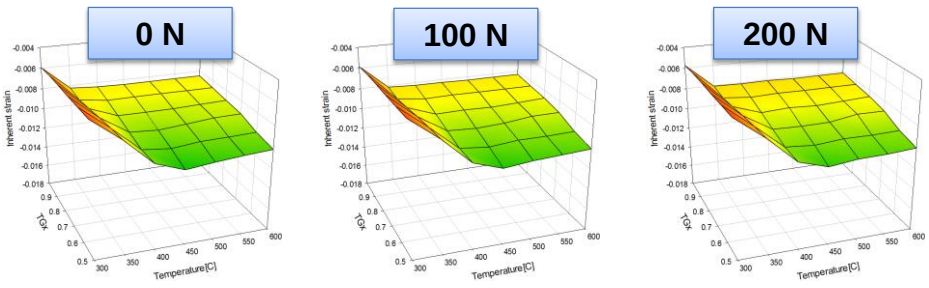

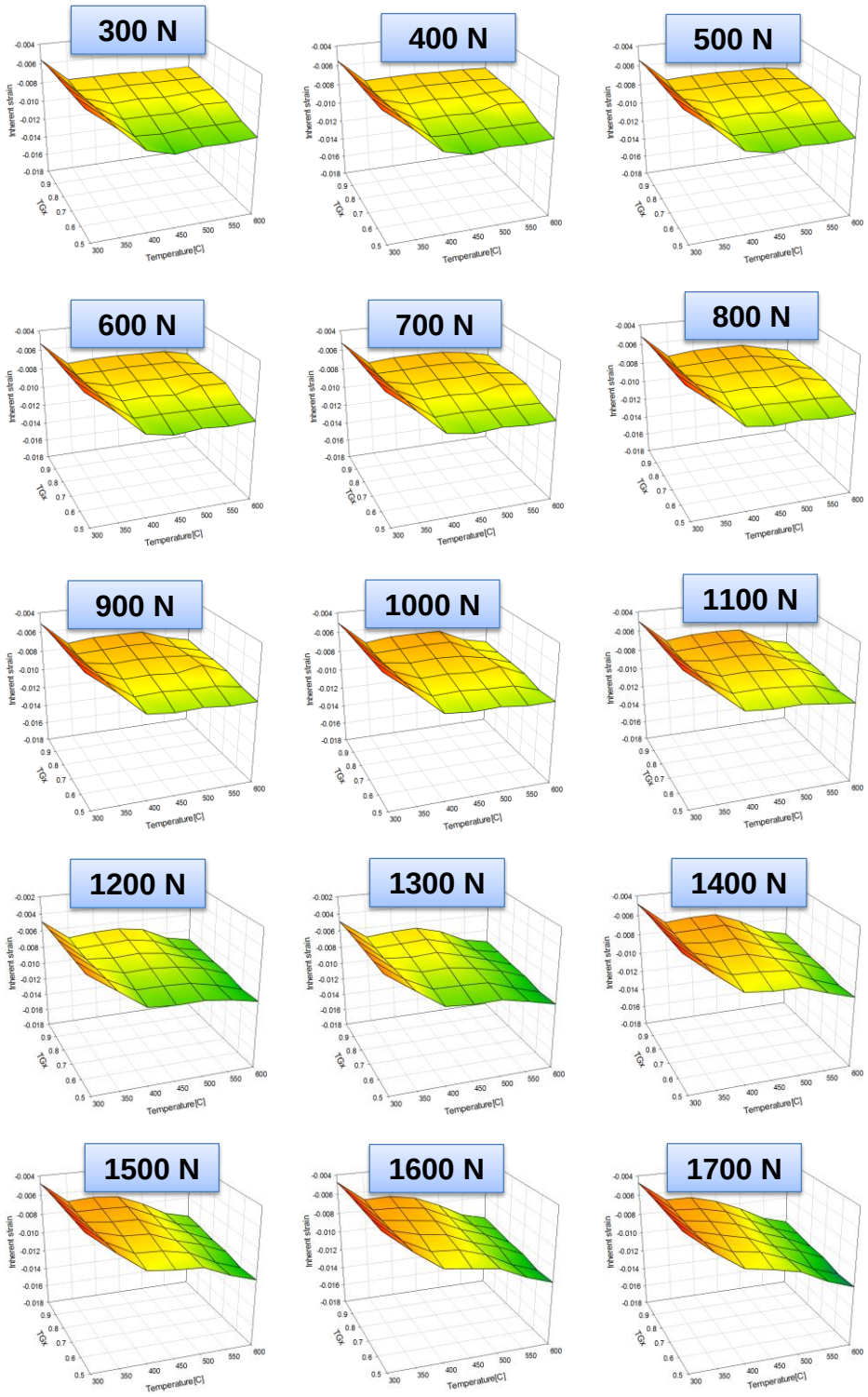
300 N
400 N
500 N
600 N
700 N
800 N
900 N
1000 N
1100 N
1200 N
1300 N
1400 N
1500 N
1600 N
1700 N
Inherent strain
TGI
Temperature[C]

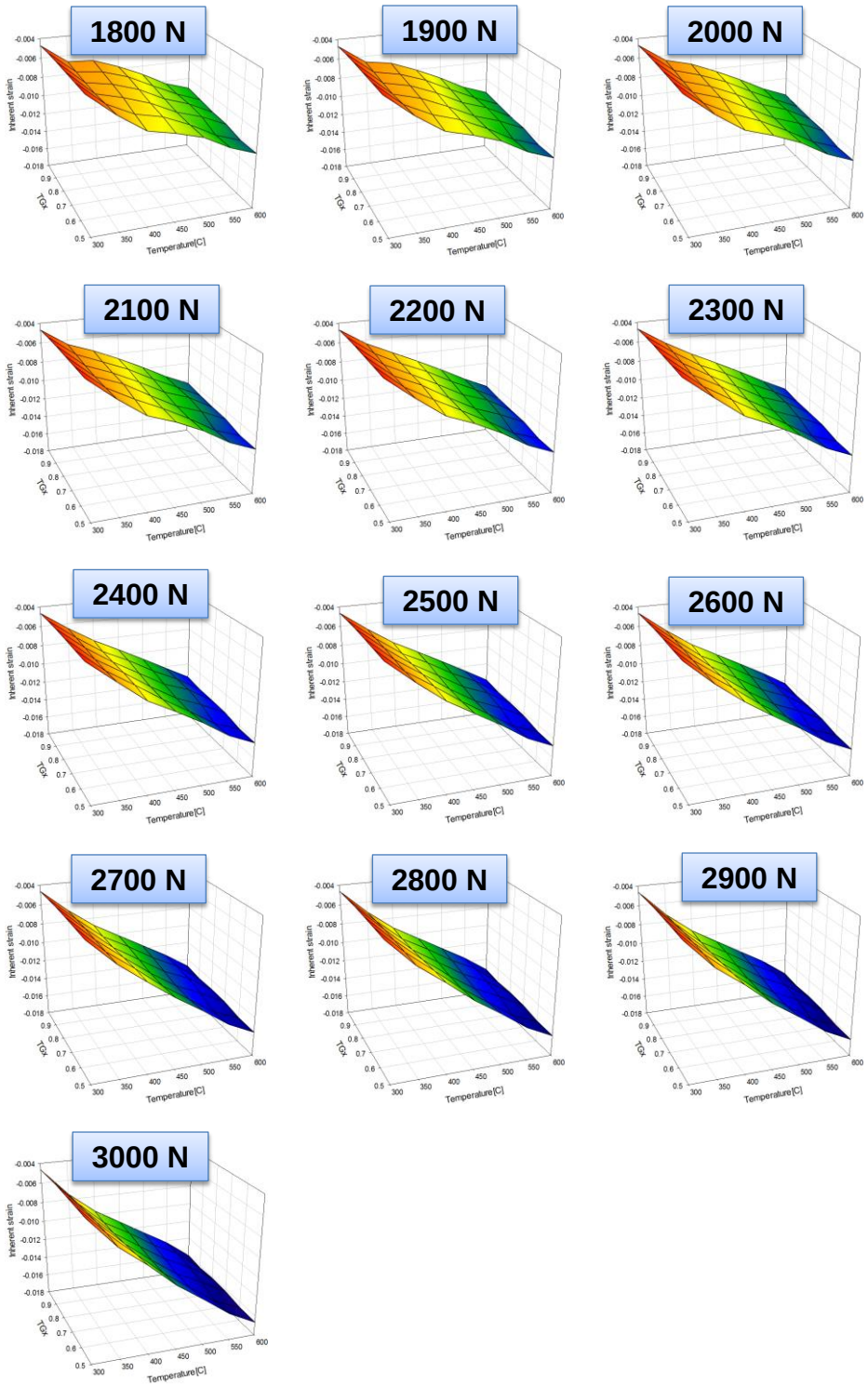

Fig. 111. Inherent strain charts.

7.5. Comparison of residual stress using experimental data, thermal elasto-plastic analysis, and inherent strain method using neural networks

In Table 21, No. 3, No. 4, No. 6, and No. 59 cases are compared with experimental data, thermal elasto-plastic analysis, and inherent strain method using neural networks in Fig. 112.

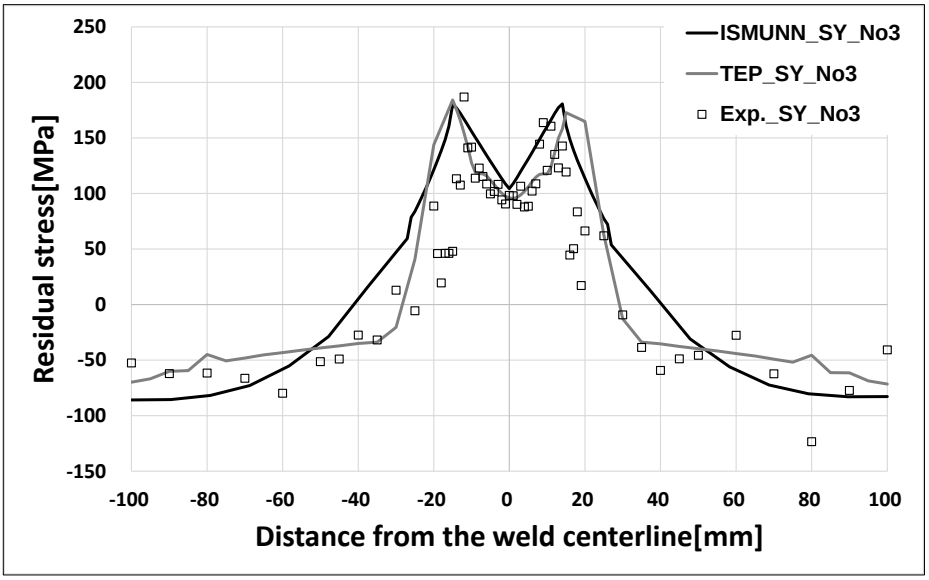

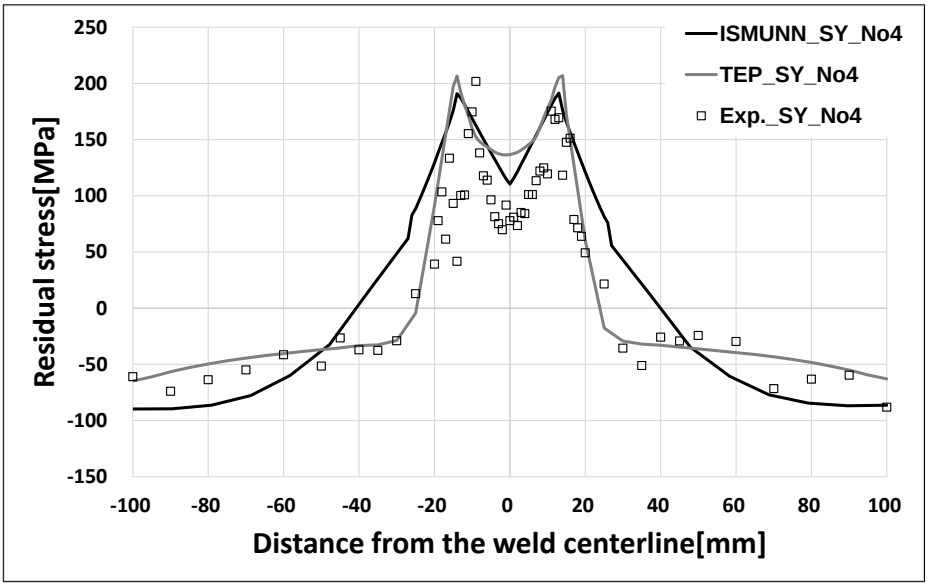
ISMUNN_SY_No4
TEP_SY_No4
Exp._SY_No4
Residual stress[MPa]
250
200
150
100
50
0
-50
-100
-150
-100
-80
-60
-40
-20
0
20
40
60
80
100
Distance from the weld centerline[mm]

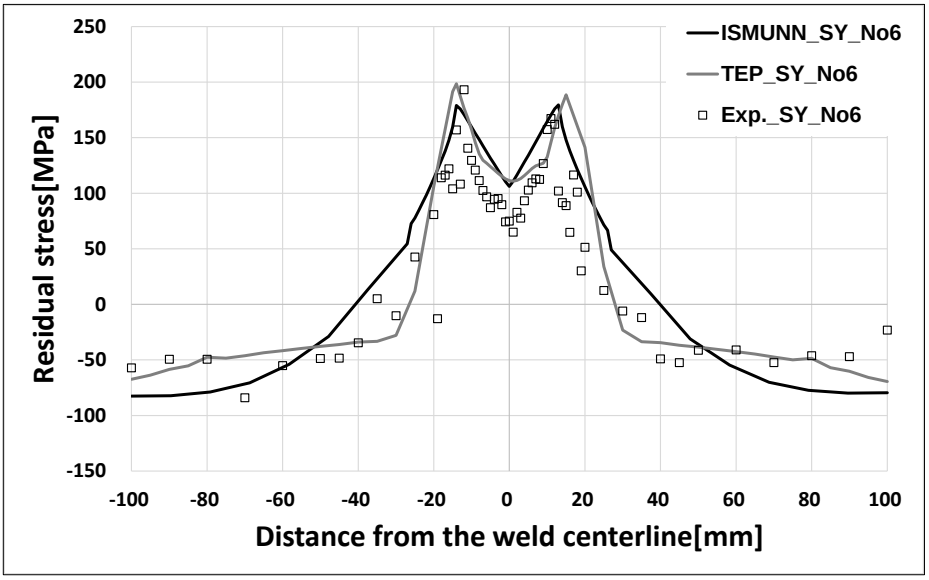
ISMUNN_SY_No6
TEP_SY_No6
Exp._SY_No6
Residual stress[MPa]
250
200
150
100
50
0
-50
-100
-150
-100
-80
-60
-40
-20
0
20
40
60
80
100
Distance from the weld centerline[mm]

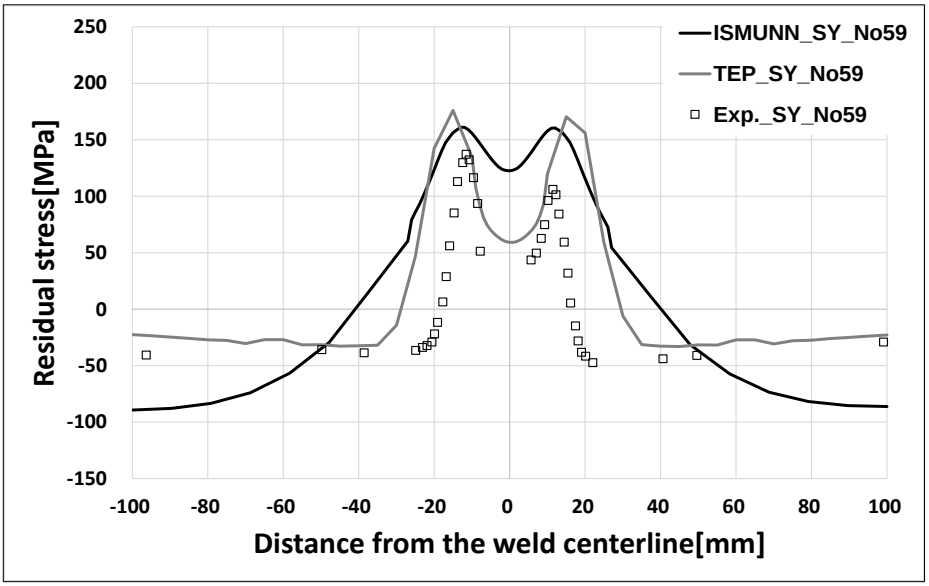

Fig. 112. Residual stress distribution in y-direction.

In Fig. 112, the experimental residual stress data of No. 59 is referred in a previous literature [48]. The experimental residual stress results and other simulation results show good agreement in each case.

Maximum residual stress values in y-direction of 61 cases in Table 21 are compared in Table 27.

Table 27. Maximum residual stress in y-direction.

	TEP	ISMUNN	Error
No1	106.17	154.01	31.06
No2	142.06	172.97	17.87
No3	184.11	180.66	1.91
No4	206.95	191.38	8.14
No5	213.64	220.51	3.12
No6	198.46	179.46	10.59

No7	184.11	180.66	1.91
No8	175.94	179.90	2.20
No9	173.64	180.06	3.57
No10	170.53	180.12	5.32
No11	124.45	128.6	3.23
No12	115.21	131.58	12.44
No13	134.29	134.96	0.50
No14	139.61	139.7	0.06
No15	148.8	145.07	2.57
No16	154.7	150.6	2.72
No17	161.19	156.18	3.21
No18	166.8	161.87	3.05
No19	172.01	167.58	2.64
No20	176.59	173.36	1.86
No21	180.63	179.28	0.75
No22	184.11	180.66	1.91
No23	187.14	192.48	2.77
No24	189.7	200.4	5.34
No25	191.66	209.72	8.61
No26	178.81	193.07	7.39
No27	198.72	216.64	8.27
No28	150.35	143.05	5.10
No29	155.81	149.17	4.45
No30	168.49	155.65	8.25
No31	178.21	162.46	9.69
No32	186.31	169.33	10.03
No33	193.55	175.95	10.00
No34	199.67	182.29	9.53
No35	204.89	188.51	8.69
No36	209.2	194.64	7.48
No37	212.66	200.72	5.95

No38	215.47	206.73	4.23
No39	217.81	212.67	2.42
No40	219.52	218.57	0.43
No41	220.78	224.48	1.65
No42	221.73	230.45	3.78
No43	165.44	155.92	6.11
No44	135.23	155.48	13.02
No45	138.31	154.38	10.41
No46	140.74	153.02	8.03
No47	147.19	151.42	2.79
No48	153.74	149.5	2.84
No49	160.42	147.52	8.74
No50	166.61	146.08	14.05
No51	172.26	149.78	15.01
No52	177.27	155.62	13.91
No53	181.53	163.91	10.75
No54	185.06	173.28	6.80
No55	187.88	184	2.11
No56	116.78	126.93	8.00
No57	153.98	141.01	9.20
No58	170.98	155.57	9.91
No59	175.92	160.99	9.27
No60	180.37	166.75	8.17
No61	190.42	186.88	1.89

In Table 27, 52 cases have an error of 10% or less, 8 cases have an error of 10 – 20%, and only 1 case has an error of over a 20%. In case of over a 20%, maximum tensile residual stress is located in about 250° C. However, it is considered that inherent strain is inputted in the position of 300° C for

consistency in inherent strain method. For this reason, a large error occurs between thermal elasto-plastic analysis and inherent strain method.

The residual stress results of elasto-plastic analysis and inherent strain method, taken as a whole, show fairly good agreement.

Finally, inherent strain method using neural network is carried out about new five cases which is not overlapped in welding speed, rotation speed of the tool, thickness of the work piece, and dimension of the tool in Table 21. Welding parameters and conditions are listed in Table 28.

Table 28. General case for verification of neural networks.

CASE	Rotation speed (RPM)	Welding speed (mm/min)	Thickness (mm)	Tool (SD x PD x PH mm)	External constraint (distance: mm)
1	1350	550	4	15 x 4 x 3.8	30
2	1050	350	5	20 x 5 x 4.5	40
3	950	450	8	24 x 6 x 7	60
4	850	450	9	28 x 8 x 8	80
5	850	350	10	30 x 10 x 9	70

In Table 28, heat transfer analysis of CASE 1 – 5 are carried out using CFD heat-flow analysis. And then, input data and output data in neural network are listed in Table 29. These data are sufficiently reasonable compared with Table 26.

Table 29. Input data using heat-flow analysis, and output data by using neural networks.

	CASE 1	CASE 2	CASE 3	CASE 4	CASE 5
Maximum temperature [° C]	440.0	520.1	480.6	516.9	572.1
Thickness [mm]	4	5	8	9	10
Location of external constraint [mm]	30	40	60	80	70
3^{rd}-order coefficient	-1.026E-06	-5.926E-06	-1.122E-05	-9.334E-06	-9.379E-06
2^{nd}-order coefficient	5.644E-04	1.480E-03	2.560E-03	2.303E-03	1.813E-03
1^{st}-order coefficient	-8.120E-02	-1.252E-01	-1.915E-01	-1.888E-01	-1.624E-01
constant coefficient	6.924	6.971	7.723	8.069	6.949

Residual stress distribution in y-direction of CASE 1 – 5 are plotted in Fig. 113 and maximum tensile residual stress values in y-direction are listed in Table 30.

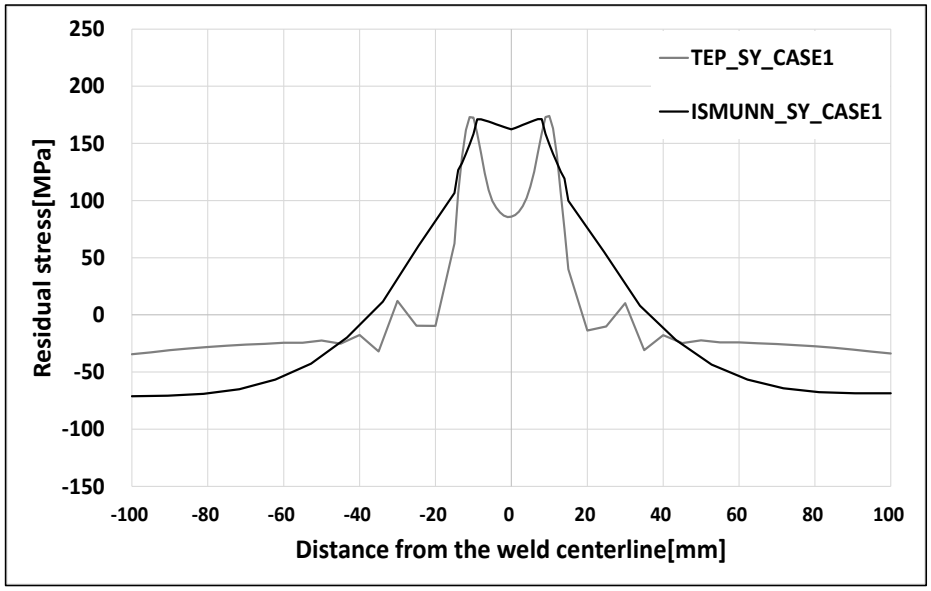
TEP_SY_CASE1
ISMUNN_SY_CASE1
Residual stress[MPa]
250
200
150
100
50
0
-50
-100
-150
-100
-80
-60
-40
-20
0
20
40
60
80
100
Distance from the weld centerline[mm]

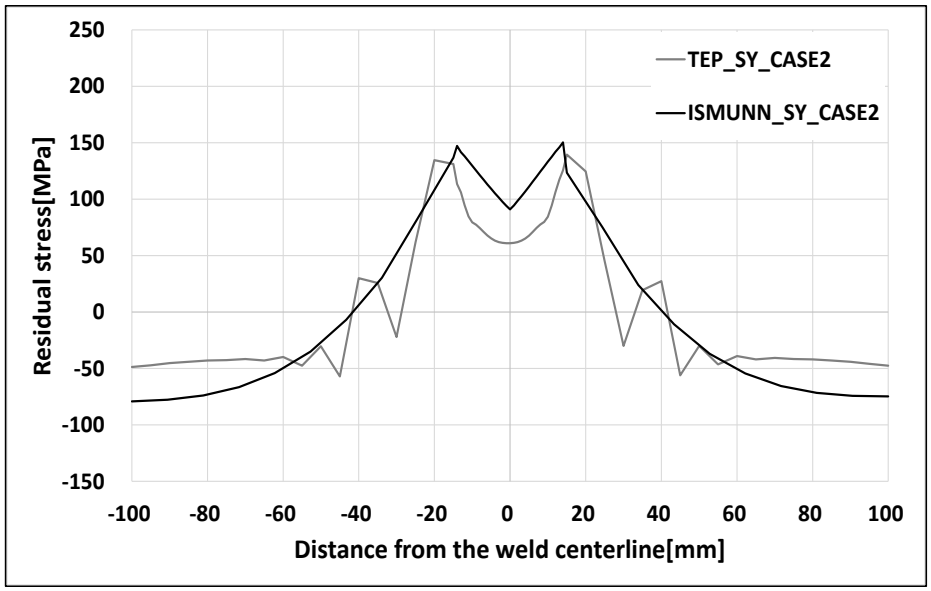
TEP_SY_CASE2
ISMUNN_SY_CASE2
Residual stress[MPa]
250
200
150
100
50
0
-50
-100
-150
-100
-80
-60
-40
-20
0
20
40
60
80
100
Distance from the weld centerline[mm]

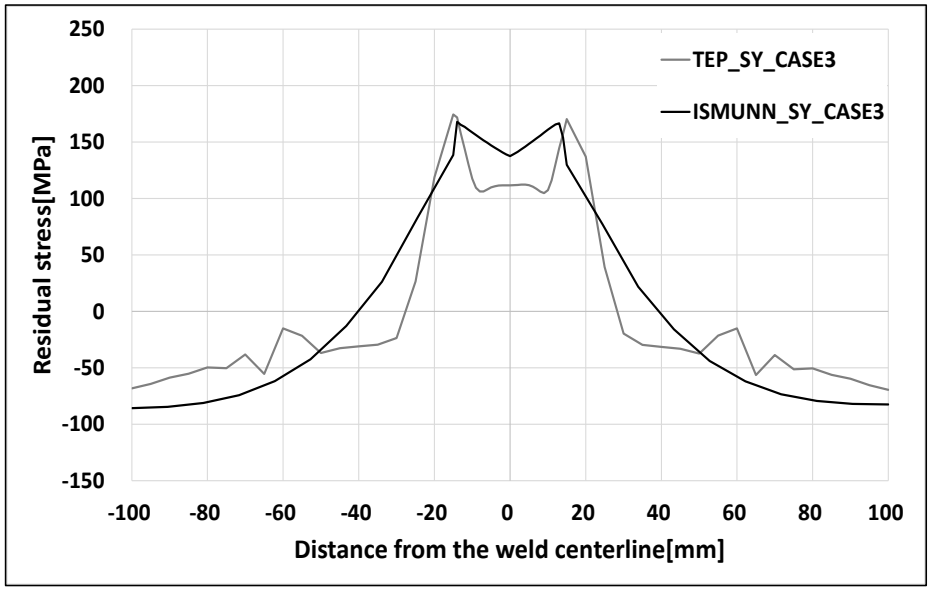
TEP_SY_CASE3
ISMUNN_SY_CASE3
Residual stress[MPa]
250
200
150
100
50
0
-50
-100
-150
-100 -80 -60 -40 -20 0 20 40 60 80 100
Distance from the weld centerline[mm]

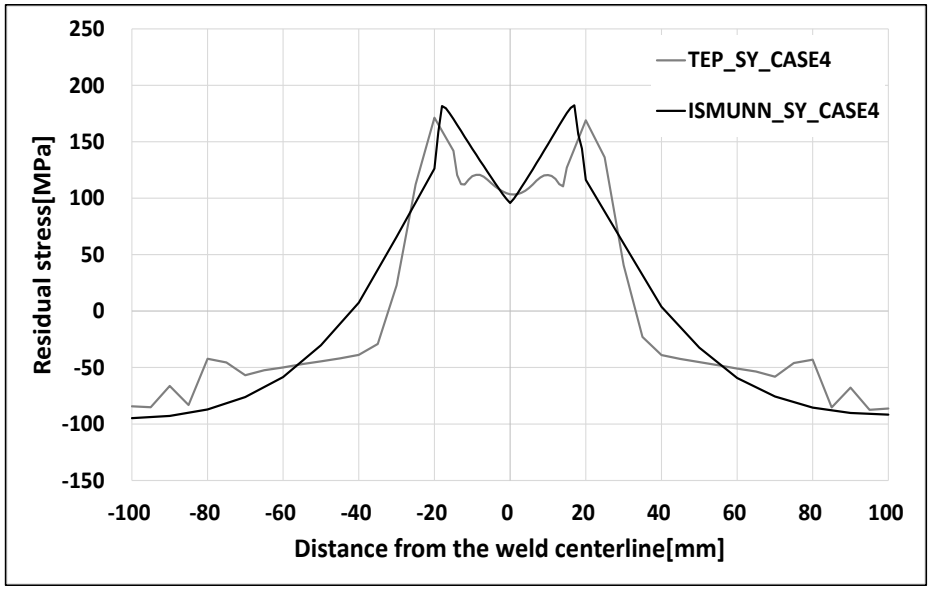
TEP_SY_CASE4
ISMUNN_SY_CASE4
Residual stress[MPa]
250
200
150
100
50
0
-50
-100
-150
-100 -80 -60 -40 -20 0 20 40 60 80 100
Distance from the weld centerline[mm]

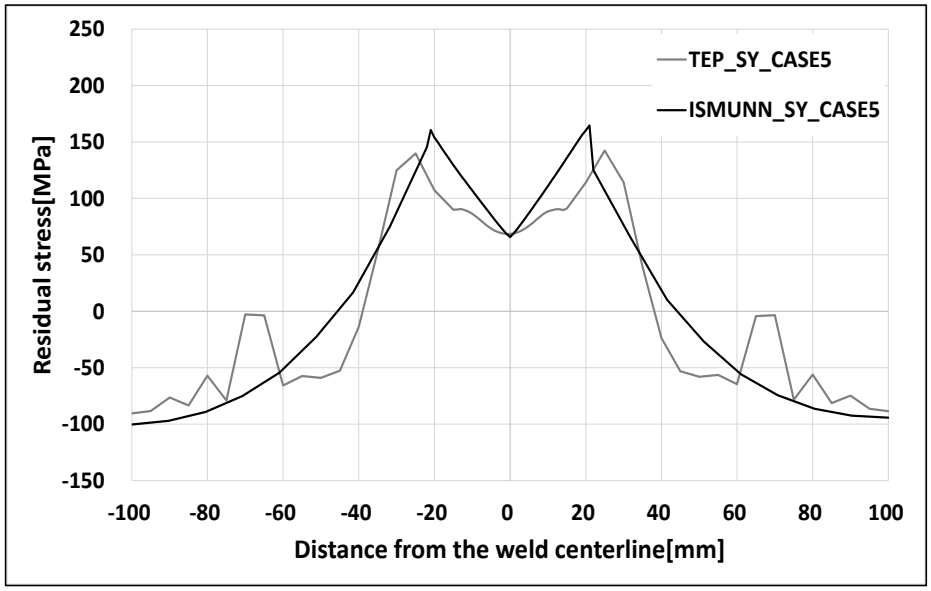

Fig. 113. Comparison of thermal elasto-plastic analysis with inherent strain method using neural networks for residual stress distribution in y-direction.

Table 30. Maximum residual stress in y-direction.

	TEP	ISMUNN	Error
CASE 1	174.00	171.21	1.63
CASE 2	139.51	150.31	-7.19
CASE 3	174.38	167.82	3.91
CASE 4	171.38	182.39	-6.04
CASE 5	142.49	164.66	-13.46

In Table 30, TEP means thermal elasto-plastic and ISMNN means inherent strain method using neural network. Thus, for the general case, when applying inherent strain method using a neural network, it was confirmed that residual stress

distribution result matches well with the thermal elasto-plastic analysis.

8. Conclusion

A three-dimensional numerical model was constructed for the purposes of a heat transfer analysis of friction stir welding (FSW) using Fluent (a commercial computational fluid dynamics software) and ANSYS multi physics (finite element analysis software).

The main conclusions of present study are summarized as follows:

1. There are some advantages in heat transfer analysis using CFD heat-flow analysis.

- ✓ Asymmetric temperature distribution.
- ✓ Analysis time is reasonable.

2. When the size of RAZ is assumed the TMAZ, the temperature results correspond in agreement with the experimental results.

3. A CFD-FEM coupled analysis is carried out and the experiments and simulations residual stress show fairly good agreement.

4. The longitudinal residual stress is proportional to the welding speed; whereas, the tool rotation speed has no significant impact on the longitudinal residual stress.

5. Welding analysis based on equivalent strain method to cover external constraint is carried out using CFD analysis result.

6. Factors affectingFinally inherent strain are listed bellows:

- ✓ Maximum temperature
- ✓ Temperature gradient in x-direction, TGx
- ✓ Reaction force during cooling stage

7. Reaction force value is predicted using neural networks.

8. Finally, comparison of thermal elasto-plastic analysis with inherent strain method. The residual stress distribution shows fairly good agreement.

REFERENCES

[1] W. M. Thomas, E. D. Nicholas, J. C. Needham, M. G. Murch, P. Temple-Smith, and C.J. Dawes, 'Friction stir butt welding, Int. Patent Application No. PCT/GB92/02203, GB Patent Application No. 9125978.8 (1991), US Patent No. 5460317 (1995).

[2] W. M. Thomas, E. D. Nicholas, J. C. Needham, M. G. Murch, P. Temple-Smith, and C.J. Dawes, Improvements relating to friction welding, International Patent Classifications B23K 20112, B29C 65/06 (1993).

[3] 김지훈, 홍재근, 이창길, 염종택, 김정한, 박노광, 강정윤, Ti합금과 Al합금 이종 마찰교반용접 접합부 특성, 대한용접학회 2009년도 춘계 학술발표대회, 2009, 51권, 127

[4] 윤태진, 김병철, 최우남, 송상우, 김남규, 정병훈, 강정윤, A5023 합금의 마찰교반용접 시 발생하는 결함 생성기구 규명, 대한용접접합학회 2009년도 추계 학술발표대회, 2009, 52권, 157

[5] 송현종, 방한서, 방희선, 차용훈, 성백섭, TIG Assisted 마찰교반용접을 이용한 이종금속재료(Al/Ti) 용접부의 용접성에 관한 연구, 대한용접학회 특별강연 및 학술발표대회, 2010

[6] 방기상, 이광진, 방한서, 방희선, Ti-6Al-4V/AA6061-T6 마찰교반용접부 계면의 미세조직, 대한용접학회 특별강연 및 학술발표대회, 2010

[7] 노찬승, 김경학, 정국성, 방한서, 방희선, 마찰교반용접을 이용한 Al5052 필렛용접시 용접공정변수에 따른 접합성 평가, 대한용접학회 특별강연 및 학술발표대회, 2013

[8] Y. J. Chao, and X. Qi, Thermal and ThermoMechanical Modeling of Friction Stir Welding of Aluminum Alloy 6061-T6, Journal of Materials Processing & Manufacturing Science, 7 (2) (1998) 215-233.

[9] J. E. Gould, and Z. Feng, Heat flow model for friction stir welding of aluminum alloys, Journal of Material Processing and Manufacturing Science, 7 (2) (1998) 185-194.

[10] P. Colegrove, Three-dimensional flow and thermal modeling of the friction stir welding process, Proceedings of the Second International Symposium on Friction Stir Welding, Gothenburg, Sweden (2000).

[11] Ø. Frigaard, Ø. Grong, and O. T. Midling, A Process Model for Friction Stir Welding of Age Hardening Aluminum Alloys, Metallurgical and Materials Transactions A, 32 (5) (2001)1189-1200.

[12] H. Khandkar, M. Zahedul, and J. Khan, Thermal modeling of overlap friction stir welding for Al-alloys, Journal of Materials Processing & Manufacturing Science, 10 (2) (2001) 91-105.

[13] M. Song, and R. Kovacevic, Heat Transfer modelling for both workpiece and tool in the friction stir welding process: A coupled model, Journal of Engineering Manufacture, 218 (1) (2004) 17-33.

[14] G. B. Bendzsak, T. B. North, and C. B. Smith, An experimentally validated 3D model for friction stir welding, Proceedings of the Second International Symposium on Friction Stir Welding, Gothenburg, Sweden (2000).

[15] C. B. Smith, G. B. Bendzsak, T. H. North, J. F. Hinrichs, J. S. Noruk, and R. J. Heideman, Heat and material flow modeling of the friction stir welding process, Proceedings of the 9th International Conference on Computer Technology in Welding, USA (2000).

[16] P. Ulysse, Three-dimensional modeling of the friction stir-welding process, International Journal of Machine Tools & Manufacture, 42 (14) (2002) 1549-1557.

[17] S. Z. Aljoaba, I. S. Jawahir, O. W. Dillon, M. H. Ali, and M. K. Khraisheh, Modeling of friction stir processing using 3D CFD analysis, International Journal of Material Forming, 2 (S1) (2009) 315-318.

[18] D. G. Kim, H. Badarinarayan, J. H. Kim, C. M. Kim, and K. Okamoto, Numerical simulation of friction stir butt welding process for AA5083-H18 sheets, European Journal of Mechanics A/Solids, 29 (2) (2010) 204-215.

[19] A. P. Reynolds, Z. Khandkar, T. Long, W. Tang, and J. Khan, Utility of relatively simple models for understanding process parameter effects on FSW, Materials Science Forum, Switzerland (2003) 2959-2964.

[20] H. Schmidt, J. Hattel, and J. Wert, An analytical model for the heat generation in friction stir welding, Modelling and Simulation in Materials Science and Engineering, 12 (1) (2004) 143-157.

[21] M. Awing, and V. H. Mucino, Energy Generation during Friction Stir Spot Welding(FSSW) of Al 6061-T6 Plates, Materials and Manufacturing Processes, 25 (1-3) (2010) 167-174.

[22] L. Fourmet, and S. Guerdoux, 3D numerical simulation of the three stages of Friction Stir Welding based on friction parameters calibration, International Journal of Material Forming, 1 (S1) (2008) 1287-1290.

[23] Y. J. Chao, X. Qi, and W. Tang, Heat Transfer in Friction Stir Welding—Experimental and Numerical Studies, Journal of Manufacturing Science and Engineering, 125 (1) (2003) 138-145.

[24] T. Hyoe, H. R. Shercliff, and P. A. Colegrove, Thermal and microstructure modelling in thick plate aluminium alloy 7075 friction stir welds, 2nd International Conference on Friction Stir Welding and Processing, San Diego, CA, USA (2003) 33-42.

[25] C. M. Chen, and R. Kovacevic, Finite element modeling of friction stir welding—thermal and thermomechanical analysis, International Journal of Machine Tools & Manufacture, 43 (13) (2003) 1319-1326.

[26] M. Song, and R. Kovacevic, Numerical and experimental study of the heat transfer process in friction stir welding, Journal of Engineering Manufacture, 217 (1) (2003) 73-85.

[27] H. S. Bang, and H. S. Bang, Transient Thermal Analysis of Friction Stir Welding using 3D-Analytical Model of Stir Zone, Journal of the Korea Welding and Joining Society, 26 (6) (2008) 580-585.

[28] B. C. Goo, and H. S. Jung, 3D Finite Element Analysis of Friction Stir Welding of Al6061 Plates, Journal of The Korea Welding and Joining Society, 29 (4) (2011) 435-441.

[29] H. Schmidt and J. H. Hattel, Thermal modelling of friction stir welding, Scripta Materialia, 58 (5) (2008) 332-337.

[30] E. Avallone, and T. Baumeister, Mark's Standard Handbook for Mechanical Engineers, 9th Ed., McGraw Hill, Columbus, USA (1987).

[31] S. Xu, X. Deng, P. Reynolds, and T. Seidel, Finite Element Simulation of Material Flow in Friction Stir Welding, Science and Technology of Welding and Joining, 6 (3) (2001) 191-193.

[32] M. Song, R. Kovacevic, J. Ouyang, and M. Valant, A Detailed Three-Dimensional Transient Heat Transfer Model for Friction Stir Welding, Proceeding of the 6th International Trends in Welding Research Conference Proceeding, Pine Mountain, GA,USA (2003) 212-217.

[33] W. S. Farren, and G. I. Taylor, The heat developed during plastic extension of metals, Mathematical, Physical and Engineering Sciences, 107 (743) (1925) 422-451.

[34] V. Singhal, P. J. Litke, A. F. Black, and S. V. Garimella, An Experimentally Validated Thermo-mechanical Model for the Prediction of Thermal Contact Conductance, International Journal of Heat and Mass Transfer, 48 (25) (2005) 5446-5459.

[35] T. Long, A STUDY OF THE FRICTION STIR WELDING PROCESS BY EXPERIMENTAL INVESTIGATION AND NUMERICAL SIMULATION, Doctorate thesis, University of South Carolina (2005).

[36] P. A. Colegrove and H. R. Shercliff, 3-Dimensional CFD modelling of flow round a threaded friction stir welding tool profile, Journal of Materials Processing Technology, 169 (2005) 320-327.

[37] R. Nandan, G.G. Roy, and T. Debroy, Numerical simulation of three-dimensional heat transfer and plastic flow during friction stir welding, Metallurgical and Materials Transactions A, 37 (4) (2006), pp. 1247-1259.

[38] D. H. Santiago, G. Lombera, S. Urquiza, A. Cassanelli, and L.A. de Vedia, Numerical Modeling of Welded Joints by the “Friction Stir Welding” Process, Materials Research, 7 (4) (2004), pp. 569−574.

[39] S. W. Kang, and B. S. Jang, Comparisons with friction stir welding heat transfer analysis methods and parametric study on unspecified input variables, Journal of Mechanical Science and Technology, Submitted in 2013.

[40] W. Woo, H. Choo, D. W. Brown, and Z. Feng, Influence of the Tool Pin and Shoulder on Microstructure and Natural Aging Kinetics in a Friction−Stir−Processed 6061–T6 Aluminum Alloy, Metallurgical and Materials Transactions A, 38 (1) (2007), pp. 69–76.

[41] T. Sheppard, and A. Jackson, Constitutive equations for use in prediction of flow stress during extrusion of aluminium alloys, Materials Science and Technology, 13 (3) (1997) 203–209.

[42] C. Zener, and J. H. Hollomon, Effect of strain rate upon plastic flow of steel, Journal of Applied Physics, 15 (1944) 22−32.

[43] N. Kumar, R. Mishra, and J. Baumann, Residual stresses in friction stir welding, A volume in the Friction Stir Welding and Processing Book Series, 2013.

[44] C. Liu, and X. Yi, Residual stress measurement on AA6061-T6 aluminum alloy friction stir butt welds using contour method, Materials and Design, 46 (2013), 366-371.

[45] C.M.Chen, and R. Kovacevic, Parametric finite element analysis of stress evolution during friction stir welding, Proceedings of the Institution of Mechanical Engineers, Part B: Journal of Engineering Manufacture, 2006, 1359-1371.

[46] M. Peel, A. Steuwer, M. Preuss, and P. J. Withers, Microstructure, mechanical properties and residual stresses as a function of welding speed in aluminium AL5083 friction stir welds, Acta Materialia, 51 (2003) 4791-4801.

[47] X. K. Zhu and Y. J. Chao, Numerical simulation of transient temperature and residual stresses in friction stir welding of 304L stainless steel, Journal of Materials Processing Technology,146 (2004) 263-272.

[48] Z. Feng, X.L. Wang, S.A. David, P. Sklad, Modelling of residual stresses and property distributions in friction stir welds of aluminium alloy 6061-T6, Proceedings of the fifth International Symposium on Friction Stir Welding, Metz, France, TWI (2004).

[49] W. Woo, H. Choo, D.W. Brown, Z. Feng, and P.K. Liaw, Angular distortion and through-thickness residual stress distribution in the friction stir processed 6061-T6 aluminum alloy, Materials Science and Engineering, A437 (2006) 64-69.

[50] V. Dattoma, M. De Giorgi, R. Nobile, On the residual stress field in the aluminum alloy FSW joints, Strain, 45 (2009) 380-386.

[51] G. Buffa, A. Ducato, L. Fratini, Numerical procedure for residual stresses prediction in friction stir welding, Finite Elements Analysis Design, 47 (2011) 470-476.

[52] R. Mohammad, and N. Hamidreza, Analysis of transient temperature and residual thermal stresses in friction stir welding of aluminum alloy 6061-T6 via numerical simulation, The International Journal of Advanced Manufacturing Technology 55 (2011) 143-152.

[53] L. Z. Jin and R. Sandström, Numerical simulation of residual stresses for friction stir welds in copper canisters, Journal of Manufacturing Processes, 14 (2012) 71-81.

[54] S. Sadeghi, M.A. Najafabadi, Y. Javadi, M. Mohammadisefat, Using ultrasonic waves and finite element method to evaluate through-thickness residual stresses distribution in the friction stir welding of aluminum plates, Materials and Design, 52 (2013) 870-880.

[55] T. J. Kim, Welding deformation analysis based on improved equivalent strain method to cover external constraint during cooling stage, Ph. D thesis in Seoul National University, 2014.

[56] Y. T. Kim, Structural analysis of ship hull block considering welding residual stress using equivalent strain method based on inherent strain, Ph. D thesis in Seoul National University, 2010.